COMPUTATIONAL STUDY OF UNDERSTANDING POROUS MATERIALS STABILITY UPON ACID GAS TREATMENT

A Dissertation
Presented to
The Academic Faculty

by

Yang Liu

In Partial Fulfillment
of the Requirements for the Degree
Doctor of Philosophy in the
School of Chemical and Biomolecular Engineering

Georgia Institute of Technology
December 2018

COMPUTATIONAL STUDY OF UNDERSTANDING POROUS MATERIALS STABILITY UPON ACID GAS TREATMENT

Approved by:

Dr. David S. Sholl, Advisor
School of Chemical and Biomolecular Engineering
Georgia Institute of Technology

Dr. Krista S. Walton
School of Chemical and Biomolecular Engineering
Georgia Institute of Technology

Dr. Ryan P. Lively
School of Chemistry & Biochemistry
Georgia Institute of Technology

Dr. Sankar Nair
School of Chemical and Biomolecular Engineering
Georgia Institute of Technology

Dr. Thomas Orlando
School of Chemical and Biomolecular Engineering
Georgia Institute of Technology

Date Approved: [October 22, 2018]

[To the students of the Georgia Institute of Technology]

ACKNOWLEDGEMENTS

Firstly, I would like to heartily thank my advisor, Dr. David S. Sholl, who expertly guided me through my graduate education at Georgia Tech. He is a great advisor, not only in my research, giving me valuable instructions on my research, but also in my personal and professional career development, setting a successful role model to me.

Besides my advisor, I would like to thank the rest of thesis committee members, Dr. Krista Walton, Dr. Ryan Lively, Dr. Sankar Nair, and Dr. Thomas Orlando for their continued encouragement, insightful instructions, and useful questions.

Next, this work would not have been possible without the financial support of UNCAGE-ME, an Energy Frontier Research Center funded by the U.S. Department of Energy.

My sincere thanks also go to Dr. Alice He and Dr. Joshua Thompson, for offering me two summer internship opportunities in Separations R&D team at Chevron and leading me working on multiple exciting projects. Company culture and team working environment are so nice and I really enjoyed my working experience.

I am also grateful to all of my collaborators with whom I have had the pleasure to work during my thesis projects, Dr. Guanghui Zhu, Dr. Joshua Howe, Dr. Yang Jiao, Dr. Luis Flores, Zachary Lee, Wenqin You, et al. Without support from whom, I would not have too many opportunities to apply my simulation expertise in multiple scenarios and

build my research productivity. Especially, I would like to thank Dr. Guanghui, my best collaborator and mentor, without whom, I couldn't have so many achievements today.

I feel great honor to meet many valued friends during the school life at Georgia Tech. Within Dr. David Sholl's group, I'd like to thank Wenqin You for being my best friend at Atlanta, Omar Knio for being my best officemate, Dr. Joshua Howe and Dr. Hanjun Fang for all the help and instructions for my research, and Dr. Chu Han, Rebecca Han, Dr. Dai Tang, Mayank Agrawal, Dr. Dalar Nazarian, Dr. Jeffery Camp, and Dr. Ross Verploegh for their help and useful discussions. Besides my friends within Dr. David Sholl's group, I also want to express my thanks to Dr. Songcheng Wang, Hongjian Tang, Yang Yang for sharing best time at CRC. Thank you all for taking this journey with me.

Finally, nobody has been more important to me in the pursuit of the doctoral degree than my parents. I would like to thank my parents, whose love and guidance are with me in whatever I pursue. Thank you for my boyfriend, Weicheng Bai, for his unconditional love and valuable support. I couldn't be as lucky as I am.

TABLE OF CONTENTS

LIST OF TABLES

LIST OF FIGURES

SUMMARY

The stability of porous materials in acid gases and water environments is a critical property as well as an issue that must be addressed when applying porous materials in adsorptions, separations and catalytic processes, where acid gases and water always coexist with the adsorbates, influencing the performance of porous materials. Since this is vital but not widely explored, my research proposed computational modeling to understand the chemical stability and degradation mechanism of porous materials upon humid acid gas treatment, and then developed chemical stable porous materials that are suitable for use with the existence of aggressive contaminants such as H_2S, SO_X, and NO_X. The porous materials studied in this work range from Metal Organic Frameworks (MOFs) to Porous Organic Cages (POCs) with different types of covalent bonds, **i.e.** MOF-2 with metal to charged ligand bond, UiO-66 with metal oxide cluster to charged ligand bond, and Cage crystal 3 (CC3), one of the imine-based POCs with non-metal to non-metal bond.

Since POCs are relatively new emerging porous materials, apart from studying their chemical stability, its formation pathway was thoroughly explored and understood. With a detailed understanding of POCs formation mechanism, two strategies have been applied to adjust the crystal structure of POCs to improve crystal properties. Firstly, "missing-linker" type of point defects were introduced into the CC3-R crystal, and defective CC3-R crystal was found to have enhanced CO_2 interaction and improved CO_2 uptake capacity due to the additional functional groups present within the defective CC3-R crystals. In addition to defect engineering, a modification to the chirality of CC3

crystals was intentionally designed, forming mixed-chirality CC3-racemic crystals. The improved sorption properties and stability of CC3-racemic crystals relative to homochiral CC3 crystals led us to fully resolve the structure of this racemic crystal. Finally, an *in silico* prediction methodology was introduced that combines electronic structure calculations and atomistic calculations to predict the structure of CC3-racmeic crystal, which were not currently available from experiments alone.

CHAPTER 1. INTRODUCTION

1.1 Nanoporous Materials

Nanoporous materials have attracted attention for adsorption, separation, and catalysis applications due to their large internal surface areas, large pore volume, etc. There are many different classes of nanoporous materials, including zeolites, metal-organic frameworks (MOFs), covalent organic frameworks (COFs), and recently newly synthesized porous organic cages (POCs). In this work, MOFs and POCs are selected as examples.

1.1.1 Metal-Organic Frameworks

Metal-Organic Frameworks (MOFs) as a novel class of nanoporous materials have received increasing research interest for potential use as materials for separations, storages, membranes, and catalysis applications.[1-15] MOFs are porous hybrid compounds that consist of metal ions or metal clusters linked by organic ligands to form one, two, or three-dimensional pore networks. By altering the organic ligands, it is possible to design MOFs with well-defined pore shapes, pore sizes, surface areas, and chemical functionality. To date, over 20,000 MOFs have been reported.[16] In addition, over 137,000 hypothetical MOFs have been identified based on known MOFs.[17]

MOFs have been tested in a variety of adsorption applications, such as CO_2 capture from the atmosphere and flue gases, H_2 and CH_4 storage, and the separation of hydrocarbons. MOFs with open-metal sites, such as MOF-74, were examined to exhibit desirable high CO_2 uptake and selectivity at low pressures and ambient temperature,

contributed from the strong affinity of CO_2 on open-metal sites.[18] For adsorptive H_2 storage, increasing the surface areas of MOFs as well as the adsorption enthalpy of H_2 on MOFs were utilized as strategies to enhance the volumetric H_2 adsorption.[19-21] Regarding hydrocarbon separation applications, the MOF $Cu_2(pzdc)_2(pyz)$ was found to effectively separate C_2H_2 from the mixture gas containing CO_2 impurities as a result of strong hydrogen bonding established between C_2H_2 and oxygen atoms on the MOF's internal surface.[22]

MOFs also have potential as heterogeneous catalysts as a result of their high surface area, tunable porosity, and high density of active sites.[11, 23] Alaerts et al. has showed that the open-metal sites on HKUST-1 can serve as Lewis acid sites and thus HKUST-1 showed potential use as catalysts for several isomerization reactions.[24] In another study, MIL-47 and MOF-48 have been found to have catalytic activity for the conversion of methane to acetic acid and remain chemically stable at the same time.[25]

Most MOFs are composed of coordinative bonds, resulting in their weak chemical stability; but a sub-set of MOFs with zeolite framework topologies, zeolitic imidazolate frameworks (ZIFs) have been shown to have relative high thermal stability (up to 550 °C) and quite good chemical resistance to water and organic solvents.[26] However, only a few MOFs, such as UiO series MOFs, have exhibited high chemical stability towards acidic or basic environments, which commonly exist in industrial applications.[27-28] In order to enhance MOF's performance for use in such an conditions, a comprehensive understanding of chemical stability and degradation mechanisms of MOFs is needed and will be discussed in Chapter 2 and Chapter 3, using two representative MOFs, including M-BDC nanosheet (M = Zn, Cu, and Co) and pristine and defective UiO-66 as examples.

1.1.2 Porous Organic Cages

Porous Organic Cage (POC) molecules have attracted significant attention due to some potential advantages with respect to porous extended framework materials (MOFs and ZIFs) since their discovery in 2009 by Cooper and co-workers.[29] Unlike extended framework materials such as zeolites, COFs, and MOFs that are connected by covalent or coordination bonds, POC solids are comprised of individual porous molecules held together by relatively weak dispersion packing forces. POC solids can have both extrinsic packing voids and intrinsic cage cavities that form either one, two, or three-dimensional pore networks.[30-33]

POCs have been synthesized through different dynamic covalent chemistries, including imine condensation reactions.[34-36] The formation mechanisms of imine-based POCs can be studied with a combination of time-resolved electrospray mass spectrometry and electronic structure calculations, as described in Chapter 4.[37] Recently, Lucero et al. observed and analyzed the crystal structure evolution of an imine-based POC as a function of crystallization time.[38] Fundamental studies of this kind are critical to achieving structural and morphological control of POC crystals.

POCs have shown promising properties and attracted significant attention in applications including gas separation, adsorption, catalysis, and molecular sensing.[29, 34-35, 39-52] Over 20 kinds of POCs have been synthesized and evaluated, with some examples are presented above the timeline in Figure 1.1. One favorable attribute of POCs is structural mobility of the cages due to the lack of intermolecular covalent bonding between individual blocks. With this structural mobility, previous work has shown the

inclusion of solvent molecules can in some cases control and change the crystal packing motifs in POC crystals from 2-D pore networks to 3-D interconnected pore networks.[33] In addition, the structural mobility of the cages can bring cooperative interactions between the host (POCs) and guest adsorbate molecules. Recent work has shown that one type of POCs was able to adsorb a large amount of SF_6, the size of which is much larger than the POC window diameter, due to cooperative diffusion and structural rearrangement, as shown in Figure 1.2. Figure 1.2 (b) shows the comparison of the pore envelope of the POC window with and without SF_6 capped inside. The black line is the window diameter distribution for the empty cage without SF_6. The green line and red line are the cage window diameter distribution with SF_6 being captured inside the cage cavity and positioned in the window. It is clear that the cage window size increased with SF_6 traversing the window.

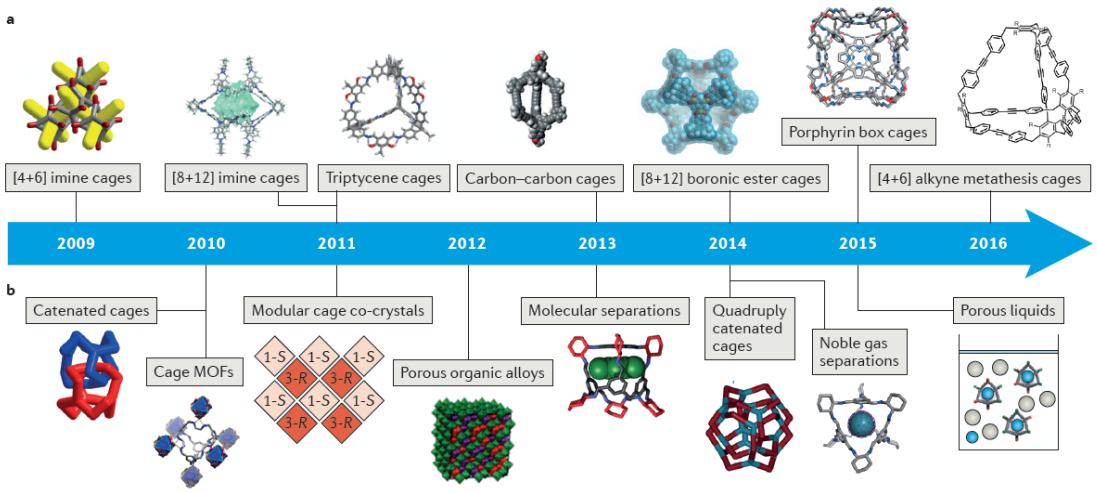

Figure 1.1 A timeline of porous organic cages. (a) Some representative porous organic cages. (b) Selective discoveries and practical uses related to porous organic cages. Reprinted from Ref 35.[35]

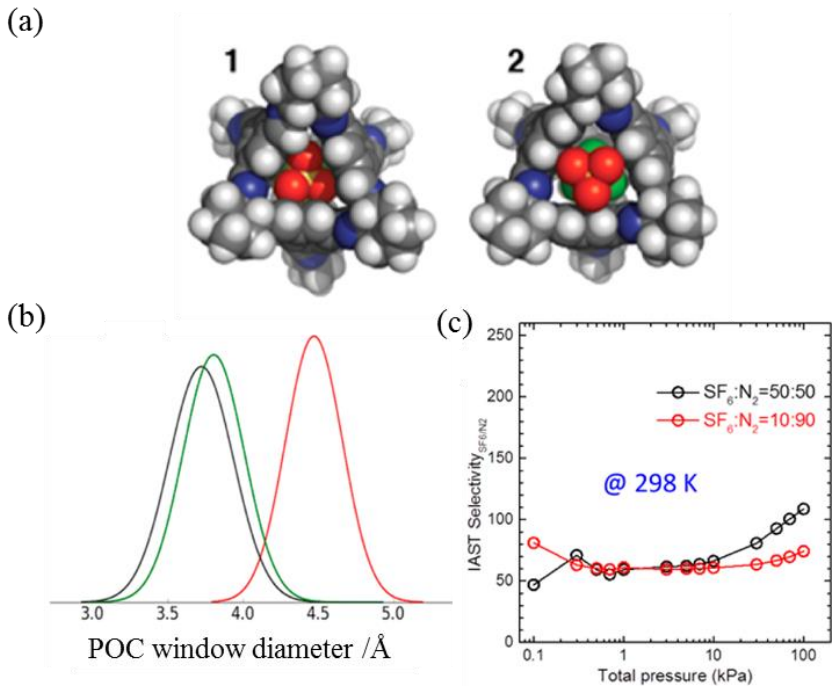

Figure 1.2 (a) Configurations of SF_6 molecule being captured in the cage cavity and SF_6 molecule being placed in the center of window. (b) Comparison of pore envelope of POC window, for an empty cage (black), for a cage with SF_6 occupying the cage cavity (green), and for cage where SF_6 is positioned in the window (red). (c) IAST selectivity for SF_6 over N_2 at SF_6:N_2 ratios of 50:50 and 10:90 at 298K. Reprinted from Ref 53.[53]

In addition to structural mobility, since cages are discrete molecules, in contrast to extended framework materials such as MOFs and zeolites, POCs can be dissolved in common organic solvents without altering the porosity of individual cages, which potentially allows the formation of more coherent mixed matrix membrane (MMM) composites than zeolites and MOFs for separation applications. Recent studies have demonstrated that porous organic cages can be solution-processed into coherent thin film membranes with tunable structure and porosity. These thin film membranes have shown potential in molecular-level separations with both high gas permeance and molecular selectivity. Evans et al. performed a theoretical study of using crystal porous organic

cages (CC1, CC2, CC3, CC4, and CC5) as additives to MMMs, which exhibited enhanced selectivity and permeability for H_2/CO_2 separations.[54] Jiang et al. demonstrated a method to introduce porosity into other non-porous materials, by blending porous organic cages as "porous additives", which has potential applications in porous polymer coatings and gas separation membranes.[55] Due to the soluble nature of POCs, it is possible to mix a combination of different porous molecules together in one system, generating additional extrinsic porosity between the cage molecules.[56,57] For instance, Jiang et al. presented a chemical approach to synthesize a mixture of amorphous POCs via vertex exchange of CC1 and CC3.[56]

Another interesting attribute of POCs is the chirality that can result from imine condensation reactions involving chiral diamines.[39, 50, 58-60] Chiral materials are of intrinsic interest for a variety of fundamental and applied reasons.[61-62] Chirality within POC materials plays an important role in controlling the crystalline assembly of these porous organic molecules.[60, 63] Cooper and co-workers reported that discrete CC3 cages with opposite chirality are able to pack more strongly by chiral recognition than CC3 cages with same chirality.[60, 64-65] In addition, intrinsically chiral POCs are interesting candidates for separation of chiral molecules. Chen et al. showed that homochiral CC3 materials exhibited an enantioselective separation for chiral alcohol, 1-phenylethanol.[50]

Recently there has been growing emphasis on defect engineering in the study of MOFs, as the mechanical and chemical properties resulted from defects have the potentials to broaden the utility of these materials.[66-67] However, in the area of POCs, current studies often assume chemical purity of the cage crystal. Little is known about the formation or existence of defects in POCs. Inspired by this, we are interested in

introducing defects into CC3-R crystals and investigating the influence of defects on adsorption properties of CC3-R crystals. Detailed work is introduced in Chapter 4.

The brief literature review above suggests POCs' potential applications in a variety of industrial areas and defect-engineering. The viability of POCs materials in industrial conditions, however, also depends on structural resilience to high temperature, high humidity, acidic environment, etc. Previous studies have demonstrated that POCs solid crystals have good thermal stability, as well as water stability,[57,68] but didn't mention how these materials respond to acid gases, which may constrain the application of POCs. Our study addresses this aspect of POCs for the first time in Chapter 4.

1.2 Chemical Stability of Porous Materials

Chemical stability for porous materials can be described as the resistance of the structure to degradation in acidic, basic and neutral gas or aqueous solutions. For MOFs, the weakest structural feature is the metal-ligand bonds, which will be attacked by water or other chemicals, resulting in the removal of protonated ligands from MOFs.[69-71] Howarth et al. summarized the chemical stability of some representative MOFs exposing to acid, basic and neutral aqueous solutions in their recent review, as shown in Figure 1.3.[72] For POCs, the degradation mechanism has not been explored yet.

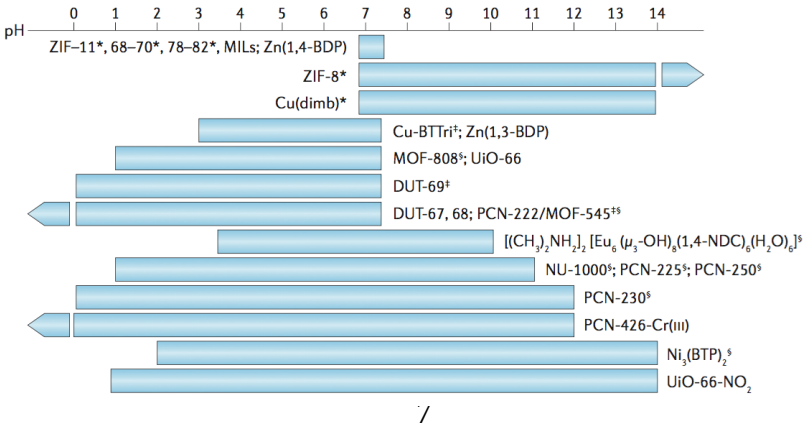

Figure 1.3 Summarized chemical (acid-base) stability of some representative MOFs. The bar length indicates the pH range that the MOFs can tolerate. An arrow indicates that the MOFs can withstand pH<0 or pH>14. Reprint from Ref 72.[72]

In recent years, water stability of MOFs has been widely investigated. Burtch et al. listed several structural factors that govern MOFs water stability[71] in the thermodynamic regime, i.e. inertness of metal clusters, metal-ligand bond strengths, and the lability of metal cluster towards water (in a sequence of decreasing importance), and the kinetic regime, i.e. hydrophobicity of MOF's external or internal surface, and steric factors around metal center and labile ligands (in a sequence of decreasing importance). Various methods to stabilize microporous MOFs against hydrolysis have been explored. Mixing a more stable metal ion into a metal cluster is able to enhance the strength of the metal-ligand bond. Jiao et al. demonstrated that incorporating as little as 16 mol % Ni into the Mg-MOF-74 structure can significantly enhance water stability.[73] Incorporating hydrophobic fluorinated and alkyl functional groups on the ligand to prevent water coming close to metal clusters is also widely utilized.[74-75] Wu et al. demonstrated introducing trifluoromethoxy functional groups into IRMOF-1 could enhance the MOFs stability in the humid air as shown in PXRD spectrum. Except for incorporating hydrophobic functional groups, hydrophilic modification can also increase MOF's water stability.[76-77] DeCoste et al. showed that amine-functionalized UiO-66 was stable towards HCl, as the result of the formation of an $-NH3^{+}Cl^{-}$ adduct.[78]

The mechanisms for MOFs degradation, as well as enhancing MOFs stability towards humid acid gases are likely to be similar to those for water, but limited detailed information is available. Han et al. investigated the influence of humid air and acid gas exposure on the selectivity of CO_2/N_2 on MOFs, and they found Cu-HF and Ni-NIC remained stable after exposure, and Zn-NDC showed partial decomposition with decreased CO_2 adsorption capacity.[79] Mounfield et al. explored the effects of acid gas adsorption on CeBTC and MIL-125 and observed that both materials experienced a drastic loss in surface area and porosity attributed to chemical degradation.[80] Mounfield et al. have synthesized amine functionalized MIL-125 (MIL-125-NH_2) and evaluated corresponding structural chemical stability with respect to that of pristine MIL-125.[81] Increased chemical stability under both humid and aqueous acidic environments in MIL-125-NH_2 was observed and explained with combined experimental and computational study. Pang et al. found that different crystallographic facets of ZIF-8 crystal exhibited different thermodynamic stability under mildly acidic conditions (aqueous SO_2 exposure). They hypothesized that the particles experienced a shrinking-core degradation mechanism, with surface imidazolates being replaced by hydroxyls with support from both experimental and computational study.[82] Bhattacharyya et al. also examined the chemical stability of ZIF-8 crystal under SO_2 exposure in dry, humid, and aqueous environments.[83] With the help from several characterization techniques (PXRD, N_2 physisorption, EDX, XPS, and FTIR), a detailed degradation mechanism of ZIF-8 crystal exposure to humid SO_2 was proposed. Sulfur hydrate species formed in humid SO_2 attack the Zn-N bonds between metal center and imidazole ring. He further developed a systematic knowledge of the kinetic and thermodynamic stability of a diverse range of

ZIFs under humid air, liquid water, and acid gases CO_2 and SO_2 (dry, humid, and aqueous) environments in his recent work.[84] Specifically, a strong correlation between the kinetic stability of ZIFs and the linker p*K*a and ZIF water adsorption capability was explored and understood.

1.3 Computational Methods

Degradation mechanisms of MOFs in acidic environment are still largely unexplored. Mondloch et al. presented a hypothesized hydrolytic degradation pathway of UiO-67 based on a cluster model,[85] shown in Figure 1.4(a). DeCoste et al. proposed a degradation mechanism for ZrMOFs upon water, HCl, and NaOH attack, driven by experimental phenomena, starting from breaking Zr–O bonds,[78] shown in Figure 1.4(b). They further suggested that the decreased stability of the double ring structures in UiO-67 can be attributed to steric and rotational effects. Kusgens et al. suggested that hydrolysis of metal–carboxylate bonds in MOFs is driven by the ability of multiple water molecules to access and cluster around the metal–carboxylate sites.[86] Ming et al. proposed a degradation pathway for MOF-5 driven by the water insertion based on FTIR spectra, shown in Figure 1.4(c).[87] These studies share the same concept that the structure breakdown starts from the attack on metal-ligand bonds.

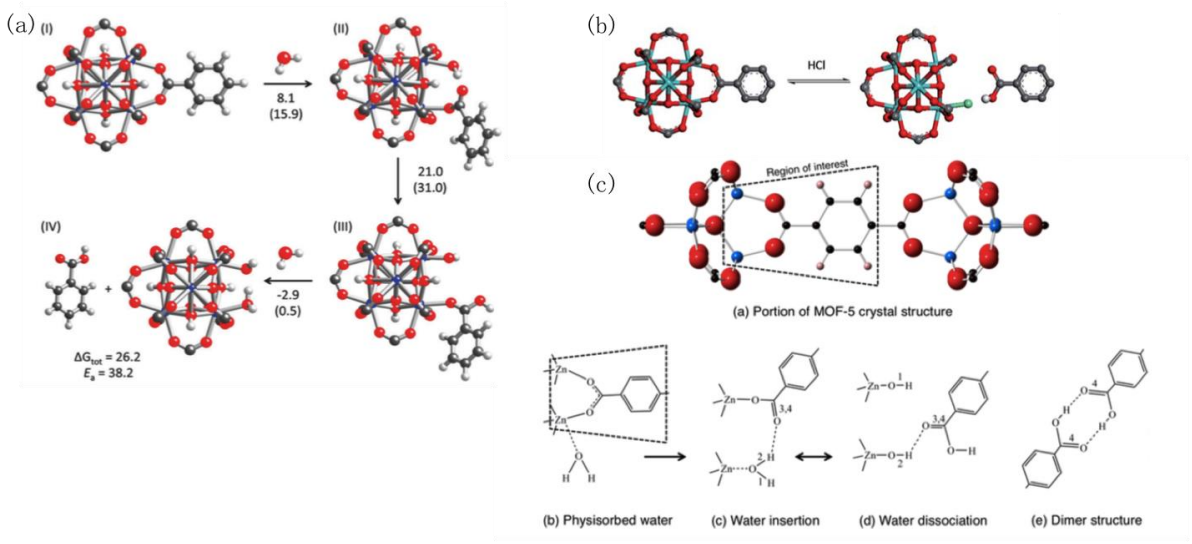

Figure 1.4 (a) Hypothetical hydrolytic degradation mechanism of UiO-67. (b) Proposed mechanism for the structural breakdown of ZrMOFs in the presence of HCl. (c) Proposed pathway for the reaction of water with MOF-5. Reproduced from ref 85, ref 78, and ref 87. [78, 85, 87]

To study the chemical stability of MOFs and POCs in acidic environments, we first propose potential degradation pathways based on chemical degradation studies of MOFs. We compare the calculated formation energies as well as activation barriers for each process along the proposed reaction pathway among various MOFs or POCs to investigate their relative chemical stability. Similar methods have been applied previously for studying the relative hydrothermal stability of MOFs. Low et al. combined quantum mechanical calculations with experimental testing to understand the relative hydrothermal stability of MOFs, including MOF-69C, MOF-5, MOF-508B, MIL-110, HKUST-1, Cr-MIL-53, MIL-101, MOF-74, AL-MIL-53, and ZIF8.[88] We further support our proposed degradation mechanisms by comparisons between the calculated IR frequencies associated with each state along the reaction pathway and experimentally measured in-situ IR data. This combination of methods with the help of in-situ IR and

DFT calculations have been applied in recent studies. For example, Tumuluri et al. investigated the effects of the surface structure and defects on the interaction between SO_2 with CeO_2 using in-situ IR, Raman spectroscopies and first-principles calculations.[89]

The calculation methods used when implementing our methodology for nanoporous material chemical stability studies are briefly described below.

1.3.1 Density Functional Theory

Density Functional Theory (DFT), as a computational quantum mechanics modeling method, has been widely used to investigate the electronic structure properties of nanoporous materials, semiconductors, metals, metal oxides, etc.[90-93] The properties of such many-electron system are described by functionals, which spatially depends on electron density. Wavefunctions can be expressed through a linear combination of either planewave basis set functions or Gaussian basis set functions. For describing the electronic properties of the periodic system, the wavefunctions can be written as a product of a cell periodic part and a plane wave part. Such DFT calculations can be performed in the Vienna Ab initio Simulation Package (VASP) with a planewave basis set and core electrons represented with projector augmented wave (PAW) potentials[94-95]. By contrast, for describing isolated atoms and molecules, where the wavefunction exponentially decays to zero at large distances, atomic orbitals can be used as basis functions as implemented in Gaussian package.[96] As related to the study of nanoporous materials, DFT is useful for modeling the material systems that contain fewer than roughly 1000 atoms, due to computational limitations associated with scaling to large systems.

1.3.2 Molecular Modelling

Molecular modeling methods describe the molecular systems at the atomic level and treat atoms as the smallest individual unit with point charges and masses. Intramolecular forces are described as chemical bonds, and intermolecular forces are represented by Van der Waals forces. Electrostatic interactions are calculated based on Coulomb's law. Molecular modeling methods focus on finding low potential energy states of molecular systems and corresponding molecular conformations. Many macroscopic properties can be obtained by averaging over different molecular system states, and thus molecular modeling methods have been widely used to investigate the thermodynamic properties, reactive properties, adsorptive properties, diffusive properties, etc. in the area of nanoporous materials. There are two well established molecular modeling methods to find the low potential energy states of molecular systems: Monte Carlo (MC) simulation and molecular dynamics (MD) simulation.

1.3.2.1 Monte Carlo Simulation

Monte Carlo (MC) simulation methods rely on equilibrium statistical mechanics to evaluate the relative stability of system states and explore the update of molecular conformations, without considering how a molecular conformation would change from one state to another from a physics perspective. Particularly, Grand Canonical Monte Carlo (GCMC) methods as implemented in RASPA are useful to predict adsorption properties in the area of nanoporous materials.[97-98]

1.3.2.2 Molecular Dynamics Simulation

Molecular dynamics (MD) simulation methods generate molecular conformations by solving the classical equations of motion according to Newton's laws based on developed potential function. Time evolution of molecular system is then determined by solving above equations with solved successive sets of atom coordinates and atom velocities. Diffusivities of small molecules can be calculated from MD simulations.[99]

1.4 References

1. Long, J. R.; Yaghi, O. M., The pervasive chemistry of metal-organic frameworks. *Chemical Society reviews* **2009,** *38* (5), 1213-4.

2. O'Keeffe, M., Design of MOFs and intellectual content in reticular chemistry: a personal view. *Chemical Society reviews* **2009,** *38* (5), 1215-7.

3. Banerjee, D.; Simon, C. M.; Elsaidi, S. K.; Haranczyk, M.; Thallapally, P. K., Xenon Gas Separation and Storage Using Metal-Organic Frameworks. *Chem* **2018,** *4* (3), 466-494.

4. Wang, C. Y.; Wang, L. X.; Belnick, A.; Wang, H.; Li, J.; Lueking, A. D., Oxygen-selective adsorption in RPM_3-Zn metal organic framework. *Chemical Engineering Science* **2017,** *165*, 122-130.

5. Guo, Z. J.; Yu, J. M.; Zhang, Y. Z.; Zhang, J.; Chen, Y.; Wu, Y. F.; Xie, L. H.; Li, J. R., Water-Stable In(III)-Based Metal-Organic Frameworks with Rod-Shaped Secondary Building Units: Single-Crystal to Single-Crystal Transformation and Selective Sorption of C_2H_2 over CO_2 and CH_4. *Inorganic Chemistry* **2017,** *56* (4), 2188-2197.

6. Millward, A. R.; Yaghi, O. M., Metal-organic frameworks with exceptionally high capacity for storage of carbon dioxide at room temperature. *Journal of the American Chemical Society* **2005,** *127* (51), 17998-17999.

7. Kuppler, R. J.; Timmons, D. J.; Fang, Q. R.; Li, J. R.; Makal, T. A.; Young, M. D.; Yuan, D. Q.; Zhao, D.; Zhuang, W. J.; Zhou, H. C., Potential applications of metal-organic frameworks. *Coordination Chemistry Reviews* **2009,** *253* (23-24), 3042-3066.

8. Yang, H. Q.; Xu, Z. H.; Fan, M. H.; Gupta, R.; Slimane, R. B.; Bland, A. E.; Wright, I., Progress in carbon dioxide separation and capture: A review. *Journal of Environmental Sciences* **2008,** *20* (1), 14-27.

9. Haldoupis, E.; Nair, S.; Sholl, D. S., Efficient Calculation of Diffusion Limitations in Metal Organic Framework Materials: A Tool for Identifying Materials for Kinetic Separations. *Journal of the American Chemical Society* **2010,** *132* (21), 7528-7539.

10. Czaja, A. U.; Trukhan, N.; Muller, U., Industrial applications of metal-organic frameworks. *Chemical Society reviews* **2009,** *38* (5), 1284-1293.

11. Lee, J.; Farha, O. K.; Roberts, J.; Scheidt, K. A.; Nguyen, S. T.; Hupp, J. T., Metal-organic framework materials as catalysts. *Chemical Society reviews* **2009,** *38* (5), 1450-1459.

12. Achmann, S.; Hagen, G.; Kita, J.; Malkowsky, I. M.; Kiener, C.; Moos, R., Metal-Organic Frameworks for Sensing Applications in the Gas Phase. *Sensors* **2009,** *9* (3), 1574-1589.

13. Nalaparaju, A.; Jiang, J. W., Recovery of Dimethyl Sulfoxide from Aqueous Solutions by Highly Selective Adsorption in Hydrophobic Metal-Organic Frameworks. *Langmuir : the ACS journal of surfaces and colloids* **2012,** *28* (43), 15305-15312.

14. Haque, E.; Jun, J. W.; Jhung, S. H., Adsorptive removal of methyl orange and methylene blue from aqueous solution with a metal-organic framework material, iron terephthalate (MOF-235). *Journal of Hazardous Materials* **2011,** *185* (1), 507-511.

15. Patil, D. V.; Rallapalli, P. B. S.; Dangi, G. P.; Tayade, R. J.; Somani, R. S.; Bajaj, H. C., MIL-53(AI): An Efficient Adsorbent for the Removal of Nitrobenzene from Aqueous Solutions. *Industrial & Engineering Chemistry Research* **2011,** *50* (18), 10516-10524.

16. Furukawa, H.; Cordova, K. E.; O'Keeffe, M.; Yaghi, O. M., The Chemistry and Applications of Metal-Organic Frameworks. *Science* **2013,** *341* (6149), 974-+.

17. Wilmer, C. E.; Leaf, M.; Lee, C. Y.; Farha, O. K.; Hauser, B. G.; Hupp, J. T.; Snurr, R. Q., Large-scale screening of hypothetical metal-organic frameworks. *Nature chemistry* **2012,** *4* (2), 83-89.

18. Caskey, S. R.; Wong-Foy, A. G.; Matzger, A. J., Dramatic tuning of carbon dioxide uptake via metal substitution in a coordination polymer with cylindrical pores. *Journal of the American Chemical Society* **2008,** *130* (33), 10870-+.

19. Furukawa, H.; Ko, N.; Go, Y. B.; Aratani, N.; Choi, S. B.; Choi, E.; Yazaydin, A. O.; Snurr, R. Q.; O'Keeffe, M.; Kim, J.; Yaghi, O. M., Ultrahigh Porosity in Metal-Organic Frameworks. *Science* **2010,** *329* (5990), 424-428.

20. Farha, O. K.; Yazaydin, A. O.; Eryazici, I.; Malliakas, C. D.; Hauser, B. G.; Kanatzidis, M. G.; Nguyen, S. T.; Snurr, R. Q.; Hupp, J. T., De novo synthesis of a metal-organic framework material featuring ultrahigh surface area and gas storage capacities. *Nature chemistry* **2010,** *2* (11), 944-948.

21. Wong-Foy, A. G.; Matzger, A. J.; Yaghi, O. M., Exceptional H_2 saturation uptake in microporous metal-organic frameworks. *Journal of the American Chemical Society* **2006,** *128* (11), 3494-3495.

22. Matsuda, R.; Kitaura, R.; Kitagawa, S.; Kubota, Y.; Belosludov, R. V.; Kobayashi, T. C.; Sakamoto, H.; Chiba, T.; Takata, M.; Kawazoe, Y.; Mita, Y., Highly controlled acetylene accommodation in a metal-organic microporous material. *Nature* **2005,** *436* (7048), 238-241.

23. Zhu, L.; Liu, X. Q.; Jiang, H. L.; Sun, L. B., Metal-Organic Frameworks for Heterogeneous Basic Catalysis. *Chemical reviews* **2017,** *117* (12), 8129-8176.

24. Alaerts, L.; Seguin, E.; Poelman, H.; Thibault-Starzyk, F.; Jacobs, P. A.; De Vos, D. E., Probing the Lewis acidity and catalytic activity of the metal-organic framework $Cu_3(btc)_2$ (BTC = benzene-1,3,5-tricarboxylate). *Chemistry-a European Journal* **2006,** *12* (28), 7353-7363.

25. Phan, A.; Czaja, A. U.; Gandara, F.; Knobler, C. B.; Yaghi, O. M., Metal-Organic Frameworks of Vanadium as Catalysts for Conversion of Methane to Acetic Acid. *Inorganic Chemistry* **2011,** *50* (16), 7388-7390.

26. Park, K. S.; Ni, Z.; Cote, A. P.; Choi, J. Y.; Huang, R. D.; Uribe-Romo, F. J.; Chae, H. K.; O'Keeffe, M.; Yaghi, O. M., Exceptional chemical and thermal stability of zeolitic imidazolate frameworks. *Proceedings of the National Academy of Sciences of the United States of America* **2006,** *103* (27), 10186-10191.

27. Cavka, J. H.; Jakobsen, S.; Olsbye, U.; Guillou, N.; Lamberti, C.; Bordiga, S.; Lillerud, K. P., A new zirconium inorganic building brick forming metal organic frameworks with exceptional stability. *Journal of the American Chemical Society* **2008,** *130* (42), 13850-13851.

28. Kandiah, M.; Nilsen, M. H.; Usseglio, S.; Jakobsen, S.; Olsbye, U.; Tilset, M.; Larabi, C.; Quadrelli, E. A.; Bonino, F.; Lillerud, K. P., Synthesis and Stability of Tagged UiO-66 Zr-MOFs. *Chemistry of Materials* **2010,** *22* (24), 6632-6640.

29. Tozawa, T.; Jones, J. T. A.; Swamy, S. I.; Jiang, S.; Adams, D. J.; Shakespeare, S.; Clowes, R.; Bradshaw, D.; Hasell, T.; Chong, S. Y.; Tang, C.; Thompson, S.; Parker, J.; Trewin, A.; Bacsa, J.; Slawin, A. M. Z.; Steiner, A.; Cooper, A. I., Porous organic cages. *Nature materials* **2009,** *8* (12), 973-978.

30. Evans, J. D.; Sumby, C. J.; Doonan, C. J., Synthesis and Applications of Porous Organic Cages. *Chemistry Letters* **2015,** *44* (5), 582-588.

31. Slater, A. G.; Little, M. A.; Pulido, A.; Chong, S. Y.; Holden, D.; Chen, L.; Morgan, C.; Wu, X.; Cheng, G.; Clowes, R.; Briggs, M. E.; Hasell, T.; Jelfs, K. E.; Day, G. M.; Cooper, A. I., Reticular synthesis of porous molecular 1D nanotubes and 3D networks. *Nature chemistry* **2017,** *9* (1), 17-25.

32. Liu, M.; Chen, L. J.; Lewis, S.; Chong, S. Y.; Little, M. A.; Hasell, T.; Aldous, I. M.; Brown, C. M.; Smith, M. W.; Morrison, C. A.; Hardwick, L. J.; Cooper, A. I., Three-dimensional protonic conductivity in porous organic cage solids. *Nature communications* **2016,** *7*.

33. Hasell, T.; Culshaw, J. L.; Chong, S. Y.; Schmidtmann, M.; Little, M. A.; Jelfs, K. E.; Pyzer-Knapp, E. O.; Shepherd, H.; Adams, D. J.; Day, G. M.; Cooper, A. I., Controlling the Crystallization of Porous Organic Cages: Molecular Analogs of Isoreticular Frameworks Using Shape-Specific Directing Solvents. *Journal of the American Chemical Society* **2014,** *136* (4), 1438-1448.

34. Jin, Y. H.; Zhu, Y. L.; Zhang, W., Development of organic porous materials through Schiff-base chemistry. *Crystengcomm* **2013,** *15* (8), 1484-1499.

35. Hasell, T.; Cooper, A. I., Porous organic cages: soluble, modular and molecular pores. *Nature Reviews Materials* **2016,** *1* (9).

36. Belowich, M. E.; Stoddart, J. F., Dynamic imine chemistry. *Chemical Society reviews* **2012,** *41* (6), 2003-2024.

37. Zhu, G.; Liu, Y.; Flores, L.; Lee, Z. R.; Jones, C. W.; Dixon, D. A.; Sholl, D. S.; Lively, R. P., Formation Mechanisms and Defect Engineering of Imine-Based Porous Organic Cages. *Chemistry of Materials* **2018,** *30* (1), 262-272.

38. Lucero, J.; Elsaidi, S. K.; Anderson, R.; Wu, T.; Gómez-Gualdrón, D. A.; Thallapally, P. K.; Carreon, M. A., Time Dependent Structural Evolution of Porous Organic Cage CC3. *Crystal Growth & Design* **2018,** *18* (2), 921-927.

39. Holst, J. R.; Trewin, A.; Cooper, A. I., Porous organic molecules. *Nature chemistry* **2010,** *2* (11), 915-920.

40. Briggs, M. E.; Cooper, A. I., A Perspective on the Synthesis, Purification, and Characterization of Porous Organic Cages. *Chemistry of Materials* **2017,** *29* (1), 149-157.

41. Jelfs, K. E.; Cooper, A. I., Molecular simulations to understand and to design porous organic molecules. *Current Opinion in Solid State and Materials Science* **2013,** *17* (1), 19-30.

42. Cooper, A. I., Nanoporous Organics Enter the Cage Age. *Angewandte Chemie-International Edition* **2011,** *50* (5), 996-998.

43. Evans, J. D.; Jelfs, K. E.; Day, G. M.; Doonan, C. J., Application of computational methods to the design and characterisation of porous molecular materials. *Chemical Society reviews* **2017**.

44. Cooper, A. I., Porous Molecular Solids and Liquids. *ACS Central Science* **2017,** *3* (6), 544-553.

45. Pulido, A.; Chen, L. J.; Kaczorowski, T.; Holden, D.; Little, M. A.; Chong, S. Y.; Slater, B. J.; McMahon, D. P.; Bonillo, B.; Stackhouse, C. J.; Stephenson, A.; Kane, C. M.; Clowes, R.; Hasell, T.; Cooper, A. I.; Day, G. M., Functional materials discovery using energy-structure-function maps. *Nature* **2017,** *543* (7647), 657-+.

46. Kong, X.; Jiang, J. W., Porous organic cage membranes for water desalination: a simulation exploration. *Physical Chemistry Chemical Physics* **2017,** *19* (28), 18178-18185.

47. Song, Q.; Jiang, S.; Hasell, T.; Liu, M.; Sun, S.; Cheetham, A. K.; Sivaniah, E.; Cooper, A. I., Porous Organic Cage Thin Films and Molecular-Sieving Membranes. *Advanced materials* **2016**.

48. Hasell, T.; Miklitz, M.; Stephenson, A.; Little, M. A.; Chong, S. Y.; Clowes, R.; Chen, L.; Holden, D.; Tribello, G. A.; Jelfs, K. E.; Cooper, A. I., Porous Organic Cages for Sulfur Hexafluoride Separation. *J Am Chem Soc* **2016,** *138* (5), 1653-9.

49. Kewley, A.; Stephenson, A.; Chen, L.; Briggs, M. E.; Hasell, T.; Cooper, A. I., Porous Organic Cages for Gas Chromatography Separations. *Chemistry of Materials* **2015,** *27* (9), 3207-3210.

50. Chen, L.; Reiss, P. S.; Chong, S. Y.; Holden, D.; Jelfs, K. E.; Hasell, T.; Little, M. A.; Kewley, A.; Briggs, M. E.; Stephenson, A.; Thomas, K. M.; Armstrong, J. A.; Bell, J.; Busto, J.; Noel, R.; Liu, J.; Strachan, D. M.; Thallapally, P. K.; Cooper, A. I., Separation of rare gases and chiral molecules by selective binding in porous organic cages. *Nature materials* **2014,** *13* (10), 954-60.

51. Mitra, T.; Jelfs, K. E.; Schmidtmann, M.; Ahmed, A.; Chong, S. Y.; Adams, D. J.; Cooper, A. I., Molecular shape sorting using molecular organic cages. *Nature chemistry* **2013,** *5* (4), 276-81.

52. Camp, J. S.; Sholl, D. S., Transition State Theory Methods To Measure Diffusion in Flexible Nanoporous Materials: Application to a Porous Organic Cage Crystal. *The Journal of Physical Chemistry C* **2016,** *120* (2), 1110-1120.

53. Hasell, T.; Miklitz, M.; Stephenson, A.; Little, M. A.; Chong, S. Y.; Clowes, R.; Chen, L. J.; Holden, D.; Tribello, G. A.; Jelfs, K. E.; Cooper, A. I., Porous Organic Cages for Sulfur Hexafluoride Separation. *Journal of the American Chemical Society* **2016,** *138* (5), 1653-1659.

54. Evans, J. D.; Huang, D. M.; Hill, M. R.; Sumby, C. J.; Thornton, A. W.; Doonan, C. J., Feasibility of Mixed Matrix Membrane Gas Separations Employing Porous Organic Cages. *The Journal of Physical Chemistry C* **2014,** *118* (3), 1523-1529.

55. Jiang, S.; Chen, L.; Briggs, M. E.; Hasell, T.; Cooper, A. I., Functional porous composites by blending with solution-processable molecular pores. *Chemical communications* **2016,** *52* (42), 6895-6898.

56. Jiang, S.; Jones, J. T.; Hasell, T.; Blythe, C. E.; Adams, D. J.; Trewin, A.; Cooper, A. I., Porous organic molecular solids by dynamic covalent scrambling. *Nature communications* **2011,** *2*, 207.

57. Jones, J. T.; Hasell, T.; Wu, X.; Bacsa, J.; Jelfs, K. E.; Schmidtmann, M.; Chong, S. Y.; Adams, D. J.; Trewin, A.; Schiffman, F.; Cora, F.; Slater, B.; Steiner, A.; Day, G. M.; Cooper, A. I., Modular and predictable assembly of porous organic molecular crystals. *Nature* **2011,** *474* (7351), 367-71.

58. Jelfs, K. E.; Schiffmann, F.; Jones, J. T. A.; Slater, B.; Cora, F.; Cooper, A. I., Conformer interconversion in a switchable porous organic cage. *Physical Chemistry Chemical Physics* **2011,** *13* (45), 20081-20085.

59. Jelfs, K. E.; Wu, X. F.; Schmidtmann, M.; Jones, J. T. A.; Warren, J. E.; Adams, D. J.; Cooper, A. I., Large Self-Assembled Chiral Organic Cages: Synthesis, Structure, and Shape Persistence. *Angewandte Chemie-International Edition* **2011,** *50* (45), 10653-10656.

60. Hasell, T.; Chong, S. Y.; Jelfs, K. E.; Adams, D. J.; Cooper, A. I., Porous Organic Cage Nanocrystals by Solution Mixing. *Journal of the American Chemical Society* **2012,** *134* (1), 588-598.

61. Hazen, R. M.; Sholl, D. S., Chiral selection on inorganic crystalline surfaces. *Nature materials* **2003,** *2* (6), 367-374.

62. Lee, H. E.; Ahn, H. Y.; Mun, J.; Lee, Y. Y.; Kim, M.; Cho, N. H.; Chang, K.; Kim, W. S.; Rho, J.; Nam, K. T., Amino-acid- and peptide-directed synthesis of chiral plasmonic gold nanoparticles. *Nature* **2018,** *556* (7701), 360-+.

63. Cooper, A. I.; Day, G. M.; Jones, J. T. A.; Wu, X. F.; Hasell, T.; Bacsa, J.; Jelfs, K. E.; Scmidtmann, M.; Chong, S. Y.; Trewin, A.; Schiffman, F.; Cora, F.; Slater, B.; Steiner, A., Modular and predictable assembly of porous organic molecular crystals. *Abstracts of Papers of the American Chemical Society* **2011,** *242*.

64. Hasell, T.; Chong, S. Y.; Schmidtmann, M.; Adams, D. J.; Cooper, A. I., Porous Organic Alloys. *Angewandte Chemie-International Edition* **2012,** *51* (29), 7154-7157.

65. Hasell, T.; Little, M. A.; Chong, S. Y.; Schmidtmann, M.; Briggs, M. E.; Santolini, V.; Jelfs, K. E.; Cooper, A. I., Chirality as a tool for function in porous organic cages. *Nanoscale* **2017,** *9* (20), 6783-6790.

66. Bennett, T. D.; Cheetham, A. K.; Fuchs, A. H.; Coudert, F.-X., Interplay between defects, disorder and flexibility in metal-organic frameworks. *Nat. Chem.* **2017,** *9* (1), 11-16.

67. Sholl, D. S.; Lively, R. P., Defects in Metal–Organic Frameworks: Challenge or Opportunity? *J. Phys. Chem. Lett.* **2015,** *6* (17), 3437-3444.

68. Hasell, T.; Schmidtmann, M.; Stone, C. A.; Smith, M. W.; Cooper, A. I., Reversible water uptake by a stable imine-based porous organic cage. *Chemical communications* **2012,** *48* (39), 4689-4691.

69. Yu, J.; Ma, Y.; Balbuena, P. B., Evaluation of the impact of H_2O, O_2, and SO_2 on postcombustion CO_2 capture in metal-organic frameworks. *Langmuir : the ACS journal of surfaces and colloids* **2012,** *28* (21), 8064-71.

70. Sholl, D. S.; Lively, R. P., Defects in Metal-Organic Frameworks: Challenge or Opportunity? *J Phys Chem Lett* **2015**, 3437-3444.

71. Burtch, N. C.; Jasuja, H.; Walton, K. S., Water stability and adsorption in metal-organic frameworks. *Chemical reviews* **2014,** *114* (20), 10575-612.

72. Howarth, A. J.; Liu, Y.; Li, P.; Li, Z.; Wang, T. C.; Hupp, J. T.; Farha, O. K., Chemical, thermal and mechanical stabilities of metal–organic frameworks. *Nature Reviews Materials* **2016,** *1* (3), 15018.

73. Jiao, Y.; Morelock, C. R.; Burtch, N. C.; Mounfield, W. P.; Hungerford, J. T.; Walton, K. S., Tuning the Kinetic Water Stability and Adsorption Interactions of Mg-MOF-74 by Partial Substitution with Co or Ni. *Industrial & Engineering Chemistry Research* **2015,** *54* (49), 12408-12414.

74. Taylor, J. M.; Vaidhyanathan, R.; Iremonger, S. S.; Shimizu, G. K. H., Enhancing Water Stability of Metal-Organic Frameworks via Phosphonate Monoester Linkers. *Journal of the American Chemical Society* **2012,** *134* (35), 14338-14340.

75. Wittmann, T.; Siegel, R.; Reimer, N.; Milius, W.; Stock, N.; Senker, J., Enhancing the Water Stability of Al-MIL-101-NH_2 via Postsynthetic Modification. *Chemistry-a European Journal* **2015,** *21* (1), 314-323.

76. Bellarosa, L.; Gutierrez-Sevillano, J. J.; Calero, S.; Lopez, N., How ligands improve the hydrothermal stability and affect the adsorption in the IRMOF family. *Physical Chemistry Chemical Physics* **2013,** *15* (40), 17696-17704.

77. Uemura, K.; Onishi, F.; Yamasaki, Y.; Kita, H., Syntheses, crystal structures, and water adsorption behaviors of jungle-gym-type porous coordination polymers containing nitro moieties. *Journal of Solid State Chemistry* **2009,** *182* (10), 2852-2857.

78. DeCoste, J. B.; Peterson, G. W.; Jasuja, H.; Glover, T. G.; Huang, Y.-g.; Walton, K. S., Stability and degradation mechanisms of metal–organic frameworks containing the $Zr_6O_4(OH)_4$ secondary building unit. *Journal of Materials Chemistry A* **2013,** *1* (18), 5642.

79. Han, S.; Huang, Y.; Watanabe, T.; Nair, S.; Walton, K. S.; Sholl, D. S.; Carson Meredith, J., MOF stability and gas adsorption as a function of exposure to water, humid air, SO_2, and NO_2. *Microporous and Mesoporous Materials* **2013,** *173*, 86-91.

80. Mounfield, W. P.; Tumuluri, U.; Jiao, Y.; Li, M.; Dai, S.; Wu, Z.; Walton, K. S., Role of defects and metal coordination on adsorption of acid gases in MOFs and metal oxides: An in situ IR spectroscopic study. *Microporous and Mesoporous Materials* **2016,** *227*, 65-75.

81. Mounfield, W. P.; Han, C.; Pang, S. H.; Tumuluri, U.; Jiao, Y.; Bhattacharyya, S.; Dutzer, M. R.; Nair, S.; Wu, Z.; Lively, R. P.; Sholl, D. S.; Walton, K. S., Synergistic Effects of Water and SO_2 on Degradation of MIL-125 in the Presence of Acid Gases. *Journal of Physical Chemistry C* **2016,** *120* (48), 27230-27240.

82. Pang, S. H.; Han, C.; Sholl, D. S.; Jones, C. W.; Lively, R. P., Facet-Specific Stability of ZIF-8 in the Presence of Acid Gases Dissolved in Aqueous Solutions. *Chemistry of Materials* **2016,** *28* (19), 6960-6967.

83. Bhattacharyya, S.; Pang, S. H.; Dutzer, M. R.; Lively, R. P.; Walton, K. S.; Sholl, D. S.; Nair, S., Interactions of SO_2-Containing Acid Gases with ZIF-8: Structural Changes and Mechanistic Investigations. *Journal of Physical Chemistry C* **2016,** *120* (48), 27221-27229.

84. Bhattacharyya, S.; Han, R.; Kim, W. G.; Chiang, Y. D.; Jayachandrababu, K. C.; Hungerford, J. T.; Dutzer, M. R.; Ma, C.; Walton, K. S.; Sholl, D. S.; Nair, S., Acid Gas Stability of Zeolitic Imidazolate Frameworks: Generalized Kinetic and Thermodynamic Characteristics. *Chemistry of Materials* **2018,** *30* (12), 4089-4101.

85. Mondloch, J. E.; Katz, M. J.; Planas, N.; Semrouni, D.; Gagliardi, L.; Hupp, J. T.; Farha, O. K., Are Zr_6-based MOFs water stable? Linker hydrolysis vs. capillary-force-driven channel collapse. *Chemical communications* **2014,** *50* (64), 8944-6.

86. Küsgens, P.; Rose, M.; Senkovska, I.; Fröde, H.; Henschel, A.; Siegle, S.; Kaskel, S., Characterization of metal-organic frameworks by water adsorption. *Microporous and Mesoporous Materials* **2009,** *120* (3), 325-330.

87. Ming, Y.; Purewal, J.; Yang, J.; Xu, C.; Soltis, R.; Warner, J.; Veenstra, M.; Gaab, M.; Muller, U.; Siegel, D. J., Kinetic Stability of MOF-5 in Humid Environments: Impact of Powder Densification, Humidity Level, and Exposure Time. *Langmuir : the ACS journal of surfaces and colloids* **2015,** *31* (17), 4988-95.

88. Low, J. J.; Benin, A. I.; Jakubczak, P.; Abrahamian, J. F.; Faheem, S. A.; Willis, R. R., Virtual High Throughput Screening Confirmed Experimentally: Porous Coordination Polymer Hydration. *Journal of the American Chemical Society* **2009,** *131* (43), 15834-15842.

89. Tumuluri, U.; Li, M.; Cook, B. G.; Sumpter, B.; Dai, S.; Wu, Z., Surface Structure Dependence of SO_2 Interaction with Ceria Nanocrystals with Well-Defined Surface Facets. *Journal of Physical Chemistry C* **2015,** *119* (52), 28895-28905.

90. Landers, J.; Gor, G. Y.; Neimark, A. V., Density functional theory methods for characterization of porous materials. *Colloids and Surfaces a-Physicochemical and Engineering Aspects* **2013,** *437*, 3-32.

91. Connolly, J. W. D.; Williams, A. R., Density-Functional Theory Applied to Phase-Transformations in Transition-Metal Alloys. *Physical Review B* **1983,** *27* (8), 5169-5172.

92. Sham, L. J.; Schluter, M., Density-Functional Theory of the Energy-Gap. *Physical Review Letters* **1983,** *51* (20), 1888-1891.

93. Sholl, D. S.; J. A., Density Functional Theory: A Practical Introductionn; John Wiley & Sons, Inc.: Hoboken, NJ. **2011**.

94. Kresse, G.; Joubert, D., From ultrasoft pseudopotentials to the projector augmented-wave method. *Physical Review B* **1999,** *59* (3), 1758-1775.

95. Blochl, P. E., PROJECTOR AUGMENTED-WAVE METHOD. *Physical Review B* **1994,** *50* (24), 17953-17979.

96. Godbout, N.; Salahub, D. R.; Andzelm, J.; Wimmer, E., Optimization of Gaussian-type basis sets for local spin density functional calculations. Part I. Boron through neon, optimization technique and validation. *Canadian Journal of Chemistry* **1992,** *70* (2), 560-571.

97. Dubbeldam, D.; Calero, S.; Ellis, D. E.; Snurr, R. Q., RASPA: molecular simulation software for adsorption and diffusion in flexible nanoporous materials. *Molecular Simulation* **2016,** *42* (2), 81-101.

98. Gelb, L. D.; Gubbins, K. E., Pore size distributions in porous glasses: A computer simulation study. *Langmuir : the ACS journal of surfaces and colloids* **1999,** *15* (2), 305-308.

99. Frenkel, D.; Smit, B., Understanding Molecular Simulation, Second Edition: From Algorithms to Applications (Computational Science). *Academic Press* **2001**.

CHAPTER 2. ACID GAS INTERACTION WITH METAL-ORGANIC FRAMEWORK NANOSHEETS AS A MODEL OF AN "ALL-SURFACE" MATERIAL

2.1 Introduction*

Metal-Organic Frameworks (MOFs) as a novel class of nanoporous materials have received increasing research interest for potential use as adsorbent materials for gas separation and storage applications.[1-2] Most studies have focused on the bulk properties of MOFs. Recently, Sholl et al. highlighted the importance of MOF defects and noted that MOFs' external surfaces could potentially be a rich source for defects.[3] Undercoordinated sites can exist on the external surfaces of the MOFs, exposed to the surroundings.[4-6] It is possible, therefore, that MOF external surfaces are more reactive for degradation than the material's interior pores. This motivates an interest in understanding the external surfaces of MOFs at a fundamental level.

In order to develop an understanding of MOF external surfaces, it is desirable to study MOFs that are as close to materials that are dominated by external surfaces. Recently, MOF nanosheets that are two-dimensional analogs of the MOF-2 structure have been synthesized, known as M-BDC nanosheets, using Zn, Cu, and Co metals in place of the Zn ions of bulk MOF-2.[7-8] Figure 2.1 shows the bulk structure of MOF-2. M-BDC nanosheets are a case of an effectively all-surface MOF containing surface

* Results from this chapter have been published previously in Howe, J. D.; Liu, Y.; Flores, L.; Dixon, D. A.; Sholl, D. S., Acid Gas Adsorption on Metal-Organic Framework Nanosheets as a Model of an "All-Surface" Material. *Journal of Chemical Theory and Computation* **2017,** *13* (3), 1341-1350.

adsorption sites, especially undercoordinated open-metal sites (OMSs), which are not readily accessible in the analogous bulk MOF.[7] In this chapter, we create a sheet model of these M-BDC nanosheets extracted from the MOF-2 bulk structure to study acid gas and energy-relevant small molecules (CO, CO_2, H_2O, SO_2, NO_2, and H_2S) interactions with the surfaces of these materials.

Co-adsorption is a common phenomenon in gas adsorption. Co-adsorption is important to investigate particularly with the existence of water because there will be residual water present in nearly any adsorption applications where the adsorbent is exposed to ambient air. Most co-adsorption studies have focused on the effects of trace gases on CO_2 adsorption in MOFs. Yu et al. investigated the influence of CO, H_2O, N_2, NO, NO_2, SO_2, SO_3, H_2SO_3, H_2SO_4, HNO_2, and HNO_3 on the CO_2 adsorption to Mg-MOF-74 and MIL-101, and found that acid gases and their hydrates could dramatically poison the open-metal sites in these MOFs.[9] Yu et al. concluded that the presence of water decreased CO_2 adsorption capacity in Mg-MOF-74.[10] On the contrary, Snurr et al. predicted that a small amount of preadsorbed water enhanced CO_2 adsorption capacity and selectivity over N_2 and CH_4 in another structure with OMS, HKUST-1.[11] Recently, Tan et al. argued that the co-adsorption of small molecules on the OMS within M-MOF-74 (M=Mg, Co, Ni) was controlled by kinetics, not just binding energies.[12] Aside from studying the most favorable binding site, OMS in MOFs, Yu et al. also studied how water and SO_2 impurities affected CO_2 adsorption and separation in various linkers within modified UiO-66(Zr) with $-NH_2$, $-OH$, and -Br functional groups.[13] Even fewer studies have explored the influence of the presence of water on the adsorption of acid gases. To fill in above gap, we further explored the adsorption behaviors of a set of acid gases to

the exposed OMS at Cu-BDC nanosheet in the presence of water, including competitive co-adsorption phenomenon and cooperative co-adsorption phenomenon.

In addition to exploring physical co-adsorption behavior of acid gases and water on Cu-BDC nanosheet, it is also essential to investigate possible chemical adsorptive reaction that would be involved when exploiting the use of these materials in the acidic environment. Many contaminants are commonly found in industrial processes, including high humidity and acid gases. In the presence of relatively high humidity, acid gases can react with H_2O to form acid hydrates that have higher acidity, which would potentially cause the material degradation. In this work, we proposed and examined detailed degradation pathways and degradation reaction energetics for Cu-BDC nanosheets under humid acid gas exposure, specifically H_2SO_3 attack.

2.2 Methods and Computational Details

2.2.1 Density Functional Theory (DFT) Calculations

DFT calculations are performed in the Vienna Ab initio Simulation Package (VASP) with a planewave basis set and core electrons represented with projector augmented wave (PAW) potentials.[14-15] For all DFT calculations, we use the Perdew−Burke−Ernzerhof (PBE) exchange-correlation functional plus the second version of a van der Waals dispersion-corrected density functional (vdW-DF2) to capture van der Waals dispersion interactions between guest molecules and OMS within MOFs.[16-17] To address on-site Coulomb effects, we use Hubbard U corrections for the d electrons of the Cu and Co ions, with U values of 4.0 eV and 3.3 eV, respectively.[18-19] During binding geometry relaxation, only the atomic positions are optimized until atomic forces were

less than 0.01 eV/ Å; while in the climbing Nudged Elastic Band (NEB) calculations, the convergence criteria was to continue until atomic forces were less than 0.05 eV/ Å.[20-21]

2.2.2 Adsorption Energy Calculations

Acid gases and relevant small molecules (CO, CO_2, H_2O, SO_2, NO_2, and H_2S) adsorption energies on M-BDC nanosheets (M = Zn, Cu, and Co) are calculated as

$$\Delta E = E_{MOF+mol} - E_{MOF} - E_{mol}$$

where ΔE is the molecule adsorption energy, with a negative sign corresponding to an exothermic adsorption, $E_{MOF+mol}$ is the energy of MOF-plus-molecule adduct, E_{MOF} is the energy of bare MOF nanosheet, and E_{mol} is the energy of isolated molecule.

2.2.3 Formation Energy Calculations

The formation energies associated with each step along the proposed degradation pathway were calculated as

$$\Delta E_{formation} = E_{MOF+H_2SO_3+(H_2O)} - E_{MOF} - E_{H_2SO_3} - (E_{H_2O})$$

where $\Delta E_{formation}$ is the reaction formation energy, with a negative sign corresponding to an exothermic reaction, $E_{MOF+H_2SO_3+(H_2O)}$ is the energy of degradation configuration of each reaction step along proposed pathway, E_{MOF} is the energy of bare MOF nanosheet, and $E_{H_2SO_3}(E_{H_2O})$ is the energy of isolated H_2SO_3 (H_2O).

2.2.4 Adsorption Spectroscopic Property calculations

In addition to adsorption energies, heats of adsorption associated with small molecule adsorption on M-BDC nanosheets at room temperature are predicted by including thermal and quantum nuclear zero-point energy corrections with a harmonic approximation. Vibrational frequencies are calculated via a finite difference method to obtain a Hessian matrix of second-order derivatives of mode energies with a displacement of each atom of the adsorbed species symmetrically by 0.015 Å along each Cartesian axis. To obtain frequency shifts, we compare vibrational modes of molecules in the MOF-plus-molecule adducts with the vibrational modes of isolated molecules in 20 Å side-length cubic cells.

2.3 Pure Acid Gas Component Adsorption on M-BDC Nanosheets

2.3.1 M-BDC Nanosheet Models

We investigated acid gas interaction with the undercoordinated OMS of MOF-2-like M-BDC nanosheets by developing a model of these nanosheets based on the bulk MOF-2 crystal structure. Because MOF-2 naturally has a layered structure where adjacent layers are held together by dispersion and electrostatic interactions, we selected our model as a single layer of exfoliated MOF-2 (shown in Figure 2.1(a)). Table 2.1 shows the structure parameters of both bulk M-MOF-2 structures and energy-optimized M-BDC nanosheets (M=Zn, Cu, and Co). The structure parameters included for comparison are illustrated in Figure 2.1 (b). Comparing the bulk M-MOF-2 structures to M-BDC nanosheet models, the M-M distances (thickness) were slightly contracted in nanosheet models due to a lack of intersheet interactions that are present in bulk MOF-2.

Overall, the M-BDC nanosheets are similar to the corresponding bulk MOF-2 structures; therefore, these nanosheet models were selected as the external surface of MOF-2 materials for further use in the study of acid gas interactions.

For Cu-BDC and Co-BDC, all reasonable spin state orderings were considered for each metal ion within a single unit cell. There are two pairs of dimer ion centers and thus four unique metal ions in a single unit cell. Through energy optimization calculations for the structures of all potential spin state orderings, we found that the metal ions from different dimer centers that are separated by a linker showed a negligible effect of spin alignment (energy differences of ~1 meV) and the metal ions from the same dimer center preferred an antiferromagnetic state by roughly 70 meV (7 kJ/mol). This spin state ordering preference result is consistent with the previous work that $Cu_3(BTC)_2$ showed antiferromagnetic state within each Cu dimer center.[22]

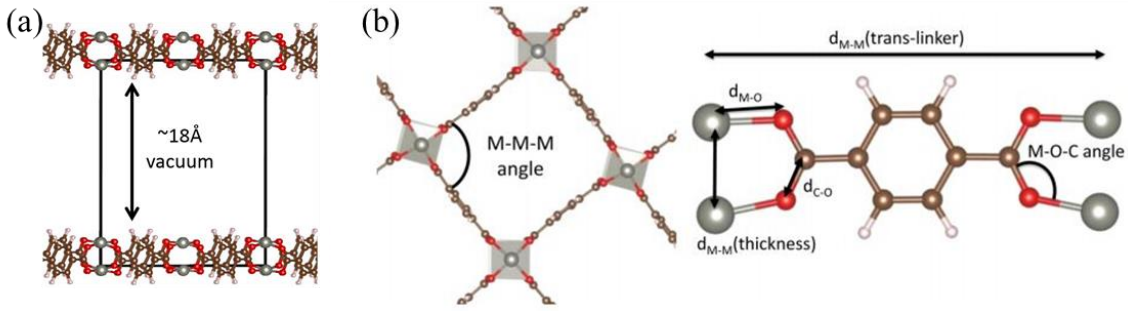

Figure 2.1 (a) Periodic model for Zn-BDC nanosheets with the box showing the unit cell. (b) Overview of structural parameters of Zn-BDC nanosheet that are used for comparing bulk and nanosheet structures.

Table 2.1 Comparison of bulk MOF-2 structure and calculated M-BDC structures.

	M-M-M angle [°]	**d_{M-M} (thickness) [Å]**	**d_{M-M} (trans-linker) [Å]**	**d_{M-O} [Å]**	**d_{C-O} [Å]**	**M-O-C angle [°]**
Zn-MOF-2	89.0-90.3	2.68	10.99,11.11	2.05-2.06	1.29	118.5-126.6
Cu-MOF-2	89.1-90.3	2.52	10.89, 11.01	1.99-2.00	1.29	118.8-122.6
Co-MOF-2	88.9-90.5	2.66	10.94, 11.09	2.03-2.04	1.29	119.8-126.5
Zn-BDC	89.0-91.7	2.63	10.95, 11.13	2.05-2.06	1.29	113.8-131.5
Cu-BDC	89.3-91.3	2.51	10.88, 11.02	1.99-2.00	1.29	118.4-122.7
Co-BDC	89.5-90.8	2.74	10.95, 11.03	2.00-2.06	1.29	114.5-134.9

2.3.2 Adsorption of Acid Gases

Using the nanosheet models we developed, the interaction of small molecules with the MOF's undercoordinated OMS were studied. For each molecule, various binding motifs (MOF-plus-molecule adduct) were relaxed by DFT calculations, and only the lowest-energy configuration was taken for further study, as shown in Figure 2.2, which takes adsorption motif on a Zn-BDC nanosheet as an example. The binding energies on M-BDC were summarized in Table 2.2. In addition to binding energies, we also calculated the binding enthalpies at the level of a harmonic approximation, summarized in Table 2.2. We expect that these calculated binding enthalpies are more

directly comparable to experimentally measured heats of adsorption. Overall, we observed that small molecules were adsorbed more strongly on Zn-BDC and Co-BDC than Cu-BDC for nearly all species, as a result of the specific electronic structure of Cu ion (d^9). For each nanosheet, SO_2, H_2O and H_2S have higher binding strength than CO, CO_2, and NO_2, in agreement with previous work result on small molecule adsorption on M-MOF-74 (M = Mg, Ti, V, Cr, Mn, Fe, Co, Ni, Cu, and Zn).[23]

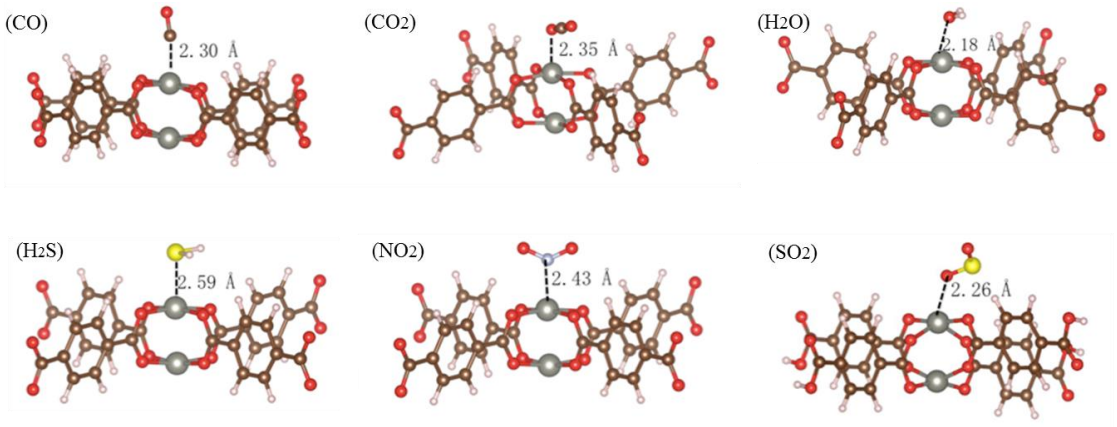

Figure 2.2 Binding motifs of CO, CO_2, H_2O, H_2S, NO_2, and SO_2 on Zn-BDC nanosheet.

Table 2.2 Binding energies (binding enthalpies) [kJ/mol] of CO, CO_2, H_2O, H_2S, NO_2, and SO_2 on M-BDC sheets. Acid gases are ordered by increasing strength of adsorption to Zn-BDC.

Metal identity	NO_2	CO_2	CO	H_2S	H_2O	SO_2
Zn-BDC	24 (22)	42 (40)	52 (48)	76 (70)	83 (76)	136 (130)
Cu-BDC	18 (15)	26 (24)	27 (24)	39 (35)	46 (40)	38 (36)
Co-BDC	57 (53)	43 (41)	47 (42)	34 (28)	79 (71)	64 (61)

2.3.3 Spectroscopic Properties

In tandem with our analysis of adsorption energetics, we calculated the vibrational frequency of the normal modes of the small molecules before and upon adsorption. The frequency shifts upon adsorption are presented in Table 2.3. Overall, the stronger H_2O showed one of the largest red shifts and also the highest strong adsorption energetics. The only outlier is NO_2, which shows the largest red shift as a result of a significant change in its electronic structure resulted from orbital interactions between unpaired electrons on NO_2 and the OMSs. We also observed a notable blue shift of the CO vibrational mode, contributed via back π bonding, consistent with previous work on CO adsorption at OMSs in MOF-74.[24]

Table 2.3 Frequency shifts of normal vibrational modes of small molecules upon adsorption on M-BDC nanosheets.

Molecule	Mode	Zn-BDC	Cu-BDC	Co-BDC
CO	stretch	60	27	3
CO_2	asymmetric stretch	-1	-5	-4
	symmetric stretch	-4	-2	-4
	bend	-11	-7	-12
H_2O	asymmetric	-66	-40	-61
	symmetric stretch	-54	-31	-73
	bend	3	1	-4
H_2S	asymmetric strech	-21	-10	-11
	symmetric stretch	-19	-10	-13
	bend	-9	-4	-10
NO_2	asymmetric strech	-117	-25	-99
	symmetric stretch	-105	-28	-63
	bend	-52	-14	4
SO_2	asymmetric stretch	-45	-29	-49
	symmetric stretch	-41	-17	-51
	bend	3	1	17

2.3.4 Co-adsorption of Pure Gases and Loading Effects

All of the calculations presented above focused on adsorption of a single acid gas molecule at an OMS on a M-BDC nanosheet, while adsorption on actual nanosheets will also include possibilities of co-adsorption at a single site or multiple sites. Additionally, the sheet models ued above include only a single layer of MOF-2-like structure as a representation of the M-BDC nanosheets, while actual nanosheets are not merely one layer thick. We have shown that our single-layer periodic model is able to represent bulk MOF-2 structure qualitatively. Here we further support the validity of such a single-layer model by demonstrating that adsorption energetics at a single primary binding site are not strongly changed when considering loading or co-adsorption phenomena.

To study loading effects, we considered NO_2, CO_2, CO, H_2S, and H_2O adsorbed to a primary binding site of Zn-BDC or Cu-BDC as well as two sites either of the same metal dimer or two sites on the same side of a sheet separated by a BDC linker. We denote these as trans-sheet and trans-linker, respectively. Table 2.4 shows the calculated average binding energies per single small molecule. Based on the comparison, we found negligible effects of loading on the strength of adsorption of small molecules on Zn-BDC and Cu-BDC nanosheets, supporting the validity of using a single-layer model for representing these nanosheets to explore the interactions between small molecules and M-BDC nanosheets.

Table 2.4 Comparison of average binding energies per single small molecule on primary binding site [kJ/ (mol × molecule)] to that on two sites of the same metal dimer and two sites on the same side of a sheet parted by a BDC linker on Zn-BDC and Cu-BDC nanosheets.

Metal Identity	Binding Motif	NO_2	CO_2	CO	H_2S	H_2O
Zn	single adsorbate	20	38	46	65	75
	trans-sheet	20	38	46	65	74
	trans-linker	20	38	46	65	75
Cu	single adsorbate	17	25	25	36	42
	trans-sheet	17	25	25	36	42
	trans-linker	17	25	25	36	42

To study co-adsorption, we considered the case of two CO molecules competing for adsorption at a single OMS on Zn-BDC, comparing the average binding energetics per CO molecule for binding motifs favoring a primary and secondary adsorption site, shown in Figure 2.3 (a), and the equidistant co-adsorption binding motif, shown in Figure 2.3 (b). DFT calculated average binding energetics per CO molecule under above binding motifs are presented in Table 2.5. The adsorption of a single molecule at a primary binding site is energetically the most favored configuration among all these binding motifs considered, and the loading of additional CO molecules onto Zn-BDC nanosheet is more likely to result in the occupation of a secondary binding site rather than fundamentally changing the nature of the primary binding site into equidistant co-adsorption binding sites. This supported our use of a single molecule at a primary binding site for purposes of understanding acid gas interactions with the surfaces of M-BDC nanosheets.

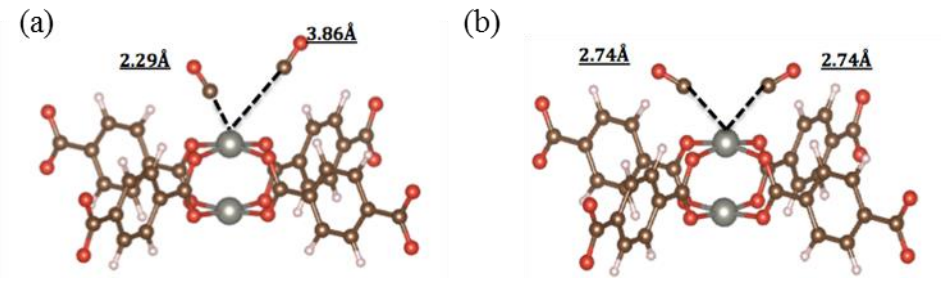

Figure 2.3 (a) Binding motif of two CO being adsorbed on a primary and secondary adsorption site, separately. (b) Binding motif of two CO being equidistant co-adsorbed at the primary binding site.

Table 2.5 Comparison of average binding energetics per CO molecule under various binding motifs, including single CO being adsorbed on primary binding site, two CO being equidistant co-adsorbed on one primary binding site, and two CO being adsorbed at a primary binding site and a secondary binding site.

System	Binding Energies kJ/ (mol × molecule)
Zn-BDC + CO	48
Zn-BDC + 2 CO (equidistant)	24
Zn-BDC + 2 CO (primary site-dominant)	31

2.4 Co-adsorption of Acid Gases with Water on Cu-BDC Nanosheet

2.4.1 Adsorption of Atmospheric Flue Gases

Purification of atmospheric flue gases which consist of CO, CO_2, NO_2, SO_2, H_2S, and H_2O was chosen as an example of an industrial application for the use of Cu-BDC nanosheets. With the presence of high relative humidity (>90%), in addition to acid gas contaminants, flue gases also potentially contain some level of acid hydrates, such as H_2SO_3, H_2SO_4, HNO_2, and HNO_3, which are compounds formed by the reactions between acid gases and water. Therefore, it is essential to consider how acid hydrates

interact with MOFs when MOFs are exposed to moist acid gases.[Error! Bookmark not defined.] The composition of briquette-fired flue gas was reported to be 21.3% CO_2, 12.8% O_2, 5.5% H_2O, 4.32ppm H_2S, 3.67 ppm SO_2, and 1.34ppm NO_x.[25] To perform some preliminary calculations, we assumed NO_2, HNO_2, HNO_3, H_2SO_3, and H_2SO_4 share the same concentration with NO_x and SO_2 respectively. We assumed that acid hydrates were formed in the gas phase before binding to MOFs. Binding energies of acid hydrates on Cu-BDC nanosheet were calculated using the same method that was used for calculating binding energies of acid gas to these nanosheets. Figure 2.4 shows the binding motif of H_2SO_3, H_2SO_4, HNO_2, and HNO_3 on Cu-BDC nanosheet and Table 2.6 presents the calculated corresponding binding energies. Even though the results demonstrated that the binding energies of acid hydrates were much higher than pure acid gas binding energies as a result of multiple interactions (oxygen atoms in acid hydrates interacted with OMSs and hydrogen atoms in acid hydrates interacted with oxygen atoms in BDC linkers), determining the most stable co-adsorption states on the external surface of Cu-BDC nanosheet upon humid acid gas treatment must consider the concentration of each species in the gas phase. We applied previously calculated binding energies of small molecules and acid hydrates into a Langmuir single-site competitive adsorption model ($\theta_A = \frac{K_A P_A}{1+\sum_i K_i P_i}$) to estimate the actual occupancy of OMS, θ_A, for each species (H_2O, CO_2, SO_2, NO_2, H_2S, H_2SO_3, H_2SO_4, HNO_2, and HNO_3) on the external surface of Cu-BDC nanosheet upon humid acid gas exposure (see Table 2.6). The calculated occupancies showed that even though the amount of SO_2 and its hydrates were small in the gas phase, they would dominate the equilibrium adsorption and bind to a large number of OMSs, especially for H_2SO_3 and H_2SO_4, as a result of their high binding strengths on OMSs.

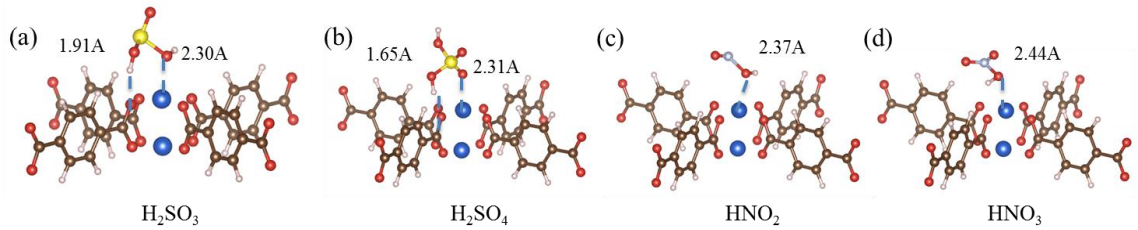

Figure 2.4 Binding motifs of (a) H_2SO_3, (b) H_2SO_4, (c) HNO_2, and (d) HNO_3 on CuBDC nanosheet.

Table 2.6 Small molecules and acid hydrates binding energies [kJ/mol], assumed concentration in the gas phase (% or ppm), and occupation of OMSs (%) on CuBDC nanosheet.

	H_2O	CO_2	SO_2	NO_2	H_2S	H_2SO_3	H_2SO_4	HNO_2	HNO_3
Binding Energy	-46	-26	-38	-18	-39	-69	-73	-43	-42
Conc.	5.5%	21.3%	3.67	1.34	4.32	3.67	3.67	1.34	1.34
OMS Occ.	17.14	0.02	$1x10^{-4}$	$<1x10^{-4}$	$2x10^{-4}$	13.25	69.59	$1x10^{-4}$	$1x10^{-4}$

2.4.2 Co-adsorption of Acid Gas and Water

The calculations presented so far have mainly focused on the adsorption of a single molecule onto OMSs in nanosheets, with the assumption of no dynamic reaction occurring among the adsorbed species at OMSs. However, actual MOF nanosheets have the possibility to allow reactive adsorption between by acid gases and water through either cooperative or competitive co-adsorption on OMSs.

To start with, it was useful to investigate whether acid gases preadsorbed at OMSs remain stable or or can be displaced by water molecules from the gas phase. We considered processes beginning with an acid gas adsorbed at an OMS and H_2O adsorbed

at the secondary binding site, and ending with water adsorbed at the OMS and acid gas adsorbed at a secondary binding site. Multiple candidate co-adsorption geometries were considered. Only the lowest-energy relaxed co-adsorption structure was further studied, shown in Figure 2.5. We applied Climbing Image NEB calculations to calculate the reaction pathways and energy barriers (including forward energy barriers as well as reverse energy barriers) for these processes, shown in Table 2.7. Figure 2.6 showed the reaction pathways of water replacement reactions for CO_2, SO_2, NO_2, and H_2S. The forward energy barrier calculations suggest that preadsorbed CO_2, SO_2, NO_2, and H_2S would be competitively replaced and pushed away from the OMS in the presence of water.

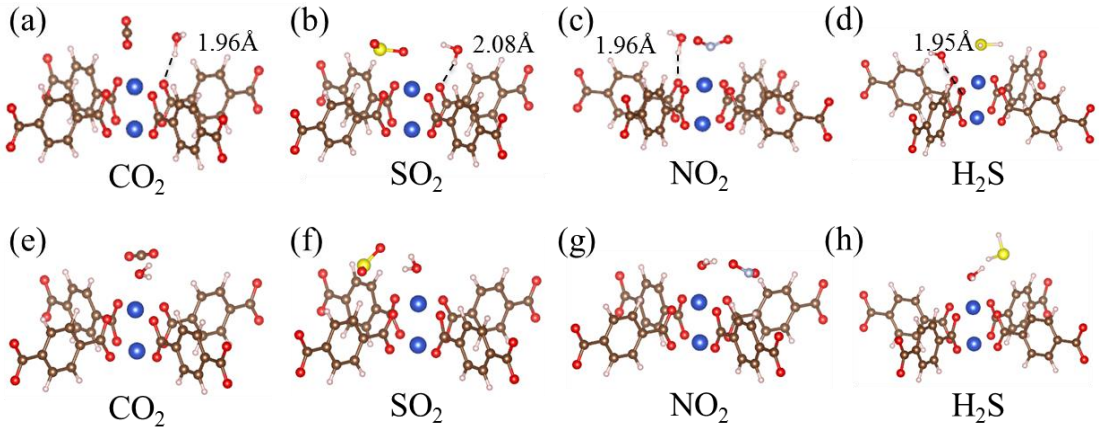

Figure 2.5 DFT relaxed co-adsorption configurations:(a) H_2O with preadsorbed CO_2, (b) H_2O with preadsorbed SO_2, (c) H_2O with preadsorbed NO_2, (d) H_2O with preadsorbed H_2S, (e) CO_2 with preadsorbed H_2O, (f) SO_2 with preadsorbed H_2O, (g) NO_2 with preadsorbed H_2O, (h) H_2S with preadsorbed H_2O.

Table 2.7 Calculated energy barriers (kJ/mol) for water displacement reactions for CO_2, SO_2, NO_2, and H_2S on Cu-BDC nanosheet.

	CO_2	SO_2	NO_2	H_2S
Forward Energy Barrier	12	5	68	11
Reverse Energy Barrier	24	28	91	16

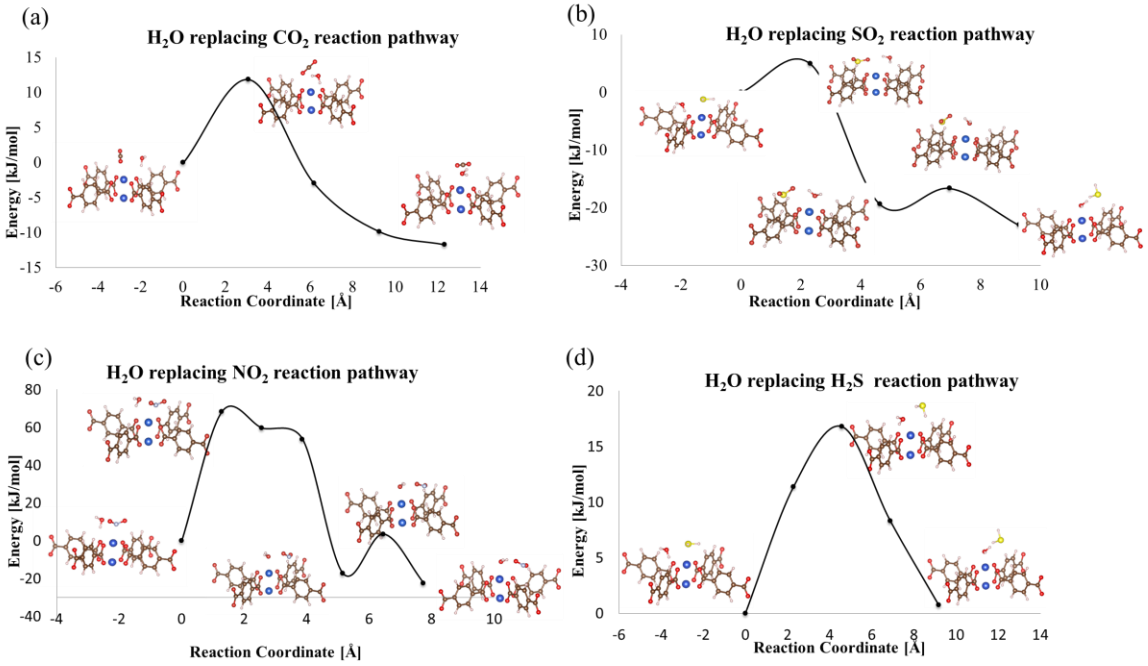

Figure 2.6 Water displacement reaction pathways of (a) CO_2, (b) SO_2, (c) NO_2, and (d) H_2S calculated using Climbing NEB methods.

The analysis above suggests that preadsorbed acid gases (CO_2, SO_2, NO_2, and H_2S) on Cu-BDC nanosheets would be replaced by water in the presence of water, leading to acid gas adsorbed on water coordinated OMSs instead of pure OMSs. Acid gas adsorption on water coordinated OMSs geometries were optimized and are shown in Figure 2.5(e) to Figure 2.5(h). The corresponding binding energies are shown in Table 2.8. For CO_2 and H_2S, the binding energies on water coordinated OMSs were lower than vacant OMSs, while for SO_2 and NO_2, the binding energies on water coordinated OMSs

were higher. The strong double hydrogen bonds established by two oxygen atoms in SO_2 and NO_2 and two hydrogen atoms in water contributed to the enhanced binding energies, while there was only one hydrogen bond formed in CO_2 co-adsorption, and none in H_2S co-adsorption. Even though water has a high probability to compete with acid gas for the same adsorption site and possibly replace preadsorbed acid gases, pre-adsorbing a small amount of water can increase the binding strength and attack on Cu-BDC nanosheet in the cases of SO_2 and NO_2.

Table 2.8 Comparison between binding energies of acid gases onto pure OMSs and that of acid gases onto water coordinated OMSs on Cu-BDC nanosheets.

Binding energies ΔE [kJ/mol]	CO_2	SO_2	NO_2	H_2S
CuBDC +X	26	38	18	39
CuBDC+H_2O +X	23	46	20	33

2.5 Chemical Stability and Degradation Pathway of Nanosheets under Exposure to Humid Acid Gas

Based on the analysis above, when using Cu-BDC nanosheet in the application for flue gas purification, H_2O, H_2SO_3, and H_2SO_4 would be mostly adsorbed on OMSs. An ideal separation candidate adsorbent should be chemically stable after adsorbing water and these acid hydrates. Here, we take H_2SO_3 attack as an example to examine the chemical stability of Cu-BDC nanosheet and illustrate a potential degradation pathway.

A proposed four-step degradation mechanism for H_2SO_3 attacking Cu-BDC nanosheet is shown in Figure 2.7, including (1) binding; (2) protonation; (3) displacement; (4) second metal atom coordination. In the first step, H_2SO_3 were adsorbed on the OMS through acid-base interaction between Cu metal ion and oxygen in H_2SO_3 and hydrogen bonds between –OH group in H_2SO_3 and oxygen in BDC ligand. In the

second step, H_2SO_3 donated a proton to the oxygen in BDC ligand, and the original metal-ligand bond was broken. In the third step, the BDC ligand twisted and the remaining HSO_3^- group coordinated to the open Cu metal ion. In the last step, the BDC ligand further moved away and additional water coordinated to another open Cu metal ion through its oxygen atom, causing the cleavage of two metal-ligand bonds in Cu-BDC nanosheet.

We calculated the formation energies associated with each step along the proposed degradation pathway to analyze how likely the degradation reaction would happen from a thermodynamic viewpoint, also presented in Figure 2.7. The adsorption energy of H_2SO_3 on Cu-BDC nanosheet was -75 kJ/mol, which represented a very exothermic process. In following step 2 and step 3, the free energy of each reaction kept decreased, and up to step 3, H_2SO_3 displacement reaction is an endothermic process with energy penalty of 42 kJ/mol. The total energy for the proposed degradation reaction was increased to -63 kJ/mol, indicating an overall exothermic process. Therefore, from the thermodynamic evaluation of proposed degradation reaction, Cu-BDC nanosheet is very likely to experience chemical structural change upon humid acid hydrate exposure.

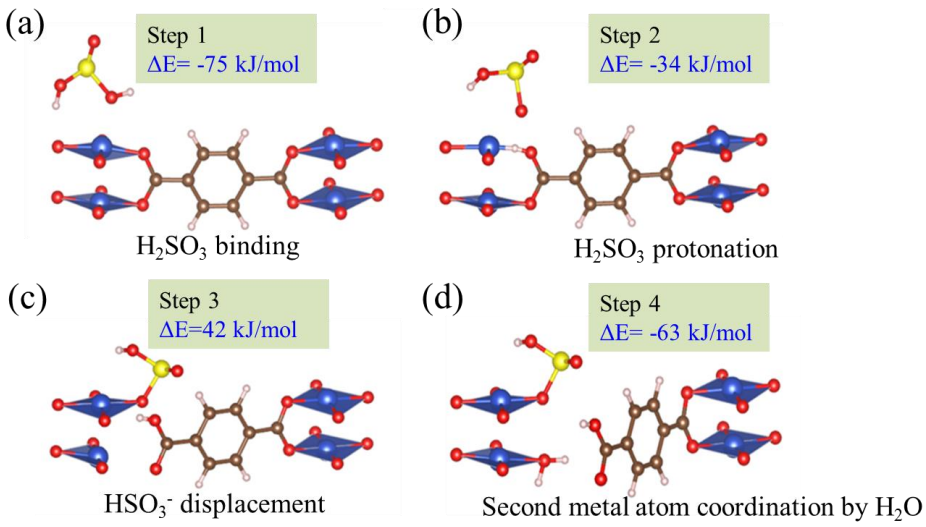

Figure 2.7 Proposed four-step degradation mechanism for Cu-BDC nanosheet upon H_2SO_3 attack.

2.6 Summary

In this chapter, we have created a sheet model to represent M-BDC nanosheets (M = Zn, Cu, and Co), one of MOFs with large external surface adsorption sites. Then, the interactions between a set of small molecules (CO, CO_2, H_2O, SO_2, NO_2, and H_2S) and surface adsorption sites have been evaluated by employing DFT methods with vdW-DF2 functional. From the analysis of calculated adsorption energies, adsorption enthalpies, as well as IR frequency shifts for the normal modes of these small molecules, we have found Zn-BDC and Co-BDC are able to coordinate most strongly with adsorbates, while Cu-BDC tends toward a weaker interaction. In addition, among all the adsorbates we have examined, SO_2, H_2O, and H_2S showed strongest interactions to OMSs of these nanosheets. In addition, through a comparison with bulk MOF-2 structure geometries and study of loading and co-adsorption effects, we have supported the use of a single-layer model as sufficient for studying adsorption of small molecules on exposed OMSs on

nanosheets, and we have also demonstrated that focusing on a single molecule adsorbed at a primary binding site can be a reasonable model for understanding the interactions between small molecules and OMS on these surfaces.

Furthermore, we studied the adsorption of a set of acid gases to the surface adsorption sites of Cu-BDC nanosheet in the presence of water, including competitive co-adsorption motif and cooperative co-adsorption motif. Our computational results suggested that preadsorbed acid gases (CO_2, SO_2, NO_2, and H_2S) on Cu-BDC nanosheet would be replaced by water in the presence of water, leading to acid gas adsorbed on water coordinated OMSs instead of pure OMSs. For CO_2 and H_2S, the binding energies on water coordinated OMSs are lower than vacant OMSs, while for SO_2 and NO_2, the binding energies on water coordinated OMSs are higher. Therefore, even though water has a high probability to compete with acid gas for the same adsorption site, and even replace preadsorbed acid gases, in SO_2 and NO_2 cases, pre-adsorbing a small amount of water can increase the SO_2 and NO_2 binding strength and attack on Cu-BDC nanosheet.

Finally, we have proposed and examined the energetics of potential degradation pathway of Cu-BDC nanosheet exposed to humid acid hydrate, such as H_2SO_3. From a thermodynamic viewpoint, Cu-BDC nanosheet would experience chemical structural change upon humid acid hydrate exposure. These calculations provided valuable insight into the degradation mechanism of MOFs.

2.7 References

1. Long, J. R.; Yaghi, O. M., The pervasive chemistry of metal-organic frameworks. *Chemical Society reviews* **2009,** *38* (5), 1213-4.

2. O'Keeffe, M., Design of MOFs and intellectual content in reticular chemistry: a personal view. *Chemical Society reviews* **2009,** *38* (5), 1215-7.

3. Sholl, D. S.; Lively, R. P., Defects in Metal-Organic Frameworks: Challenge or Opportunity? *J Phys Chem Lett* **2015**, 3437-3444.

4. Chizallet, C.; Lazare, S.; Bazer-Bachi, D.; Bonnier, F.; Lecocq, V.; Soyer, E.; Quoineaud, A.-A.; Bats, N., Catalysis of Transesterification by a Nonfunctionalized Metal-Organic Framework: Acido-Basicity at the External Surface of ZIF-8 Probed by FTIR and ab Initio Calculations. *Journal of the American Chemical Society* **2010,** *132* (35), 12365-12377.

5. Chizallet, C.; Bats, N., External Surface of Zeolite Imidazolate Frameworks Viewed Ab Initio: Multifunctionality at the Organic-Inorganic Interface. *Journal of Physical Chemistry Letters* **2010,** *1* (1), 349-353.

6. Amirjalayer, S.; Tafipolsky, M.; Schmid, R., Surface Termination of the Metal-Organic Framework HKUST-1: A Theoretical Investigation. *Journal of Physical Chemistry Letters* **2014,** *5* (18), 3206-3210.

7. Li, H.; Eddaoudi, M.; Groy, T. L.; Yaghi, O. M., Establishing microporosity in open metal-organic frameworks: Gas sorption isotherms for Zn(BDC) (BDC = 1,4-benzenedicarboxylate). *Journal of the American Chemical Society* **1998,** *120* (33), 8571-8572.

8. Rodenas, T.; Luz, I.; Prieto, G.; Seoane, B.; Miro, H.; Corma, A.; Kapteijn, F.; Llabres i Xamena, F. X.; Gascon, J., Metal-organic framework nanosheets in polymer composite materials for gas separation. *Nature materials* **2015,** *14* (1), 48-55.

9. Yu, K.; Kiesling, K.; Schmidt, J. R., Trace Flue Gas Contaminants Poison Coordinatively Unsaturated Metal–Organic Frameworks: Implications for CO_2 Adsorption and Separation. *The Journal of Physical Chemistry C* **2012,** *116* (38), 20480-20488.

10. Yu, J.; Balbuena, P. B., Water Effects on Postcombustion CO_2 Capture in Mg-MOF-74. *The Journal of Physical Chemistry C* **2013,** *117* (7), 3383-3388.

11. Yazaydın, A. Ö.; Benin, A. I.; Faheem, S. A.; Jakubczak, P.; Low, J. J.; Willis, R. R.; Snurr, R. Q., Enhanced CO2 Adsorption in Metal-Organic Frameworks via Occupation of Open-Metal Sites by Coordinated Water Molecules. *Chemistry of Materials* **2009,** *21* (8), 1425-1430.

12. Tan, K.; Zuluaga, S.; Gong, Q.; Gao, Y.; Nijem, N.; Li, J.; Thonhauser, T.; Chabal, Y. J., Competitive Coadsorption of CO_2 with H_2O, NH_3, SO_2, NO, NO_2, N_2, O_2, and CH_4 in M-MOF-74 (M = Mg, Co, Ni): The Role of Hydrogen Bonding. *Chemistry of Materials* **2015,** *27* (6), 2203-2217.

13. Yu, J.; Balbuena, P. B., How Impurities Affect CO_2 Capture in Metal–Organic Frameworks Modified with Different Functional Groups. *ACS Sustainable Chemistry & Engineering* **2015,** *3* (1), 117-124.

14. Kresse, G.; Joubert, D., From ultrasoft pseudopotentials to the projector augmented-wave method. *Physical Review B* **1999,** *59* (3), 1758-1775.

15. Blochl, P. E., PROJECTOR AUGMENTED-WAVE METHOD. *Physical Review B* **1994,** *50* (24), 17953-17979.

16. Lee, K.; Murray, E. D.; Kong, L.; Lundqvist, B. I.; Langreth, D. C., Higher-accuracy van der Waals density functional. *Physical Review B* **2010,** *82* (8).

17. Perdew, J. P.; Burke, K.; Ernzerhof, M., Generalized gradient approximation made simple. *Physical Review Letters* **1996,** *77* (18), 3865-3868.

18. Dudarev, S. L.; Botton, G. A.; Savrasov, S. Y.; Humphreys, C. J.; Sutton, A. P., Electron-energy-loss spectra and the structural stability of nickel oxide: An LSDA+U study. *Physical Review B* **1998,** *57* (3), 1505-1509.

19. Wang, L.; Maxisch, T.; Ceder, G., Oxidation energies of transition metal oxides within the GGA+U framework. *Physical Review B* **2006,** *73* (19).

20. Henkelman, G.; Jonsson, H., Improved tangent estimate in the nudged elastic band method for finding minimum energy paths and saddle points. *Journal of Chemical Physics* **2000,** *113* (22), 9978-9985.

21. Henkelman, G.; Uberuaga, B. P.; Jonsson, H., A climbing image nudged elastic band method for finding saddle points and minimum energy paths. *Journal of Chemical Physics* **2000,** *113* (22), 9901-9904.

22. Watanabe, T.; Sholl, D. S., Molecular chemisorption on open metal sites in Cu_3(benzenetricarboxylate)$_2$: A spatially periodic density functional theory study. *The Journal of chemical physics* **2010,** *133* (9), 094509.

23. Lee, K.; Howe, J. D.; Lin, L.-C.; Smit, B.; Neaton, J. B., Small-Molecule Adsorption in Open-Site Metal–Organic Frameworks: A Systematic Density Functional Theory Study for Rational Design. *Chemistry of Materials* **2015,** *27* (3), 668-678.

24. Bloch, E. D.; Hudson, M. R.; Mason, J. A.; Chavan, S.; Crocella, V.; Howe, J. D.; Lee, K.; Dzubak, A. L.; Queen, W. L.; Zadrozny, J. M.; Geier, S. J.; Lin, L. C.; Gagliardi, L.; Smit, B.; Neaton, J. B.; Bordiga, S.; Brown, C. M.; Long, J. R., Reversible CO binding enables tunable CO/H_2 and CO/N_2 separations in metal-organic frameworks with exposed divalent metal cations. *Journal of the American Chemical Society* **2014,** *136* (30), 10752-61.

25. Pilusa, T. J.; Huberts, R.; Muzenda, E., Emissions analysis from combustion of eco-fuel briquettes for domestic applications. *Journal of Energy in Southern Africa* **2013,** *24* (4), 30-36.

CHAPTER 3. FORMATION AND STABILITY OF DEFECTIVE UIO-66 WITH MISSING LINKERS AND MISSING CLUSTERS

3.1 Introduction[*]

The porous material UiO-66 is one of the most stable MOFs, largely due to its high metal-ligand coordination. The fundamental building unit of UiO-66 is a six-center octahedral metal cluster in which six Zr sit in an octahedral arrangement. Thesemetal centers are connected by BDC linkers, forming a face-centered-cubic arrangement framework. In this topology, each metal cluster is connected to 12 neighboring clusters by BDC linkers, shown in Figure 3.1. Recently, it has become evident that defect-engineering can be a powerful strategy to adjust the properties of pristine MOF system. Those defects include point defects, dislocations, and grain boundaries. In UiO-66, the most common defect is a missing-linker type of point defect. The existence of missing-linker defects in UiO-66 was first discovered by TGA measurements. Valenzano et al. demonstrated approximately one in twelve of the BDC linkers bound to each metal cluster node was missing.[1] Recently it has been shown that the concentration of missing-linker defects in UiO-66 can be systematically tuned by adding modulators during the material synthesis process, such as benzoic acid (HBC), acetic acid (C_2H_5COOH), formic acid (CH_3COOH), hydrochloric acid (HCl), and trifluoroacetic acid (TFA).[2-3] As modulators, they not only terminate the framework at the crystal boundaries, but also participate in the framework formation as a partial substitute for H_2BDC incorporating on

[*] Results from this chapter have been published previously in Jiao, Y.; Liu, Y.; Zhu, G. H.; Hungerford, J. T.; Bhattacharyya, S.; Lively, R. P.; Sholl, D. S.; Walton, K. S., Heat-Treatment of Defective UiO-66 from Modulated Synthesis: Adsorption and Stability Studies. *Journal of Physical Chemistry C* **2017,** *121* (42), 23471-23479.

the metal cluster.[4,5] During UiO-66 material synthesis, excess modulators compete with H_2BDC to coordinate to metal clusters. These coordinated modulators can be removed from metal clusters upon a thermal treatment, creating missing linker vacancy defects.

The presence of missing-linker defects in a MOF can have a dramatic effect on the physical property, gas adsorption capacity, catalytic activity, and material stability. Cliffe et al. demonstrated defects in UiO-66 could be used to tune the thermomechanical properties of MOFs.[2] Several characterization methods had been applied to investigate the relationship between defect concentration/composition and CO_2 uptake abilities over both low and high pressure ranges, as well as hydroscopic properties.[6] Ghosh et al. described two missing-linker UiO-66 models, and argued that the concentration of defects as well as the location of defects had a profound influence on water and CO_2 adsorption.[7] Wu et al. showed that by varying the synthesis conditions, missing-linker defects in UiO-66 can be tuned systematically, leading to dramatically enhanced porosity (i.e., mesopores), which had profound effects on CO_2 adsorption behavior.[4] Li et al. showed the existence of missing-linker defects in UiO-66 had the potential application in roxarsone removal from the water.[3] Vermoortele et al. demonstrated adding TFA in the UiO-66 synthesis resulted in a highly crystalline material with missing linkers, which can enhance the catalytic activity of UiO-66.[5] Shearer et al. demonstrated that linker defects in UiO-66 resulted in a significantly lower thermal stability than pristine UiO-66.[8]

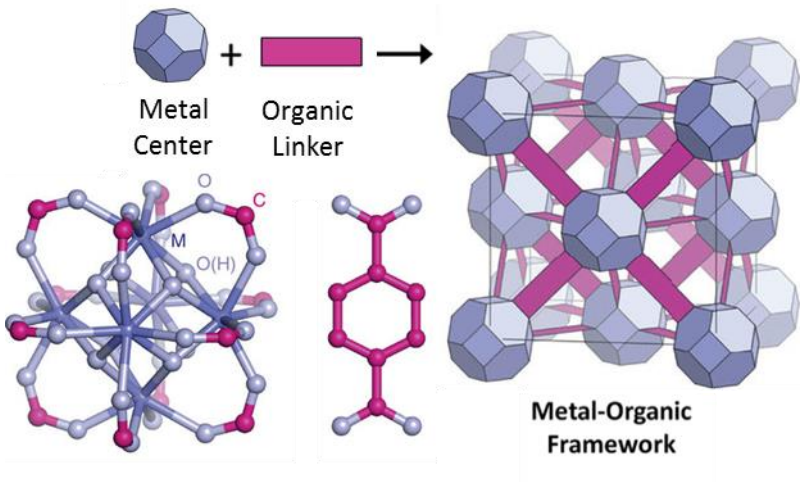

Figure 3.1 Fundamental building block and unit cell of UiO-66. Reproduced from ref 9.[9]

Multiple groups have studied the structure of UiO-66 with linker vacancies. Trickett et al. identified the missing-linker defect sites in UiO-66 on the molecular scale with single-crystal X-ray diffraction (SXRD), showing the defective sites were occupied by water, with charge neutrality maintained by hydroxide anions hydrogen bonding to the metal cluster.[10] Ling et al. demonstrated that charge balancing hydroxide anions were bonded to under-coordinated Zr sites around the linker vacancies using static and dynamic first principles approaches. They further showed that the defective UiO-66 structures exhibited strong dynamic behavior with rapid proton transfer involving the hydroxide anion and physisorbed atmospheric water molecules.[11]

Recent studies revealed that the defective sites created in UiO series materials with additional modulators contain not only linker vacancies, but also metal oxide cluster vacancies. Gutov et al. showed that using a high concentration of acetic and formic acid as modulators to synthesize missing-linker defect UiO-67 can also produce missing metal cluster node defects.[12] Hu et al. synthesized two hierarchically porous MOFs named

NUS-6 composed of either zirconium (Zr) or hafnium (Hf) clusters, and they found hierarchical porosity of NUS-6 was a result of both missing linkers and clusters, which made NUS-6 an efficient and selective solid acid catalyst.[13] Cliffe et al. created an atomically detailed model representing a nanoregion defect in UiO-66 where metal oxide cluster vacancies occurred at the corners of the cubic unit cell based on a combination of diffuse scattering, electron microscopy, anomalous X-ray scattering and pair distribution function measurements.[9]

Most previous studies have focused on tuning the adsorption properties of defective UiO-66 towards small adsorbates such as CO_2. Studies evaluating adsorption performance of large molecules and elucidating the influence of defect on material chemical stability, however, are relatively sparse. When using these porous materials under realistic conditions, where the presence of multiple contaminants such as CO_2, H_2O, SO_X, NO_X, and H_2S is common, the chemical stability of adsorbent is an important issue that needs to be addressed. In this work, the effect of defects inside UiO-66 on guest molecule interaction is evaluated using physisorption with molecules of different sizes, including N_2, SO_2, benzene, and cyclohexane, through Grand Canonical Monte Carlo (GCMC) calculations. In addition to adsorption properties, the chemical stability with respect to attack by water of a series of UiO-66 with different types of compensating groups for missing-linker defects are investigated through electronic structure calculations.

3.2 Methods and Computational Details

3.2.1 Density Functional Theory (DFT) Calculations

All UiO-66 related framework structures were optimized by Density Functional Theory calculations with periodic models performed in the Vienna Ab initio Simulation Package (VASP) with a planewave basis set and core electrons represented with projector augmented wave (PAW) potentials.[14,15] For all DFT calculations, the Perdew−Burke−Ernzerhof (PBE) functional and semiempirical dispersion corrections via the DFT-D3 method were used to better capture van der Waals dispersion interactions.[16, 17] We used a planewave basis set with a cutoff energy of 600 eV, with total energy and atomic force convergence criteria for energy relaxation of 10^{-6} eV and 0.03 eV/Å. In the climbing Nudged Elastic Band (NEB) calculations, the convergence criteria is that atomic forces were less than 0.07 eV/ Å.[18-19] We first optimized the atomic positions and lattice constants of the pristine UiO-66 structure using a 2×1×1 primitive cell. Based on the optimized pristine UiO-66 structure, one of the original BDC ligands was substituted by either two TFA ligands or two water molecules with two hydroxyl groups incorporating to Zr_6 clusters, both of which were further optimized in calculations where the lattice constants were fixed. Water insertion to metal-ligand bond reaction and water displacement of the protonated ligand reaction occurred on both three optimized framework structures. Formation energies of water physisorption, insertion, and displacement along proposed reaction pathways were calculated as energy difference between reaction products and reactants. The reactants for all three reactions are bare MOF structures and isolated water molecules. Positive and negative reaction formation energy correspond to an energetically unfavorable process and an energetically favorable process, respectively.

3.2.2 Molecular Mechanics Calculations

In this study, a missing cluster type of defective UiO-66 is considered by using **reo-**defective UiO-66 crystal model, in which one out of four Zr_6 clusters is missing within every unit cell and trifluoroacetate ligands are utilized to compensate Zr_6 clusters, as shown in Figure 3.2.[9] Such missing cluster defects cause the metal-ligand connectivity decreased to 8 from 12 in pristine UiO-66.[20] Adsorption isotherms of probe molecules, including N_2, SO_2, benzene, and cyclohexane, on pristine UiO-66 and **reo**-defective UiO-66 were computed using GCMC simulations in RASPA.[21, 22] Lennard-Jones (LJ) and Coulombic potentials were combined to describe the guest molecule - guest molecule and guest molecule - MOF interactions with Lorentz-Berthelot (LB) mixing rules. LJ parameters of frameworks are from DREIDING force field except for Zr, for which was taken from UFF force field.[23, 24] The framework structures were treated as rigid during GCMC simulations. LJ parameters of N_2 were from DREIDING force field and N_2 was modeled as a three-site model with two sites located at two N atoms and the third one located at its center of mass.[25] LJ parameters of SO_2 were taken from UFF force field. SO_2 was modeled as a three-site model with charges on each site. Benzene was described using TraPPE-EH model, with interaction sites located at the atomic center for both C and H atoms.[26] Cyclohexane was modeled as a TraPPE-UA model, treating each $–CH_2$ group as a united-site. The model assumed fixed bond lengths with harmonic bending modes.[27] The atomic partial charges for frameworks and adsorbates are obtained from previous work.[28, 29] In GCMC simulation, 50000 initial cycles were applied for the system to reach equilibrium, and another 100000 cycles were applied to calculate the average adsorption properties. Four types of guest molecule moves were included during each cycle simulation: translation, rotation, reinsertion, and swap.

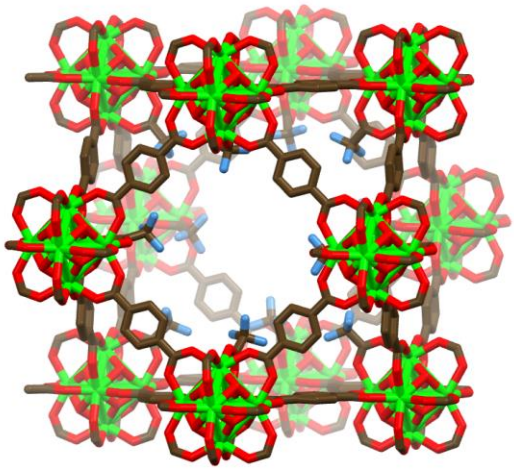

Figure 3.2 Reo-defective UiO-66 structure with trifluoroacetate ligands compensating Zr_6 clusters. Zr atoms are shown in green, O atoms are shown in red, C atoms are shown in gray, H atoms are shown in white, F atoms are shown in blue.

3.3 Defect Influence in Molecular Adsorption

To explore the role of defects in molecular adsorption behavior in defective UiO-66, both pristine UiO-66 material and defective UiO-66 material were synthesized experimentally by Dr. Yang Jiao. The pristine UiO-66 material has a Brunauer-Emmett-Teller (BET) surface area of 1179 m^2/g. The defective UiO-66 material was initially synthesized from the mixing of 0.682 mmol $ZrCl_4$, 0.682 mmol H_2BDC, and 13.64 mmol TFA in 26.5 mL DMF at room temperature. Then the as-synthesized defective UiO-66 sample was heated at 200°C with the removal of the physically trapped TFA and solvents molecules to form defective UiO-66 material. The defective UiO-66 material has a BET surface area of 1808 m^2/g. Computational modeling was also performed to understand the influence of defects on pore size and adsorption performance. To represent experimentally synthesized pristine UiO-66 material and defective UiO-66 material, two UiO-66 based structure models were build, including a pristine UiO-66 model and a **reo-**

defective UiO-66 model, respectively. The theoretically simulated surface area of the pristine UiO-66 model is 951 m^2/g and that of the **reo**-defective UiO-66 is 1822 m^2/g. Good agreement between the theoretically simulated surface area and the experimentally measured BET surface area of these two materials supported the validity of using these two crystal models to represent experimentally synthesized pristine UiO-66 material and defective UiO-66 material. In addition, The simulated and experimentally measured N_2 isotherms on these two UiO-66 materials are shown in Figure 3.3. As suggested by the comparison of BET surface areas, the simulated and experimental isotherms are similar, supporting the idea of using these computational models to describe the experimental materials.[30]

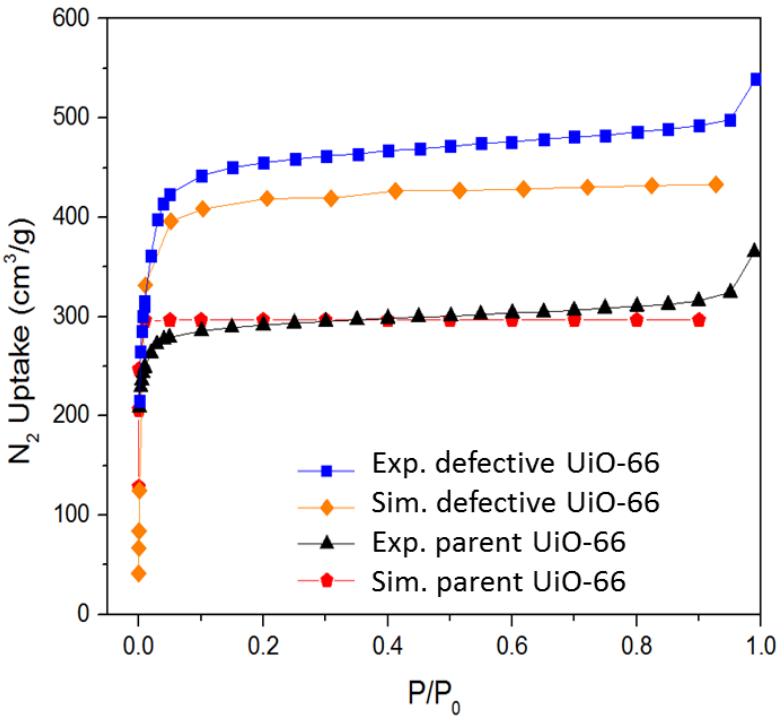

Figure 3.3 Experimental and computational N_2 adsorption isotherms at 77 K for pristine UiO-66 and defective UiO-66.

Given that the pore diameter in pristine UiO-66 is ~6 Å, and that in **reo-**defective UiO-66 is increased to ~9 Å, we selected SO_2 (4.1 Å), benzene (C_6H_6, 5.8 Å), and cyclohexane (c-C_6H_{12}, 6.2 Å) as the probe molecules, whose diameters are listed after the name of molecules, to determine the impact of defects on the porosity within **reo-**defective UiO-66. Atomic structures of the probe molecules are shown in Figure 3.4. We simulated above probe molecule adsorption isotherms at room temperature on both pristine and **reo-**defective UiO-66 models through GCMC simulations. In Figure 3.4, we specified probe molecule adsorption capacities at 0.2 relative pressure ($P/P_0 = 0.2$), and compared the simulated adsorption capacities (in light pink and blue colors) to experiment data (in dark pink and blue colors) for both pristine (in pink color) and defective (in blue color) UiO-66. All experimental data were measured by Dr. Yang Jiao. In general, there is good agreement between simulated and experimental measured adsorption capacity and the adsorption uptake for all three probe molecules in defective framework are higher than that in pristine framework.

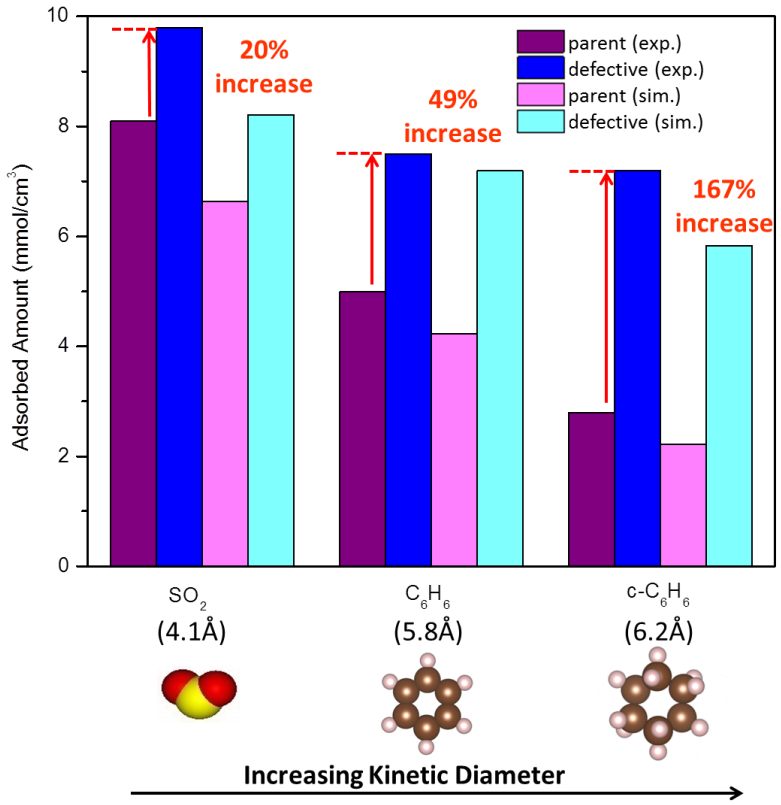

Figure 3.4 Simulated and experimental measured adsorption capacities (at $P/P_0 = 0.2$ and $T = 25$ ° C) of SO_2, benzene (C_6H_6), and cyclohexane (c-C_6H_{12}) for both pristine and reo-defective UiO-66.

When using SO_2 as the probe molecule, we observed that SO_2 could be adsorbed in both the pristine and **reo**-defective UiO-66. In comparison with the adsorption uptake in the pristine framework, there is only a small increase (20%) in the defective framework. This small increment is primarily attributed to the difference in accessible surface areas between two frameworks, and the incremental change in adsorption is consistent with the change in BET surface areas between the two frameworks. When using benzene and cyclohexane as the probe molecules, the size of which are close to or even larger than pristine UiO-66 pore size, we observed that the **reo**-defective UiO-66

displays a 49% and 167% increase for benzene and cyclohexane, respectively, due to the enlarged pore size generated by missing cluster defects. Based on the adsorption capability results for these three probe molecules, it is clear that missing cluster defects can increase the pore size in **reo**-defective UiO-66 and thus significantly enhance the adsorption capacity of large molecules that cannot be effectively captured by pristine UiO-66.

3.4 Defect Influence in Chemical Stability

In addition to adsorption properties of defective UiO-66, understanding the chemical stability of defect-engineered MOFs is also interesting. Three types of UiO-66 related frameworks, including pristine UiO-66 structure, a TFA group capped defective UiO-66 structure, and a hydrolyzed defective UiO-66 structure were used to explore the chemical stability and analyze the degradation reaction energetics. These structures are shown in Figure 3.5. The pristine UiO-66 structure is a 2×1×1 unit cell of the UiO-66 primitive unit cell taken from the CoRE MOF database.[31] The TFA group capped defective UiO-66 structure is a derivative unit cell of pristine UiO-66 structure with one BDC ligand substituted by two TFA groups, denoted as TFA-UiO-66. The hydrolyzed missing-linker type of defective UiO-66 structure is also a derivative unit cell of pristine UiO-66 structure with one missing BDC ligand capped by one water and a hydroxyl group, denoted as ML-UiO-66.

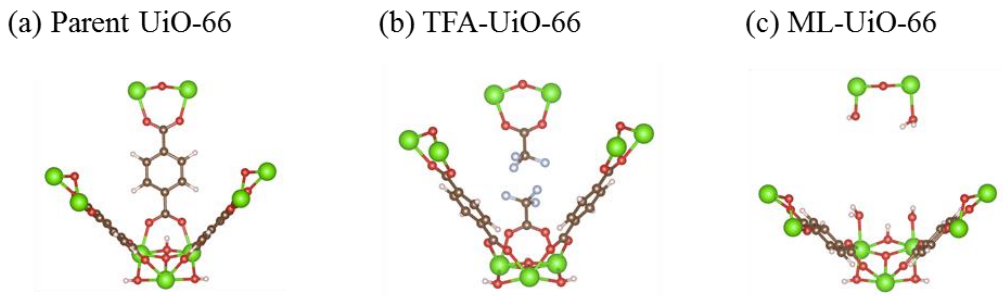

Figure 3.5 Atomic representations of (a) pristine UiO-66, (b) TFA-UiO-66, and (c) ML-UiO-66. Only the structural components associated with the presence of defect are shown, with the rest of the structure omitted for clarity. Zr atoms are shown in green, O atoms are shown in red, C atoms are shown in gray, H atoms are shown in yellow and F atoms are shown in blue.

When using these materials in acidic environments, their performance would potentially be weakened, as a result of undergoing partial or total degradation reactions. Determining degradation mechanisms of MOFs upon exposure to water and humid acid gas is an active area of research, but there are still many outstanding questions. Previous studies provide evidence that MOFs undergo degradation as the reacting molecule attacks the metal-ligand bonds.[32-35, 36] In this work, we proposed a potential degradation pathway for pristine UiO-66, TFA-UiO-66, and ML-UiO-66 upon water attack, shown in Figure 3.6. Figure 3.7 shows a detailed degradation pathway for removing one BDC ligand from the framework that is applicable for all these three UiO-66 related frameworks.

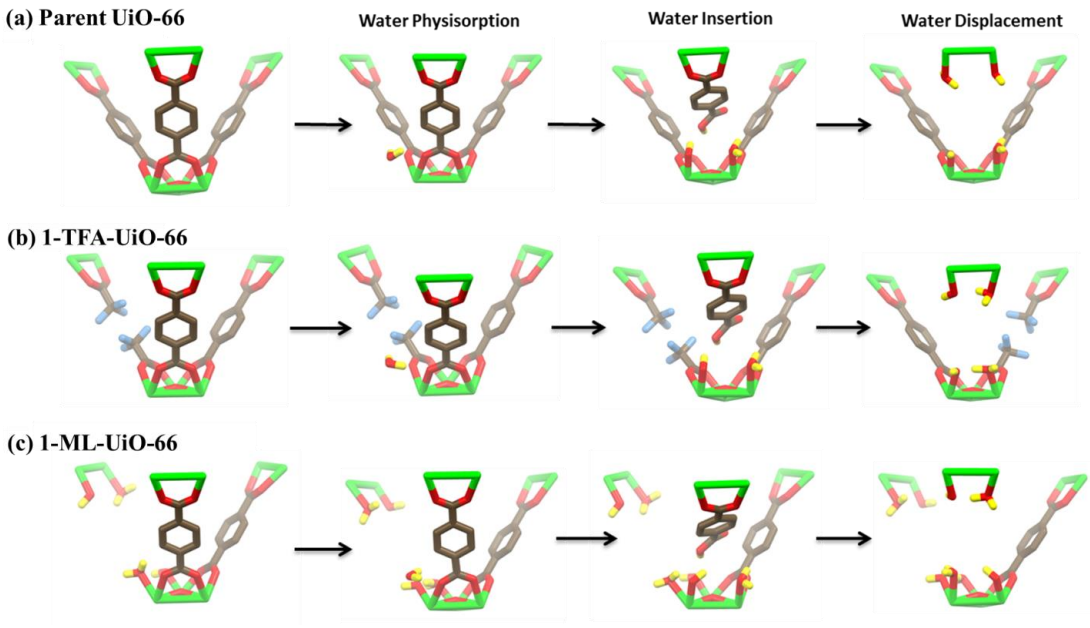

Figure 3.6 Proposed degradation mechanisms for (a) pristine UiO-66, (b) TFA-UiO-66, and (c) ML-UiO-66. Only the structural components associated with the degradation reactions are shown, with the rest of the structure omitted for clarity.

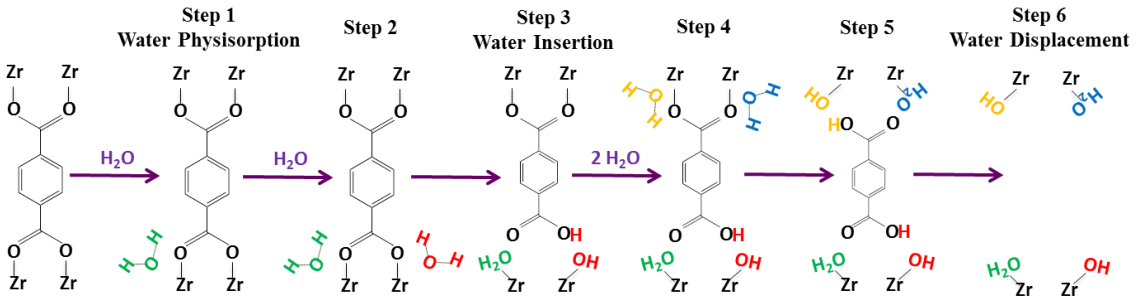

Figure 3.7 Proposed detailed degradation mechanisms for one BDC ligand removal from the framework, involving five steps with the cleavage of four metal-ligand bonds.

When a water molecule adsorbs and dissociates near the Zr metal center, water can donate a proton to the BDC ligand, and the remaining hydroxyl group continues to be coordinated to the Zr metal center to maintain charge neutrality. As a result, multiple water insertion reactions can cause the cleavage of the metal-ligand bond and eventually the removal of neutral, protonated BDC ligand from the framework. First, we evaluated

the chemical stability from a thermodynamic perspective by analyzing the degradation reaction energetics calculated by DFT. Formation energies along these proposed reaction pathways are calculated as the energy difference between reactants and products. The isolated water molecules and bare UiO-66 frameworks serve as the reactants for each product. The calculated formation energies associated with each degradation pathway step are shown in Table 1. (Each step corresponds to the intermediate state in the proposed detailed degradation mechanism in Figure 3.7) Water physisorption on the Zr_6 cluster is energetically favorable in all three frameworks, as shown in the water physisorption step in Table 1. This is expected because water isotherms measured experimentally for the pristine UiO-66 framework exhibit appreciable water uptake at 30% RH, and the missing linker defects make UiO-66 even more hydrophilic.[7] As the reaction moves forward, water insertion to the metal-ligand bond and the removal of the neutral and protonated BDC ligand by water displacement are only thermodynamically favorable in ML-UiO-66 with missing linker defect, with reaction energies of -84 kJ/mol and -39 kJ/mol, respectively, shown in water insertion step and water displacement step in Table 1. This is consistent with an experimental chemical stability evaluation result that missing-linker defective UiO-66 sample experienced chemical degradation upon liquid water exposure.[30] For pristine UiO-66 and defective TFA-UiO-66 with the incorporation of TFA compensating groups, the cleavage of the metal-ligand bond and the removal of neutral and protonated BDC ligand are thermodynamically unfavorable, in agreement with the phenomena observed experimentally that pristine UiO-66 and TFA group capped defective UiO-66 samples retain nearly all of their starting BET surface areas upon water exposure.[30]

Table 3.1 Formation Energies of the Proposed Reaction Pathways (Each step corresponds to the intermediate state in the proposed detailed degradation mechanism in Figure 3.6)

MOF [kJ/mol]	Step 1 Water Physisorption	Step 2	Step 3 Water Insertion	Step 4	Step 5	Step 6 Water Displacement
Pristine UiO-66	-26	-61	20	-50	-25	102
TFA-UiO-66	-35	-66	17	-58	-40	29
ML-UiO-66	-32	-58	-84	-96	-59	-39

The pristine UiO-66 and TFA group capped defective TFA-UiO-66 showed higher thermodynamic stability than missing-linker defective ML-UiO-66. To further understand the kinetic stability of three different frameworks, the activation energies for water insertion reaction on these three frameworks were examined. We chose Step 2 in degradation mechanism as the initial state of this water insertion reaction, and Step 3 as the final state. Figure 3.8 (a) shows the detailed reaction pathway of water insertion reaction. The calculated activation energy for breaking one side of metal-ligand bonds was ~0.79 eV (76 kJ/mol) on missing-linker defective ML-UiO-66, lower than the barrier of 1.22 eV (118 kJ/mol) on pristine UiO-66 and 1.31 eV (126 kJ/mol) on the TFA group capped defective TFA-UiO-66. The energy profiles associated with this water insertion reaction on these three frameworks are shown in Figure 3.8. Since the cleavage of metal-ligand bonds by water attack on missing-linker defective ML-UiO-66 is substantially more both thermodynamically and kinetically favorable as compared to on both pristine UiO-66 and TFA group capped defective TFA-UiO-66, the incorporation of TFA compensating groups can effectively prevent the degradation reaction that occurs on missing-linker defective ML-UiO-66 due to exposure to water.

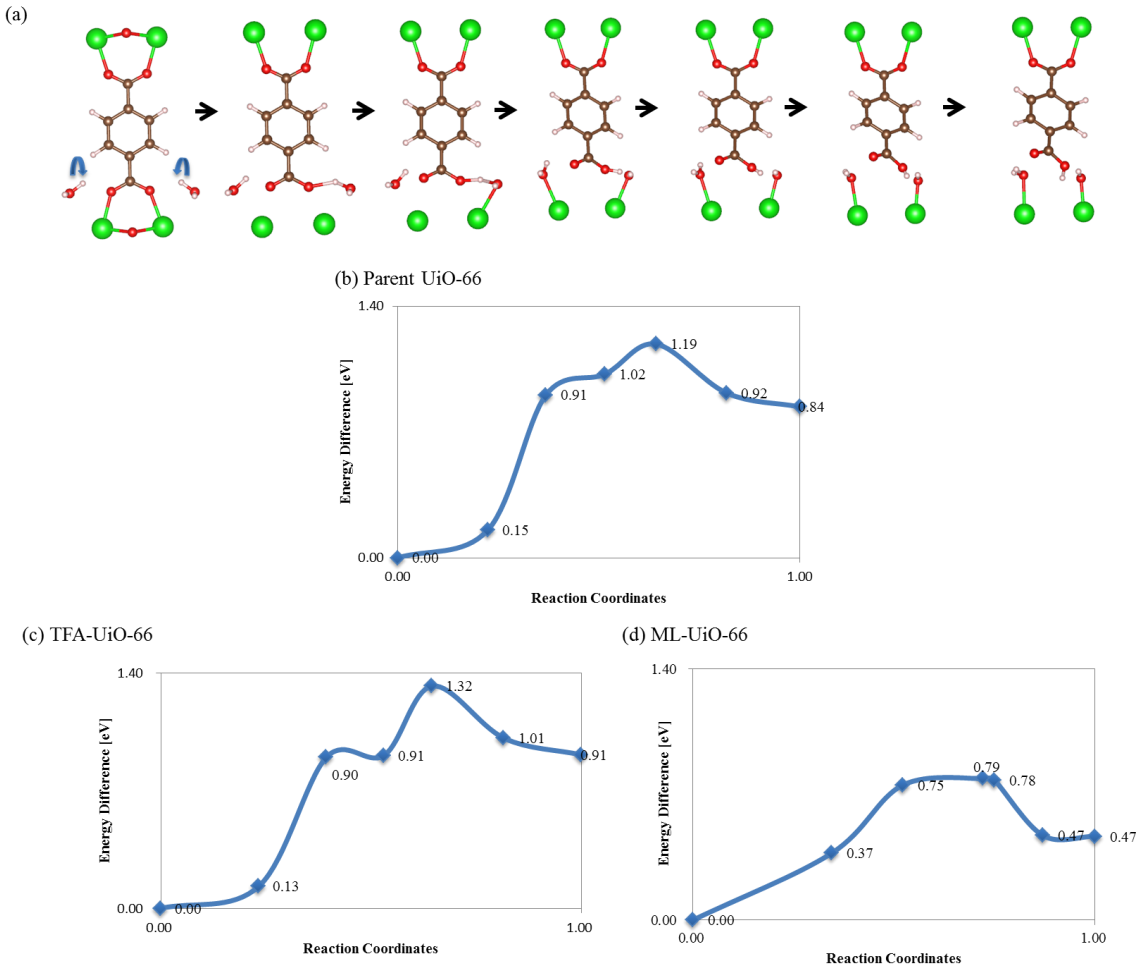

Figure 3.8 (a) Atomic representation of detailed reaction pathway of water insertion reaction. Energy profiles associated with water insertion reaction on (b) pristine UiO-66, (c) TFA-UiO-66, and (d) ML-UiO-66.

3.5 Summary

In this work, to evaluate the influence of defects on large molecule adsorption performance on material and material chemical stability, we built a series of UiO-66 related crystal models with different concentration of defects and different types of compensating groups, including pristine UiO-66, TFA group capped missing-linker defective UiO-66 (TFA-UiO-66), TFA group capped missing-cluster defective UiO-66 (**reo**-defective UiO-66), and hydrolyzed missing-linker defective UiO-66 (ML-UiO-66).

Through analyzing several various probe molecule physisorption isotherms calculated by GCMC method, including N_2, SO_2, benzene, and cyclohexane, **reo-**defective UiO-66 exhibited significantly increment of adsorption uptake in comparison to pristine UiO-66, due to induced missing cluster defects. The adsorption capacities were greatly enhanced for large size molecules, benzene and cyclohexane, which cannot be effectively captured by pristine UiO-66. Finally, we systematically explored the effect of different types of compensating groups for defects on material chemical stability in a water environment. Via both thermodynamic and kinetic evaluation of proposed degradation reaction induced by water attack on pristine UiO-66, TFA group capped defective TFA-UiO-66, and hydrolyzed defective ML-UiO-66, we observed that the incorporation of TFA compensating groups could effectively prevent the degradation reaction that occurs on hydrolyzed defective ML-UiO-66 due to exposure to water. Therefore, this work shows that crystal pore size can be tuned with the introduction of defects and the structural incorporation of TFA groups in defective UiO-66 leads to an increase in average pore size without sacrificing chemical stability toward water attack.

3.6 References

1. Valenzano, L.; Civalleri, B.; Chavan, S.; Bordiga, S.; Nilsen, M. H.; Jakobsen, S.; Lillerud, K. P.; Lamberti, C., Disclosing the Complex Structure of UiO-66 Metal Organic Framework: A Synergic Combination of Experiment and Theory. *Chemistry of Materials* **2011,** *23* (7), 1700-1718.

2. Cliffe, M. J.; Hill, J. A.; Murray, C. A.; Coudert, F.-X.; Goodwin, A. L., Defect-dependent colossal negative thermal expansion in UiO-66(Hf) metal-organic framework. *Physical Chemistry Chemical Physics* **2015,** *17* (17), 11586-11592.

3. Li, B.; Zhu, X.; Hu, K.; Li, Y.; Feng, J.; Shi, J.; Gu, J., Defect creation in metal-organic frameworks for rapid and controllable decontamination of roxarsone from aqueous solution. *Journal of Hazardous Materials* **2016,** *302*, 57-64.

4. Wu, H.; Chua, Y. S.; Krungleviciute, V.; Tyagi, M.; Chen, P.; Yildirim, T.; Zhou, W., Unusual and highly tunable missing-linker defects in zirconium metal-organic framework UiO-66 and their important effects on gas adsorption. *J Am Chem Soc* **2013,** *135* (28), 10525-32.

5. Vermoortele, F.; Bueken, B.; Le Bars, G.; Van de Voorde, B.; Vandichel, M.; Houthoofd, K.; Vimont, A.; Daturi, M.; Waroquier, M.; Van Speybroeck, V.; Kirschhock, C.; De Vos, D. E., Synthesis Modulation as a Tool To Increase the Catalytic Activity of Metal-Organic Frameworks: The Unique Case of UiO-66(Zr). *Journal of the American Chemical Society* **2013,** *135* (31), 11465-11468.

6. Liang, W. B.; Coghlan, C. J.; Ragon, F.; Rubio-Martinez, M.; D'Alessandro, D. M.; Babarao, R., Defect engineering of UiO-66 for CO_2 and H_2O uptake - a combined experimental and simulation study. *Dalton Transactions* **2016,** *45* (11), 4496-4500.

7. Ghosh, P.; Colon, Y. J.; Snurr, R. Q., Water adsorption in UiO-66: the importance of defects. *Chem. Commun.* **2014,** *50* (77), 11329-11331.

8. Shearer, G. C.; Chavan, S.; Ethiraj, J.; Vitillo, J. G.; Svelle, S.; Olsbye, U.; Lamberti, C.; Bordiga, S.; Lillerud, K. P., Tuned to Perfection: Ironing Out the Defects in Metal–Organic Framework UiO-66. *Chemistry of Materials* **2014,** *26* (14), 4068-4071.

9. Cliffe, M. J.; Wan, W.; Zou, X.; Chater, P. A.; Kleppe, A. K.; Tucker, M. G.; Wilhelm, H.; Funnell, N. P.; Coudert, F.-X.; Goodwin, A. L., Correlated defect nanoregions in a metal-organic framework. *Nature communications* **2014,** *5*.

10. Trickett, C. A.; Gagnon, K. J.; Lee, S.; Gandara, F.; Burgi, H. B.; Yaghi, O. M., Definitive molecular level characterization of defects in UiO-66 crystals. *Angewandte Chemie* **2015,** *54* (38), 11162-7.

11. Peralta, D.; Barthelet, K.; Pérez-Pellitero, J.; Chizallet, C.; Chaplais, G.; Simon-Masseron, A.; Pirngruber, G. D., Adsorption and Separation of Xylene Isomers: CPO-27-Ni vs HKUST-1 vs NaY. *The Journal of Physical Chemistry C* **2012,** *116* (41), 21844-21855.

12. Gutov, O. V.; Hevia, M. G.; Escudero-Adan, E. C.; Shafir, A., Metal-Organic Framework (MOF) Defects under Control: Insights into the Missing Linker Sites and Their Implication in the Reactivity of Zirconium-Based Frameworks. *Inorganic Chemistry* **2015,** *54* (17), 8396-8400.

13. Hu, Z.; Peng, Y.; Gao, Y.; Qian, Y.; Ying, S.; Yuan, D.; Horike, S.; Ogiwara, N.; Babarao, R.; Wang, Y.; Yan, N.; Zhao, D., Direct Synthesis of Hierarchically Porous Metal–Organic Frameworks with High Stability and Strong Brønsted Acidity: The Decisive Role of Hafnium in Efficient and Selective Fructose Dehydration. *Chemistry of Materials* **2016,** *28* (8), 2659-2667.

14. Kresse, G.; Joubert, D., From ultrasoft pseudopotentials to the projector augmented-wave method. *Phys. Rev. B: Condens. Matter* **1999,** *59* (3), 1758-1775.

15. Blochl, P. E., Projector augmented-wave method. *Phys. Rev. B: Condens. Matter* **1994,** *50* (24), 17953-17979.

16. Lee, K.; Murray, E. D.; Kong, L. Z.; Lundqvist, B. I.; Langreth, D. C., Higher-accuracy van der Waals density functional. *Phys. Rev. B: Condens. Matter* **2010,** *82* (8), 081101.

17. Grimme, S.; Antony, J.; Ehrlich, S.; Krieg, H., A consistent and accurate ab initio parametrization of density functional dispersion correction (DFT-D) for the 94 elements H-Pu. *J. Chem. Phys.* **2010,** *132* (15), 154104.

18. Henkelman, G.; Jonsson, H., Improved tangent estimate in the nudged elastic band method for finding minimum energy paths and saddle points. *Journal of Chemical Physics* **2000,** *113* (22), 9978-9985.

19. Henkelman, G.; Uberuaga, B. P.; Jonsson, H., A climbing image nudged elastic band method for finding saddle points and minimum energy paths. *Journal of Chemical Physics* **2000,** *113* (22), 9901-9904.

20. Cliffe, M. J.; Wan, W.; Zou, X. D.; Chater, P. A.; Kleppe, A. K.; Tucker, M. G.; Wilhelm, H.; Funnell, N. P.; Coudert, F. X.; Goodwin, A. L., Correlated defect nanoregions in a metal-organic framework. *Nat. Commun.* **2014,** *5*, 4176.

21. Gelb, L. D.; Gubbins, K. E., Pore size distributions in porous glasses: A computer simulation study. *Langmuir : the ACS journal of surfaces and colloids* **1999,** *15* (2), 305-308.

22. Dubbeldam, D.; Calero, S.; Ellis, D. E.; Snurr, R. Q., RASPA: molecular simulation software for adsorption and diffusion in flexible nanoporous materials. *Mol. Simul.* **2016,** *42* (2), 81-101.

23. Mayo, S. L.; Olafson, B. D.; Goddard, W. A., DREIDING: A generic force-field for molecular simulations. *J. Phys. Chem.* **1990,** *94* (26), 8897-8909.

24. Rappe, A. K.; Casewit, C. J.; Colwell, K. S.; Goddard, W. A.; Skiff, W. M., UFF, a full periodic table force field for molecular mechanics and molecular dynamics simulations. *J. Am. Chem. Soc.* **1992,** *114* (25), 10024-10035.

25. Potoff, J. J.; Siepmann, J. I., Vapor-liquid equilibria of mixtures containing alkanes, carbon dioxide, and nitrogen. *Aiche Journal* **2001,** *47* (7), 1676-1682.

26. Rai, N.; Siepmann, J. I., Transferable Potentials for Phase Equilibria. 9. Explicit Hydrogen Description of Benzene and Five-Membered and Six-Membered Heterocyclic Aromatic Compounds. *J. Phys. Chem. B* **2007,** *111* (36), 10790-10799.

27. Keasler, S. J.; Charan, S. M.; Wick, C. D.; Economou, I. G.; Siepmann, J. I., Transferable Potentials for Phase Equilibria-United Atom Description of Five- and Six-Membered Cyclic Alkanes and Ethers. *J. Phys. Chem. B* **2012,** *116* (36), 11234-11246.

28. Sokolic, F.; Guissani, Y.; Guillot, B., Molecular Dynamics Simulations of Thermodynamic and Structural Properties of Liquid SO_2. *Molecular Physics* **1985,** *56* (2), 239-253.

29. Yang, Q. Y.; Wiersum, A. D.; Llewellyn, P. L.; Guillerm, V.; Serred, C.; Maurin, G., Functionalizing porous zirconium terephthalate UiO-66(Zr) for natural gas upgrading: a computational exploration. *Chemical communications* **2011,** *47* (34), 9603-9605.

30. Jiao, Y.; Liu, Y.; Zhu, G. H.; Hungerford, J. T.; Bhattacharyya, S.; Lively, R. P.; Sholl, D. S.; Walton, K. S., Heat-Treatment of Defective UiO-66 from Modulated Synthesis: Adsorption and Stability Studies. *Journal of Physical Chemistry C* **2017,** *121* (42), 23471-23479.

31. Chung, Y. G.; Camp, J.; Haranczyk, M.; Sikora, B. J.; Bury, W.; Krungleviciute, V.; Yildirim, T.; Farha, O. K.; Sholl, D. S.; Snurr, R. Q., Computation-Ready, Experimental Metal-Organic Frameworks: A Tool To Enable High-Throughput Screening of Nanoporous Crystals. *Chemistry of Materials* **2014,** *26* (21), 6185-6192.

32. Pang, S. H.; Han, C.; Sholl, D. S.; Jones, C. W.; Lively, R. P., Facet-Specific Stability of ZIF-8 in the Presence of Acid Gases Dissolved in Aqueous Solutions. *Chemistry of Materials* **2016,** *28* (19), 6960-6967.

33. Bhattacharyya, S.; Pang, S. H.; Dutzer, M. R.; Lively, R. P.; Walton, K. S.; Sholl, D. S.; Nair, S., Interactions of SO_2-Containing Acid Gases with ZIF-8: Structural Changes and Mechanistic Investigations. *Journal of Physical Chemistry C* **2016,** *120* (48), 27221-27229.

34. Mounfield, W. P.; Han, C.; Pang, S. H.; Tumuluri, U.; Jiao, Y.; Bhattacharyya, S.; Dutzer, M. R.; Nair, S.; Wu, Z.; Lively, R. P.; Sholl, D. S.; Walton, K. S., Synergistic Effects of Water and SO_2 on Degradation of MIL-125 in the Presence of Acid Gases. *Journal of Physical Chemistry C* **2016,** *120* (48), 27230-27240.

35. Burtch, N. C.; Walton, K. S., Modulating Adsorption and Stability Properties in Pillared Metal-Organic Frameworks: A Model System for Understanding Ligand Effects. *Acc. Chem. Res.* **2015,** *48* (11), 2850-2857.

36. Zhang, C. Y.; Han, C.; Sholl, D. S.; Schmidt, J. R., Computational Characterization of Defects in Metal-Organic Frameworks: Spontaneous and Water-Induced Point Defects in ZIF-8. *J. Phys. Chem. Lett.* **2016,** *7* (3), 459-464.

CHAPTER 4. FORMATION MECHANISM, DEFECT ENGINEERING, AND CHEMICAL STABILITY OF IMINE-BASED POROUS ORGANIC CAGE

4.1 Introduction[*]

Porous organic cage (POC) solids are porous materials made up of individual porous molecules held together by non-covalent forces.[1-4] POC solids have shown promising properties and attracted significant attention in applications including separation, adsorption, catalysis, and molecular sensing.[5-11] The discovery of new porous organic cage crystals with desired functionality depends largely on improved understanding of the formation mechanisms of POCs, which have not been thoroughly investigated yet. Compared to conducting time-consuming experiments to find new combinations of linkers, such as diamine molecules and trialdehyde molecules, computational methods can accelerate the design of new POC crystals. Nevertheless, there are two main challenges associated with the prediction of solid POC crystals using computational methods. The first challenge is the assembly of linkers into a cage in solution, and the other is the packing of synthesized cages into solid state upon crystallization and desolvation. The latter has been addressed by crystal structure prediction methods developed by Cooper and coworkers from the University of Liverpool, which forecasts the structure of porous polymorphs based on a known cage.[12-13] However, this method requires a prior knowledge of the single cage structure.

[*] Results from this chapter have been published previously in Zhu, G. H.; Hoffman, C. D.; Liu, Y.; Bhattacharyya, S.; Tumuluri, U.; Jue, M. L.; Wu, Z. L.; Sholl, D. S.; Nair, S.; Jones, C. W.; Lively, R. P., *Chemistry-a European Journal* **2016,** *22* (31), 10743-10747. and in Zhu, G.; Liu, Y.; Flores, L.; Lee, Z. R.; Jones, C. W.; Dixon, D. A.; Sholl, D. S.; Lively, R. P., *Chemistry of Materials* **2018,** *30* (1), 262-272

Therefore, there is a gap in *in silico* prediction of how linkers form the single cage structures, which is addressed in this Chapter. Here, we use two types of imine-based porous organic cages, CC3-R and CC-pentane, to investigate the formation mechanism of POC, the assembly of linkers into a cage. CC3-R is formed via [4+6] cycloimination reaction between triformylbenzene and (1R,2R)-(−)-1,2-diaminocyclohexane.[1] CC-pentane is formed via [2+3] cycloimination reaction between triformylbenzene and 1,5-pentane-diamine.[14]

Recently there has been growing emphasis on defect engineering in the study of MOFs, as the mechanical and chemical properties resulted from defects have the potentials to broaden the utility of these materials.[15-16] However, in the area of POCs, current studies often assume chemical purity of the cage crystal. Little is known about the formation or existence of defects in POCs. Inspired by this, we are interested in introducing defects into CC3-R crystals. Among various kinds of defects that are present in MOFs, a missing-linker-type molecular defect is the most common type of defects, where one of the linkers in MOFs is missing. Thus, mimicking missing linker defects in MOFs, isophthaladehyde (IPA) is introduced into CC3-R synthesis, which can result in dangling free amine groups that do not have a corresponding aldehyde group to form an imine bond, forming defective CC3-R materials.

Despite CC3-R materials' potential defect-engineering and applications mentioned above, the viability of CC3-R materials in industrial conditions depends on structural resilience to aggressive contaminants such as humid acid gas, because those aggressive contaminants commonly exist in industry processes. [17-18] Our work addresses

for the first time the chemical stability of CC3-R materials under exposure to acid gases, specifically humid SO_2.

4.2 Methods and Computational Details

4.2.1 Reaction Formation Energy Calculations

Intermediates and cages of CC3-R, and CC-pentane structures and defective CC3-R structures were initially optimized at the B3LYP[19-20] level using the DZVP2 basis set[21]. The initial structures were manually constructed with several different starting geometries to allow for different approaches towards the global minimum. Vibrational frequencies were also calculated for every structure to ensure that each structure was at an energy minimum. Several hybrid DFT functionals, B3LYP, MN15,[22] ωB97X-D,[23] and APFD,[24] were tested to determine the reliability of such functionals for the prediction of processes with many noncovalent interactions. Each method was used to optimize geometries and calculate vibrational frequencies for all of the structures using the DZVP2 basis sets. Different DFT functionals showed noticeably different reaction energies. Among them, APFD and MN15 provided similar reaction energies with APFD providing the most exothermic reaction energies of all the DFT functionals. The ωB97X-D functional provided less exothermic reaction energies than MN15 and APFD, and B3LYP provided the least exothermic reaction energies. To capture the effect of solvent on the formation energies of CC3-R, CC-pentane, and corresponding intermediates, the single point formation energies in three different solvents, including dichloromethane ($\varepsilon = 8.93$), chloroform ($\varepsilon = 4.7113$), and tetrahydrofuran ($\varepsilon = 7.4257$) were calculated using a self-consistent reaction field (SCRF) approach[25] with both PCM parameters[26] and the

COSMO parameters[27]. The single point free energies with solvent corrections were calculated at the APFD/DZVP2 level on APFD/DZVP2 optimized gas phase structures. DFT calculations were performed using either the Gaussian 09 package[28] or Gaussian 16 package[29].

Table 4.1 shows the solution phase formation energies of all the intermediates observed in CC3-R and CC-pentane in dichloromethane, chloroform, and tetrahydrofuran using both PCM model and COSMO model. Table 4.2 shows the reaction energies of all the intermediates observed in CC-pentane, CC3-R, and defective CC3-R synthesis reactions using different DFT functionals and MP2.

Table 4.1 Formation energies calculations with solvent correction for CC3-R, CC-pentane, and corresponding intermediates with the presence of three solvents calculated using APFD functional in both PCM and COSMO solvent models.

CC3-R formation energies with solvent correction calculated with APFD functional (kJ/mol)							
		PCM			COSMO		
Structure	Gas Phase	DCM	$CHCl_3$	THF	DCM	$CHCl_3$	THF
$(TFB)_1(DACH)_1(H_2O)_{-1}$	-9.57	-4.83	-4.51	-4.76	-8.49	-7.62	-8.25
$(TFB)_1(DACH)_2(H_2O)_{-2}$	-8.41	-15.44	-14.62	-15.27	-24.43	-22.58	-23.97
$(TFB)_1(DACH)_3(H_2O)_{-3}$	-3.55	-5.86	-4.29	-5.42	-5.93	-4.90	-5.76
$(TFB)_2(DACH)_3(H_2O)_{-5}$	-87.58	-94.28	-93.47	-94.10	-111.57	-108.76	-110.63
$(TFB)_2(DACH)_3(H_2O)_{-6}$	-93.67	-111.95	-109.93	-111.49	-130.63	-128.33	-130.24
$(TFB)_2(DACH)_4(H_2O)_{-6}$	-81.26	-95.34	-93.34	-94.86	-114.62	-112.31	-114.21
$(TFB)_3(DACH)_5(H_2O)_{-9}$	-172.29	-194.69	-191.00	-193.79	-226.03	-222.19	-225.33
$(TFB)_4(DACH)_6(H_2O)_{-12}$	-248.82	-284.22	-279.10	-282.99	-325.96	-320.04	-324.85

CC-pentane formation energies with solvent correction calculated with APFD functional (kJ/mol)							
		PCM			COSMO		
Structure	Gas Phase	DCM	$CHCl_3$	THF	DCM	$CHCl_3$	THF
$(TFB)_1(PDA)_1(H_2O)_{-1}$	-16.16	-19.66	-19.97	-19.77	-14.09	-13.73	-13.99
$(TFB)_1(PDA)_2(H_2O)_{-2}$	-30.57	-27.07	-35.58	-26.96	-29.61	-28.12	-29.18
$(TFB)_1(PDA)_3(H_2O)_{-3}$	-44.10	-32.13	-31.35	-31.96	-41.62	-51.14	-41.26
$(TFB)_2(PDA)_3(H_2O)_{-5}$	-120.05	-129.56	-129.09	-129.56	-130.19	-130.09	-130.24
$(TFB)_2(PDA)_3(H_2O)_{-6}$	-155.51	-174.41	-172.45	-173.94	-183.30	-181.45	-183.00
$(TFB)_2(PDA)_4(H_2O)_{-6}$	-81.26	-101.28	-99.46	-100.96	-108.28	-114.72	-118.85
$(TFB)_3(PDA)_6(H_2O)_{-9}$	-113.92	-122.07	-128.96	-121.79	-150.52	-149.25	-150.38
$(TFB)_4(PDA)_6(H_2O)_{-12}$	-117.75	-155.23	-151.09	-154.22	-191.47	-186.25	-190.43

Table 4.2 Reaction energies, ΔG_{298K}(kJ/mol), calculated using several candidate DFT/DZVP2 methods and MP2/aug-cc-pVDZ/cc-pVDZ for all intermediates in the CC3-R, CC-pentane, and CC3-R defect synthesis reactions.

CC3-R						
Structure	Name	B3LYP	MN15	ωB97XD	APFD	MP2
$(TFB)_1(DACH)_1(H_2O)_{-1}$	[1+1]	1.4	-7.6	-3.1	-9.6	-25.5
$(TFB)_1(DACH)_2(H_2O)_{-2}$	[1+2]	9.7	-10.2	-2.0	-8.4	-45.2
$(TFB)_1(DACH)_3(H_2O)_{-3}$	[1+3]	25.2	-5.2	6.8	-3.6	-61.1
$(TFB)_2(DACH)_3(H_2O)_{-5}$	[2+3]	-21.5	-71.5	-59.5	-87.6	-197.5
$(TFB)_2(DACH)_3(H_2O)_{-6}$	Small Cage	-0.1	-77.4	-54.2	-74.1	-244.8
$(TFB)_2(DACH)_4(H_2O)_{-6}$	[2+4]	-11.7	-69.9	-50.5	-81.3	-220.5
$(TFB)_3(DACH)_5(H_2O)_{-9}$	[3+5]	-43.1	-142.7	-126.3	-172.3	-360.9
$(TFB)_4(DACH)_6(H_2O)_{-12}$	[4+6]	-133.0	-211.4	-190.9	-248.8	-528.9

CC-pentane						
Structure	Name	B3LYP	MN15	ωB97XD	APFD	MP2
$(TFB)_1(PDA)_1(H_2O)_{-1}$	[1+1]	-8.0	-16.7	-12.3	-16.2	-34.4
$(TFB)_1(PDA)_2(H_2O)_{-2}$	[1+2]	-10.2	-30.1	-21.0	-30.6	-67.4
$(TFB)_1(PDA)_3(H_2O)_{-3}$	[1+3]	-10.3	-39.8	-22.7	-44.1	-94.6
$(TFB)_2(PDA)_3(H_2O)_{-5}$	[2+3]	-37.4	-107.6	-90.5	-120.1	-231.0
$(TFB)_2(PDA)_3(H_2O)_{-6}$	Small Cage	-77.3	-134.7	-115.6	-155.5	-267.0
$(TFB)_2(PDA)_4(H_2O)_{-6}$	[2+4]	-25.6	-82.5	-62.8	-91.2	-208.0
$(TFB)_3(PDA)_6(H_2O)_{-9}$	[3+6]	-24.7	-89.6	-63.8	-113.9	-310.9
$(TFB)_4(PDA)_6(H_2O)_{-12}$	[4+6]	-28.9	-117.6	-69.2	-117.8	-334.3

CC3-R Defect						
Structure	Name	B3LYP	MN15	ωB97XD	APFD	MP2
$(TFB)_2(IPA)_1(DACH)_4(H_2O)_{-8}$	IC1	-56.0	-127.5	-109.1	-151.4	-359.8
$(TFB)_2(IPA)_2(DACH)_5(H_2O)_{-10}$	IC2	-86.5	-157.4	-141.4	-182.9	-392.5
$(TFB)_3(DACH)_5(H_2O)_{-9}$	IC3	-43.1	-142.7	-126.3	-172.3	-360.9
$(TFB)_3(IPA)_1(DACH)_5(H_2O)_{-10}$	IC4	-95.3	-164.9	-148.3	-201.3	-387.2
$(TFB)_3(IPA)_1(DACH)_6(H_2O)_{-11}$	IC5	-92.6	-172.3	-158.8	-205.6	-437.3
$(TFB)_3(IPA)_1(DACH)_7(H_2O)_{-11}$	IC6	-49.5	-135.8	-114.3	-166.9	-368.1

4.2.2 Isotherm Simulations

CO_2 and N_2 adsorption isotherms on CC3-R-related species were computed using Grand Canonical Monte Carlo (GCMC) simulations in RASPA[30]. The CC3-R structure model used in this adsorption study was from the Cambridge Crystallographic Database

and the defective cage models (IC2, IC4, and IC5) were derived from the CC3-R structure model, with each parent CC3-R cage changing to the corresponding defective cage and following the same packing motif as CC3-R. Before conducting GCMC simulations, all the defective cage models were further optimized by DFT calculations using vdW-DF2 van der Waals-corrected density functional in the Vienna Ab initio Simulation Package (VASP). Lennard-Jones (LJ) and Coulombic potentials were combined to describe the guest molecule - guest molecule and guest molecule - cage interactions with Lorentz-Berthelot (LB) mixing rules. LJ parameters of all the CC3-R related species were taken from the scaled DREIDING force field (scaling parameter: 0.69 to the original ε parameter), previously used in work from Cooper and colleagues,[31] and that of N_2 and CO_2 were taken from original DREIDING force field. Force field parameters are shown in Table 4.3 and Table 4.4, and corresponding definition of atom types are shown in Figure 4.1. The CC3-R-related species' structures were treated as rigid during GCMC simulations. N_2 was modeled as a three-site model with two sites located at the two N atoms and the third one located at its center of mass, and CO_2 was also modeled as a three-site model with two sites located at the two O atoms and the third one located at the C atom. 50,000 initial cycles were applied for the system to reach equilibrium, and another 100,000 cycles were applied to calculate the average adsorption properties.

Table 4.3 Force field parameters for IC5 and CC3.

	ε/kB (K)	σ (Å)	q (e)
N1	26.83	3.2626	-0.6185
N2	26.83	3.2626	-0.8960
C1	32.97	3.4730	-0.3289
C2	32.97	3.4730	0.1870
C3	32.97	3.4730	0.3256
C4	32.97	3.4730	0.2982
C5	32.97	3.4730	-0.2024
C6	32.97	3.4730	-0.0554
C7	32.97	3.4730	0.0426
H1	5.27	2.8464	0.1433
H3	5.27	2.8464	0.0195
H4	5.27	2.8464	0.0138
H5	5.27	2.8464	0.0750
H6	5.27	2.8464	0.0339
H7	5.27	2.8464	0.3150
H8	5.27	2.8464	0.1370
O_co2	79	3.05	-0.35
C_co2	27	2.8	0.7
N_n2	36	3.310	-0.482
N_com	0	0	0.964

Table 4.4 Force field parameters for IC2 and IC4.

	ε/kB (K)	σ (Å)	q (e)
N1	26.83	3.2626	-0.6185
N2	26.83	3.2626	-0.9029
C1	32.97	3.4730	-0.3289
C2	32.97	3.4730	0.1870
C3	32.97	3.4730	0.3256
C4	32.97	3.4730	0.2982
C5	32.97	3.4730	-0.2024
C6	32.97	3.4730	-0.0554
C7	32.97	3.4730	0.44
C8	32.97	3.4730	0.2902
C9	32.97	3.4730	0.0426
O1	33.23	3.0330	-0.5546
H1	5.27	2.8464	0.1433
H3	5.27	2.8464	0.0195
H4	5.27	2.8464	0.0138
H5	5.27	2.8464	0.0750
H6	5.27	2.8464	0.0339
H7	5.27	2.8464	0.29
H8	5.27	2.8464	0.01
H9	5.27	2.8464	0.143

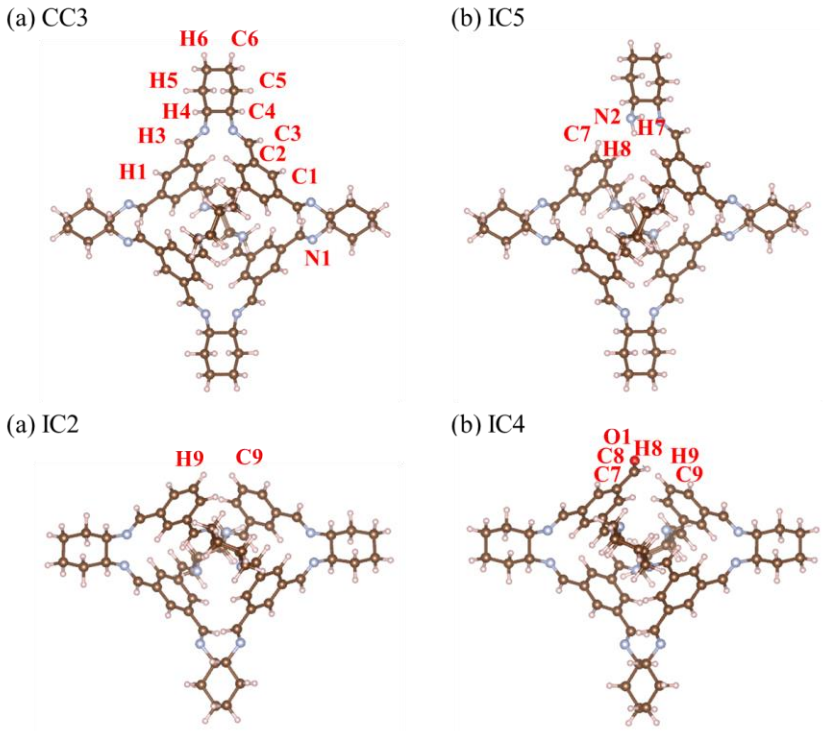

Figure 4.1 Definition of atom types in (a) CC3, (b) IC5, (c) IC2, and (d) IC4.

Further CO_2 adsorption energies on CC3-R and selected defective cages were performed by DFT calculation using vdW-DF2 functional method in VASP, with one CO_2 molecule adsorbed on periodic cage models. Adsorption energies were calculated as the energy difference between the CO_2-loaded cage energy and the sum of the isolated CO_2 energy and pure cage energy.

4.2.3 Degradation Reaction Calculations

All DFT calculations, including molecule geometry optimization and analysis of vibrational modes, were performed by using the B3LYP functional with the 6-31G(d,p) basis set in the Gaussian09 package.[28] Each calculation examined a single CC3-R molecule or its derivative structure. In order to better compare calculated vibrational

frequencies to experimentally measured IR spectra all the calculated vibrational modes were scaled by a factor of 0.9613, which has previously been established as appropriate for the B3LYP functional.[32]

4.3 Formation Mechanisms of Imine-Based Porous Organic Cages

Figure 4.2 shows the synthesis route for both CC3-R and CC-pentane. CC3-R is formed via [4+6] cycloimination reaction between triformylbenzene (TFB) and (1R,2R)-(−)-1,2-diaminocyclohexane.[1] In CC3-R cage, four planar benzene units are linked by six cyclohexane group vertices, resulting in four triangular windows existing in a tetrahedral arrangement around the center of each cage. CC-pentane is formed via [2+3] cycloimination reaction between triformylbenzene (TFB) and 1,5-pentane-diamine.[14] In CC-pentane cage, two planar benzene units are linked by three pentane group vertices, resulting in three rectangular windows embracing into a triangle around the cage center. The problem that we want to address here is what the formation mechanisms of imine-based POCs are, exploring the intermediates between reactant linkers and final cage products.

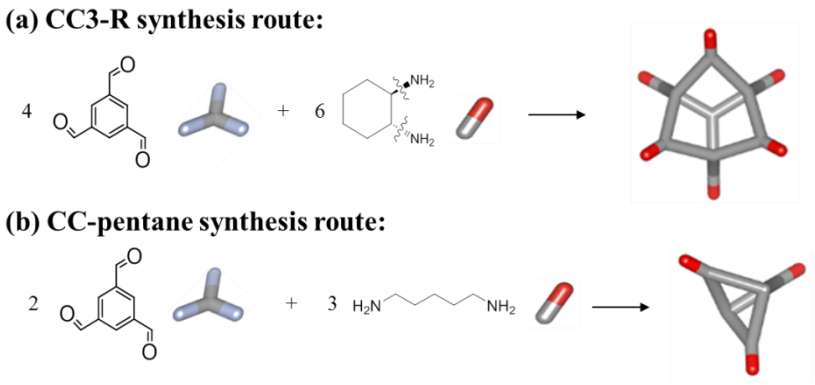

Figure 4.2 Synthesis route of (a) CC3-R and (b) CC-pentane. A blue tail signifies an unreacted carboxaldehyde group. Both of the amine groups in diaminocyclohexane are omitted for clarity, and the connectivity can be determined by totalling the gray cylinders connected to red dots.

4.3.1 Time-Resolved Mass Spectrometry (Provided by Guanghui Zhu)

Firstly, time-resolved mass spectrometry was utilized to track the reaction pathways of both CC3-R and CC-pentane. This work was done by my collaborator, Guanghui Zhu. Time-resolved mass spectrometry results inferred similar reaction pathways of both CC3-R and CC-pentane. That is, upon mixing of the linkers, localized random assembly immediately occurred between the linkers to form a wide range of intermediates. These intermediates were transformed to several species with certain metastable geometries in a short time period. The metastable species were then slowly converted to the desired cages, while a small amount of incomplete cages or undesired byproducts remain in the final product. Figure 4.3 shows the formation mechanism of CC3-R cage.

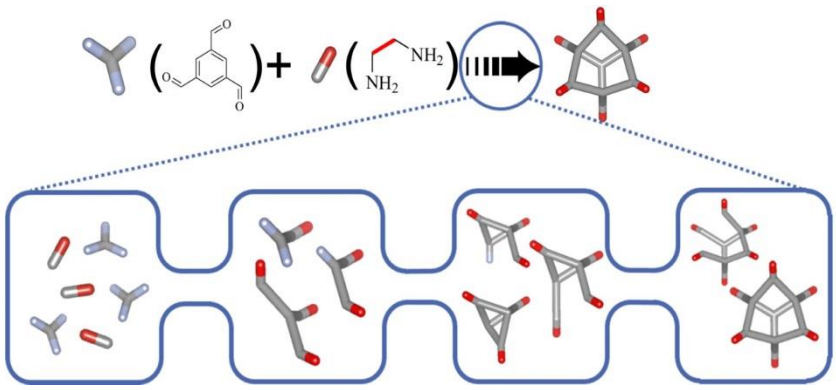

Figure 4.3 Simplified representations of formation mechanism of CC3-R cage.

4.3.2 Theoretical Validation of CC3-R and CC-pentane Reaction Mechanisms

With the help of assigning molecular mass peaks occurred during time-resolved mass spectrometry measurement to specific intermediate species, the proposed intermediates between reactant linkers and final cage products were identified. To validate and explain the observed pathways of forming CC3-R and CC-pentane, we performed electronic structure calculations on the formation energies of the proposed intermediates along the reaction pathway using both correlated MO theory (2^{nd} order Møller–Plesset perturbation theory (MP2)) and density functional theory (DFT) approaches. (MP2 calculations were performed by Luis Flores and Zachary Lee) Figure 4.4 and Figure 4.5 show the reactions used for energy calculations for all the stable intermediates observed in CC3-R and CC-pentane synthesis reactions. The reaction formation energy of each species was calculated as the energy difference between products and reactants, and a negative reaction formation energy corresponds to an energetically favorable process.

The formation energies of intermediates observed in the CC3-R synthesis were calculated at the MP2 level with the aug-cc-pVDZ and aug-cc-pVTZ basis sets, shown in Figure 4.6 (a).[33-36] The aug-cc-pVDZ and aug-cc-pVTZ basis sets were chosen as a result of their better ability to capture the weak van der Waals interactions in these structures. All reactions were predicted to be exothermic, strongly suggesting that the POC formation mechanisms observed by time-resolved MS are facile under mild conditions. In particular, the formation energy of the [2+3] cage (-244.8 kJ/mol per [2+3] unit) is only slightly lower than that of the [4+6] cage (-264.4 kJ/mol per [2+3] unit), which aligns with the experimental observation of this species during the CC3-R formation reaction. This kind of information will be inaccessible without knowing details of the reaction system illustrated with our experiments.

The CC-pentane results are shown in Figure 4.6 (b). For CC-pentane, the [2+3] cage possesses the lowest formation energy per [2+3] unit, in contrast to CC3-R. Although we have not computed reaction barriers for these reactions, these results support the proposed general imine-based POC formation pathway observed by mass spectrometry.

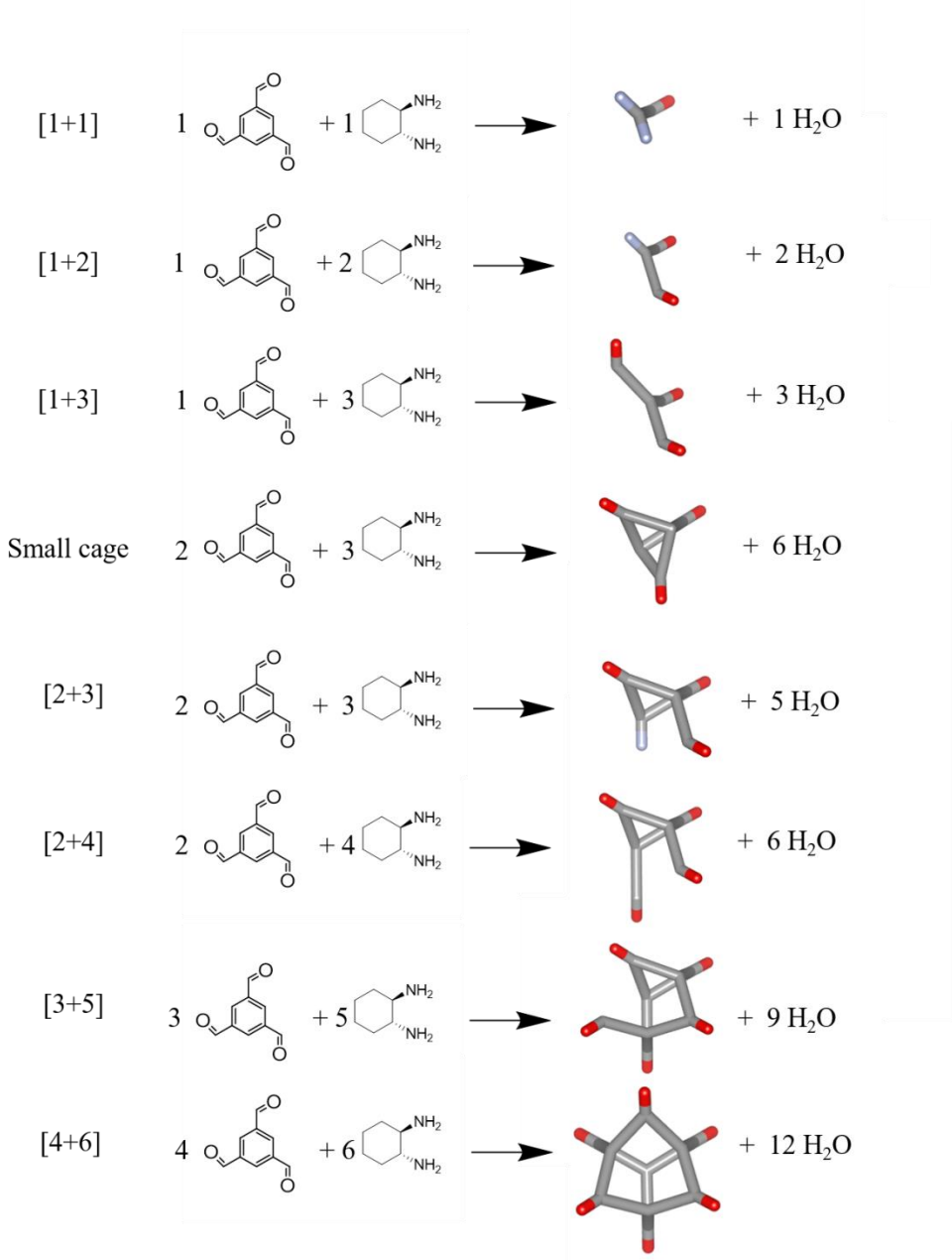

Figure 4.4 Reaction schemes of the stable intermediates observed during CC-3 synthesis process.

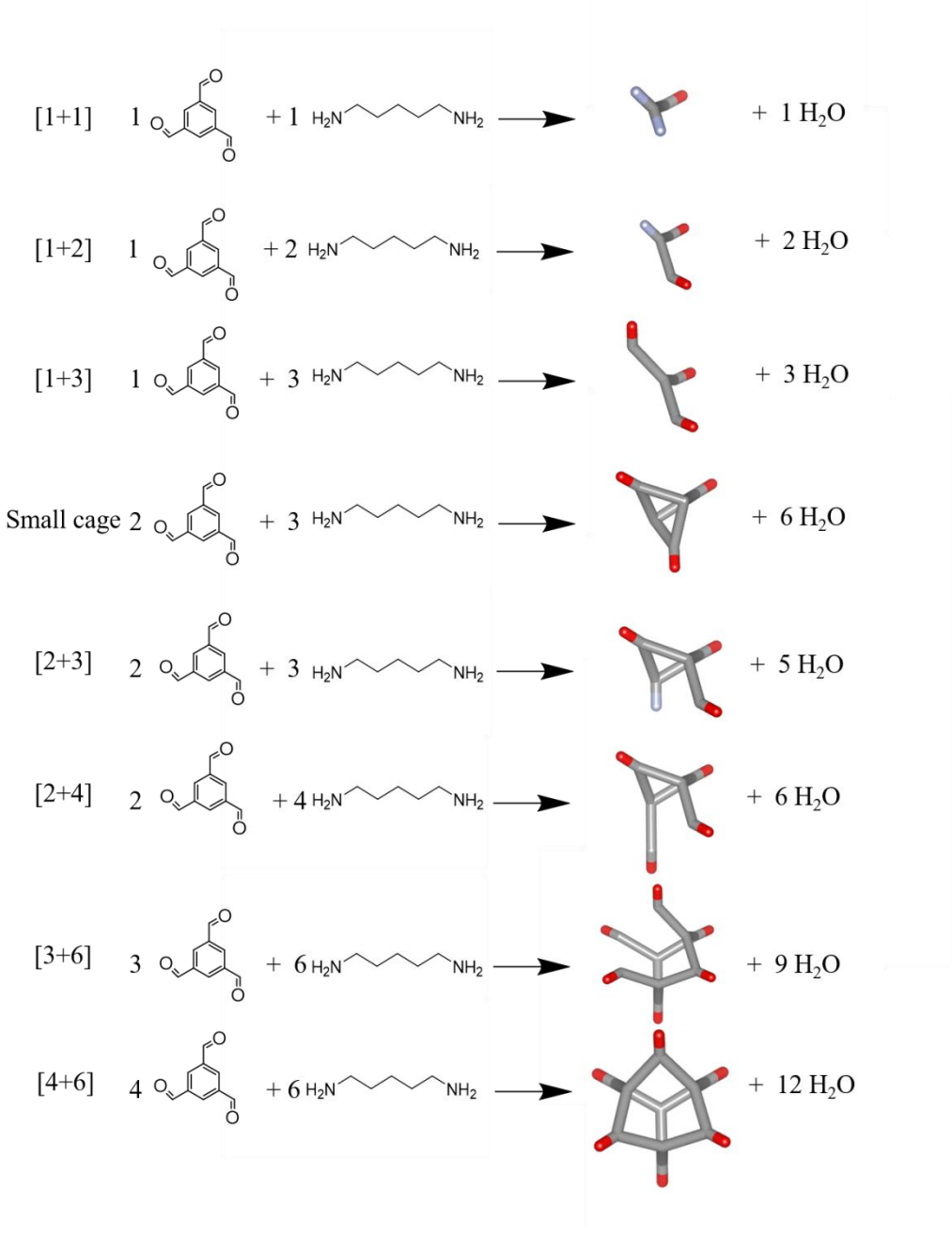

Figure 4.5 Reaction schemes of the stable intermediates observed during CC-pentane synthesis process.

(a) (b)

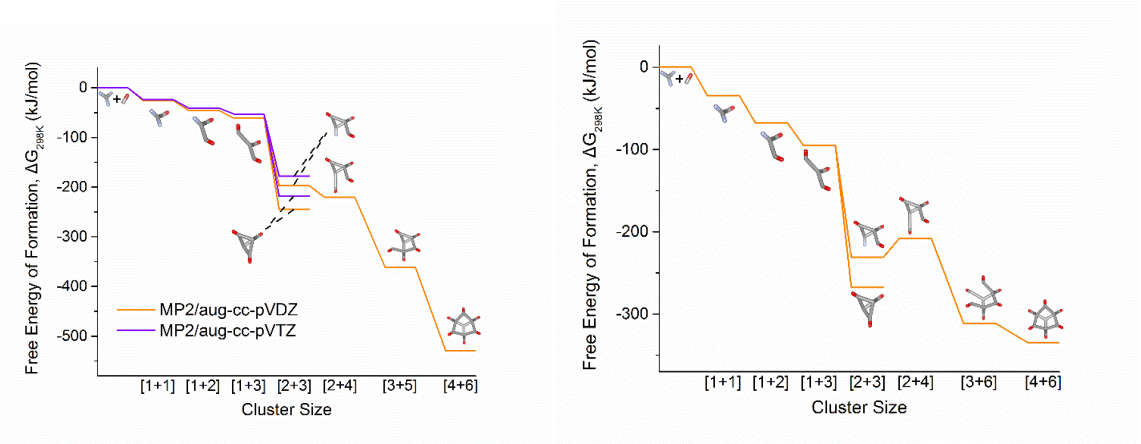

Figure 4.6 (a) Reaction formation energies of species identified during CC3-R synthesis calculated at MP2 level with different basis sets. The calculations with aug-cc-pVTZ were only carried out up to the [2+3] cage because of increasing computational cost. (b) Reaction formation energies of species identified during CC-pentane synthesis calculated at the MP2/aug-cc-pVDZ level.

Although the MP2 calculations are more accurate in terms of absolute energy values, it is more convenient to use far more computationally efficient DFT methods for large scale screening of structures. Thus, the formation energies calculated with MP2 were used as a standard to evaluate several DFT methods. Several DFT functionals, including a hybrid functional (B3LYP) [19-20], a global-hybrid exchange-correlation density functional (MN15) [22], and two dispersion corrected functionals (ωB97XD[23] and APFD[24]) with the DZVP2 basis set, were used to optimize and calculate the corresponding reaction formation energies of the intermediate structures listed in Table 4.5 and plotted in Figure 4.7.[19-24] The results from the DFT methods were compared to MP2 by using percentage deviation metric (PDM), which was calculated as $PDM = \frac{|E_{DFT} - E_{MP2}|}{E_{MP2}} \times 100$. Figure 4.8 shows the calculated PDM for all the intermediates as well as CC3-R cage and CC-

pentane cage by using above four DFT methods.. Among these, the APFD functional gave both the least deviation from the MP2 results and the best trend prediction. The reaction formation energy comparison between the B3LYP functional and ωB97XD/APFD functionals showed the necessity of incorporating dispersion corrections in the DFT functionals for capturing the long-range van der Waals interactions. The MN15 functional, which has good performance for noncovalent interactions also offered good results. A closely related functional M06-2X, has recently been used in exploring the feasibility of energy calculations in POC topology prediction.[37]

(a) (b)

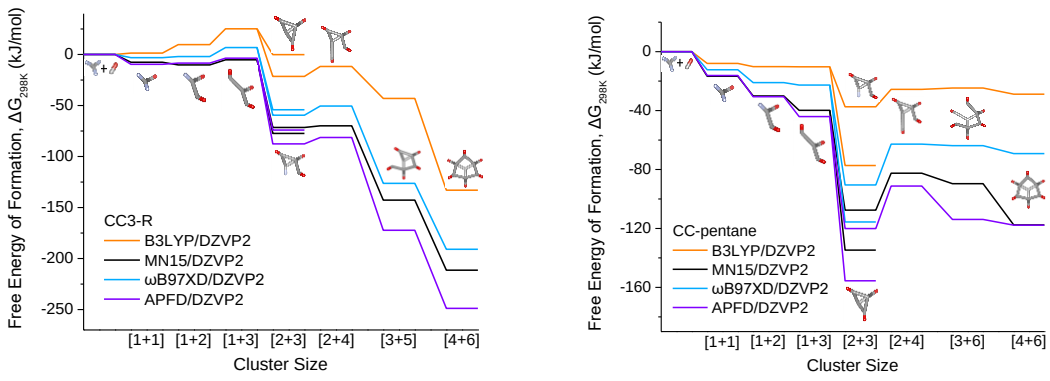

Figure 4.7 Reaction formation energies of species identified during (a) CC3-R and (b) CC-pentane synthesis calculated with B3LYP, MN15, ωB97XD, and APFD functionals and DZVP2 basis set.

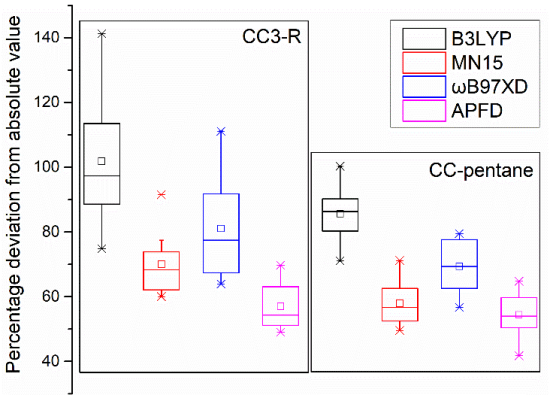

Figure 4.8 Comparison of energy values between DFT methods and MP2 methods for both CC3-R formation and CC-pentane formation.

It is important to note that the above calculations are all gas phase energy calculations. In reality, cage syntheses are carried out in solution, where the choice of solvent may have a considerable effect on cage formation.[38] Here, we consider the case that the solvent only affects the relative stability of species. To accurately capture the effect of solvent, we considered two types of implicit solvent models, including polarizable continuum model (PCM) and conductor-like screening model (COSMO), both of which treat the solvent as a polarizable continuum medium rather than explicit solvent molecules, thus making the electronic structure calculations computationally feasible.[26-27] Three types of solvent were considered in this work: dichloromethane (ε = 8.93), chloroform (ε = 4.7113), and tetrahydrofuran (ε = 7.4257). These three solvents have been shown to affect porous organic cage formation.[38] Formation energy calculations for CC3-R, CC-pentane, and corresponding intermediates with the presence of three solvents were calculated using the APFD functional in both PCM and COSMO solvent models and are shown in Figure 4.9. In general, the solvent corrections made the formation energies of the intermediate and cage species more negative, indicating more

energetically favorable reactions facilitated by the presence of solvent relative to the gas phase calculations.

(a) (b)

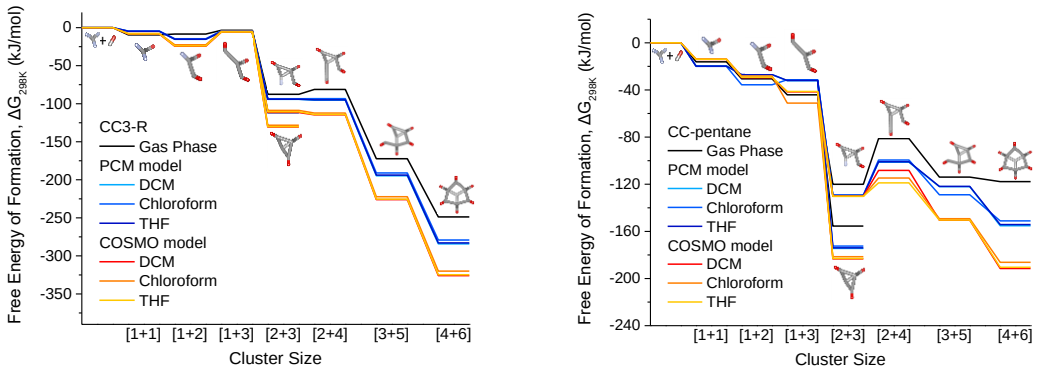

Figure 4.9 Formation energy calculations with solvent correction for CC3-R, CC-pentane, and corresponding intermediates with the presence of three solvents calculated using APFD functional in both PCM and COSMO solvent models.

4.3.3 Summary

As a summary for this section, we investigated and understood the formation mechanisms of both CC3-R and CC-pentane, two imine-based POCs. We also observed that synthesized CC3-R based on literature procedure in fact is not pure, but several other stable intermediates coexist with CC3-R cage in the product. This information was not available in the literature. Therefore, extra synthetic or purification precautions need to be considered to acquire pure CC3-R cage product. In addition, through extended electronic structure calculations, we demonstrated that the APFD/DZVP2 basis set is suitable for qualitative evaluation of the size and permanent porosity of cage products backed by both experimental observations and higher level calculations.

4.4 Defect Engineering of Imine-Based Porous Organic Cages

4.4.1 Formation Energy Evaluation of Defective CC3-R

Defective CC3-R materials with pre-installed defects were synthesized by Guanghui Zhu according to Figure 4.10. In addition to TFB, IPA was incorporated into CC3-R, as compared to pristine CC3-R. Similar to exploring the formation mechanism of CC3-R, mass spectrometry was used to characterize the composition of defective CC3-R materials. Six incomplete cages as well as pristine CC3-R cage were observed with simplified structures shown in Table 4.5. All the incomplete cages (IC) share a similar geometry with the parent cage. No cages or intermediates larger than CC3-R were observed. Figure 4.11 shows the reaction schemes of the stable intermediates observed during defective CC3-R synthesis process. The free energies of reaction formation for all the structures listed in Table 4.5 were calculated at the APFD/DZVP2 level and listed under the structures. In addition to the reaction formation energies of the individual species, the average reaction formation energies per imine bond within each structure were also calculated. CC3-R exhibits the lowest formation energy among all structures investigated, in agreement with the MS spectra, which suggest the majority of the crystal sample is made up of CC3-R cages. Judging from the average reaction formation energies per imine bond, other than IC6, whose connection geometries are hindered by steric effects, the remaining species share similarly stable reaction formation energies per bond within ~ 2 kJ/mol. Although the reaction formation energy of CC3-R is lower than the defective species, the energy differences are small enough to indicate that defective cages may be present at low concentrations after synthesis of CC3-R if the synthesis reaction is stopped before full equilibrium is reached.

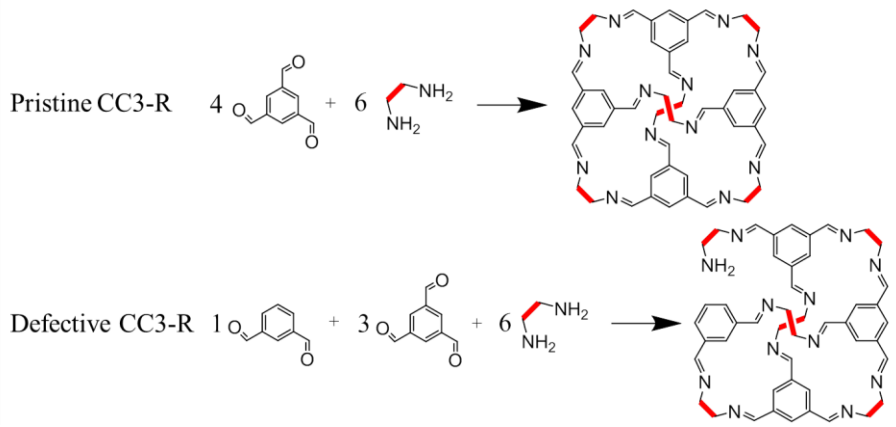

Figure 4.10 Synthesis scheme of CC3-R and one possible structure of defective CC3-R molecules.

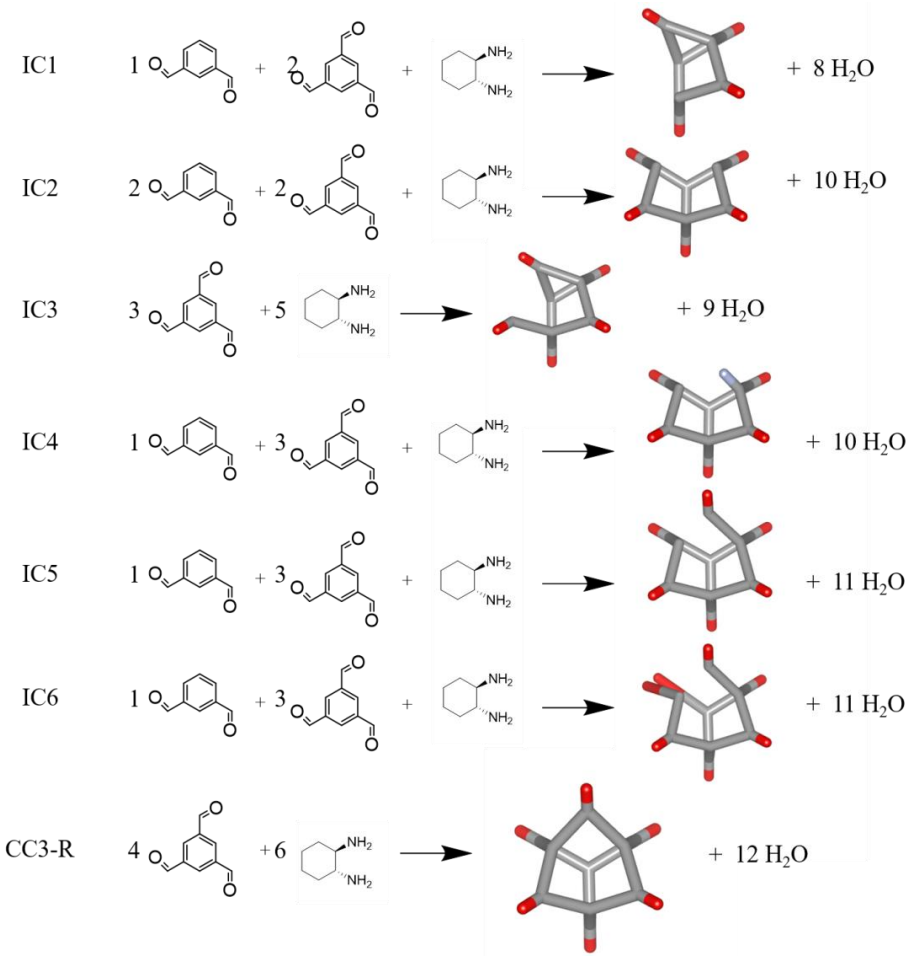

Figure 4.11 Reaction schemes of the stable intermediates observed during defective CC3-R synthesis process.

Table 4.5 Defect species identified by mass spectrometry in defective CC3-R materials and their formation energies at the APFD/DZVP2 level.

	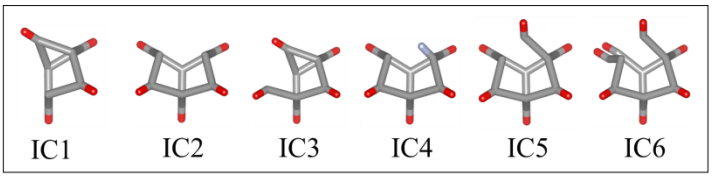 IC1	IC2	IC3	IC4	IC5	IC6	 CC3-R
Formation Energy [kJ/mol]	-151.4	-182.9	-172.3	-201.3	-205.6	-166.9	-248.8
Formation Energy per Imine Bond [kJ/mol]	-18.93	-18.29	-19.14	-20.13	-18.69	-15.17	-20.73

4.4.2 CO_2 Interactions on Defective CC3-R

The effect of incomplete cages inside the crystal on guest interaction was evaluated using N_2 and CO_2 physisorption isotherms. Experimentally measured N_2 and CO_2 adsorption isotherms on pristine CC3-R materials (marked as CC3-R fast crystallization) and two defective CC3-R materials (marked as CC3-R-IPA-a and CC3-R-IPA-b) were shown in Figure 4.12 (a) and (b). The experimental data were provided by Guanghui Zhu. Defective CC3-R materials showed decreased surface areas but enhanced CO_2 interaction and improved CO_2 uptake capacity. The hypothesized reason was that the defective cages within the defective CC3-R materials possess more functional groups that may have additional electrostatic interactions with the sorbates.

GCMC isotherm simulations and cage-specific DFT calculations on guest interactions were carried out to explore CO_2 interactions on defective CC3-R materials.[30] For the GCMC simulation, we used the scaled DREIDING force field to capture the interaction between the cage crystals and sorbate molecules. Good agreement can be

found between the isotherms of N_2 and CO_2 for CC3-R generated by GCMC simulations and experiments as shown in Figure 4.12 (a) and (b). To evaluate the isotherms of defective species, we generated new crystal structures that were composed of only one type of defective species that followed the same packing motif as defect-free CC3-R. Based on our formation energy calculations, we chose IC2, IC4, and IC5, as they have similar formation energies to CC3-R on a per cage basis as well as a per imine bond basis. The N_2 and CO_2 isotherms for selected defect species are shown in Figure 4.12 (c) and (d). Although this simplification in the crystal model may deviate from reality where the packing of defect species may not follow the same packing motif as CC3-R, it provides information on the trend of the change in uptake and guest binding sites based on defect structures and types. For CO_2, the simulated adsorption loadings on the defective species were higher than the parent CC3-R cages both at low pressure and high pressure, in agreement with experimentally measured CO_2 isotherms. The enhanced CO_2 loading calculated in the low pressure region can be attributed to stronger adsorption sites provided by additional functional groups occurring in the defective species: -CHO functional group in model IC4, and -NH_2 functional groups in model IC5. To further help examine the enhanced binding strength with these functional groups, we performed DFT calculations on the following sites to show the CO_2 binding energetics with: (i) the cage center, (ii) dangling -CHO functional group, and (iii) dangling -NH_2 functional group. These calculations were carried out within all selected defective species and parent CC3-R separately, shown in Table 4.6. Figure 4.13 highlights the DFT-optimized CO_2 adsorption configurations at the cage center in parent CC3-R, and adjacent to the dangling -NH_2 functional group in model IC5, respectively. As a result of the dipole

interactions between the partial positively charged carbon atom in CO_2 and partial negatively charged atoms in the defective species (i.e., the nitrogen atom in $-NH_2$), the calculated CO_2 binding strength with defective species were found to be higher than that at the cage center in parent CC3-R.

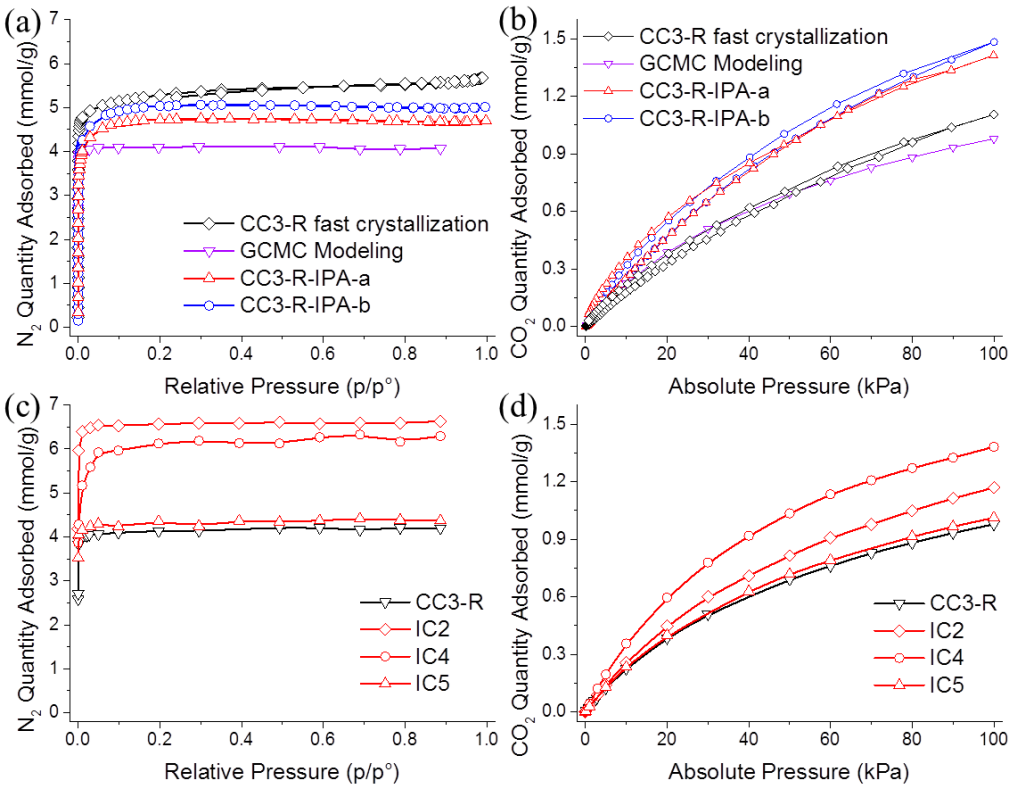

Figure 4.12 (a) N_2 isotherms at 77 K for "defect free" CC3-R and two defective CC3-R materials. (b) CO_2 isotherms at 308 K for "defect free" CC3-R and two defective CC3-R materials. GCMC isotherm modeling of CC3-R is shown in black. (c) GCMC isotherm modeling of N_2 physisorption in CC3-R and selected incomplete cage models. (d) GCMC isotherm modeling of CO_2 physisorption in CC3-R and selected incomplete cage models.

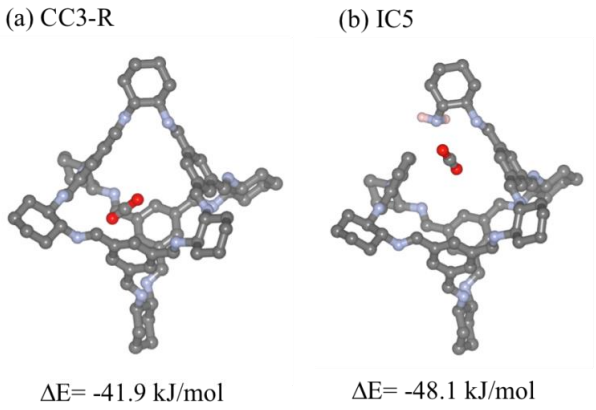

Figure 4.13 DFT optimized CO_2 adsorption configurations and corresponding adsorption energies (a) at the cage center in parent CC3-R, and (b) on -NH_2 functional group in model IC5.

Table 4.6 List of CO_2 binding energies on the cage center, -CHO functional group, an

Binding Energy	IC2	IC4		IC5		CC3
	cage center	cage center	-CHO	cage center	-NH_2	cage center
[kJ/mol]	-42.3	-31.7	-38.6	-23.6	-48.1	-41.9

4.4.3 Summary

As a summary for this section, we successfully introduced "missing-linker" defect into CC3-R materials, synthesizing defective CC3-R materials. The comparison between formation energies of pristine CC3-R cage and defective CC3-R cage indicated the possible existence of defective cages from thermodynamic perspective. The effects of the defective cages on the crystal materials were evaluated with an emphasis on the physisorption of guest molecules (N_2 and CO_2). The defective CC3-R materials are found to have enhanced CO_2 interaction and improved CO_2 uptake capacity due to the additional free functional groups present within the CC3 crystals, supported by both experimentally measured and atomically simulated CO_2 adsorption isotherms. We also

calculated CO_2 adsorption energy to demonstrate that defective CC3-R materials have the capability to adsorb CO_2 more effectively than pristine CC3-R materials.

4.5 Chemical Stability of Imine-Based Porous Organic Cages

4.5.1 Degradation Mechanism Analysis

Through SEM images and *in-situ* IR characterisations performed by Guanghui Zhu, both morphological changes and IR spectra changes of CC3-R materials after exposure to humid and aqueous SO_2 were observed, indicating CC3-R was not stable and experienced chemical degradation with humid SO_2's presence.

DFT calculations, including formation energy calculations and IR frequencies calculations, were performed to help understand the mechanism of the observed instability. All DFT calculations, including molecule geometry optimization and analysis of vibrational modes, were performed by using the B3LYP functional with the 6-31G(d,p) basis set. We first compared IR spectra from DFT calculations to experimental results for pristine CC3-R, shown in Figure 4.14. Good agreement is seen between the experimentally observed and calculated peaks. The broad peak centered at 3250 cm^{-1} corresponds to absorbed atmospheric H_2O and the peaks from 1750 cm^{-1} to 2500 cm^{-1} originate from the ATR module. For CC3-R degradation by exposure to SO_2, we proposed a three-step reaction. First, the imine bond in CC3-R is attacked by HSO_3^{-1}, forming the decomposition intermediate shown in Figure 4.15 (a). Then the attacked imine bond in this decomposition intermediate structure breaks into dangling amine group and aldehyde group in the presence of H_2O, shown in Figure 4.15 (b). Finally, SO_2 can interact with the newly generated amine group in the broken cage, forming the -NH_2-

SO_2 complex shown in Figure 4.15 (c). DFT calculations were performed to optimize the geometry of each intermediate in this process. The formation energies ($\Delta E_{formation}$) for each state along this degradation pathway and the S-O bond lengths in the optimized structures are summarized in Table 4.7. Formation energies were calculated as the energy difference between products and reactants, and positive formation energy corresponds to an energetically favorable process:

$$\Delta E(\text{intermediate}) = -\big(E(\text{intermediate}) - E(CC3-R) - E(H_2SO_3)\big)$$

$$\Delta E(\text{broken cage}) = -\big(E(\text{broken cage}) + E(H_2SO_3) - E(\text{intermediate}) - E(H_2O)\big)$$

$$\Delta E(-NH_2 - SO_2 \text{ complex}) = -\big(E(-NH_2 - SO_2 \text{complex}) - E(\text{broken cage}) - E(SO_2)\big)$$

Each process in this pathway is either energetically favorable or requires only a small amount of energy. Although we have not computed reaction energy barriers for these processes, our results strongly suggest that this degradation pathway is facile under mild conditions.

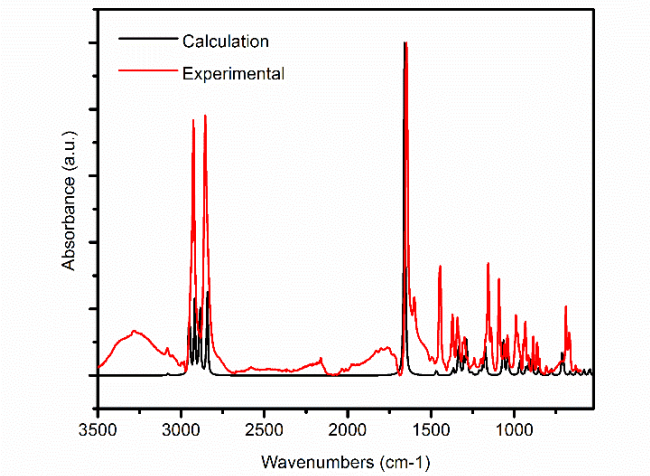

Figure 4.14 Comparison between DFT calculated and experimental results of pristine CC3-R IR spectra.

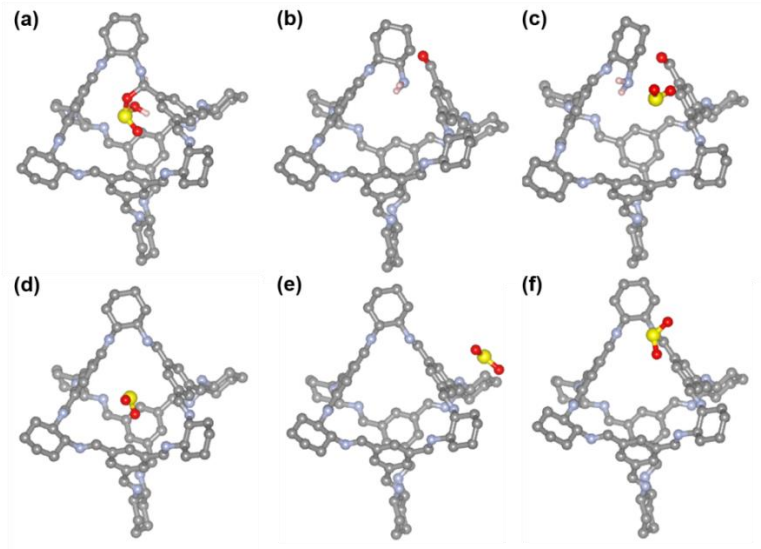

Figure 4.15 Relaxed structure of (a) decomposition intermediate of CC3-R, (b) broken cage, (c) -NH_2-SO_2 complex, (d) SO_2 physisorbed in the center of CC3-R, (e) SO_2 physisorbed near benzene ring outside cage, and (f) SO_2 physisorbed near N outside cage.

Table 4.7 Formation energies ($\Delta E_{formation}$) and corresponding S-O bond lengths of 3 states (decomposition intermediate, broken cage, and -NH_2-SO_2 complex) along the proposed degradation pathway.

Structure	$\Delta E_{formation}$ [kJ/mol]	S-O bond lengths [Å]		
Intermediate	-2.3	1.48	1.66	1.69
Broken cage	8.7	-	-	-
-NH_2-SO_2 complex	10.3	1.47	1.48	-

Using the optimized structures along the degradation pathway described above, the corresponding IR spectra were generated by DFT calculations. Figure 4.16 (a) compares the IR spectra of pristine CC3-R, the decomposition intermediate, and the -NH_2-SO_2 complex. Using the DFT calculated vibrational modes, the peaks in the difference spectra comparing pristine and SO_2 exposed CC3-R were assigned as

summarized in Table 4.8. Physisorption of SO_2 in various positions in the cage (at cage center, near benzene ring outside cage, and near N outside cage (Figure 4.15 (d)-(f)) were also modeled and compared to the pristine CC3-R IR spectra, as shown in Figure 4.16(b). The only new peaks in those three physisorption configurations were the vibrational modes belonging to SO_2, which have negligible shifts compared to gas phase SO_2. This indicates that physisorbed SO_2 does not alter the vibrational properties of CC3-R.

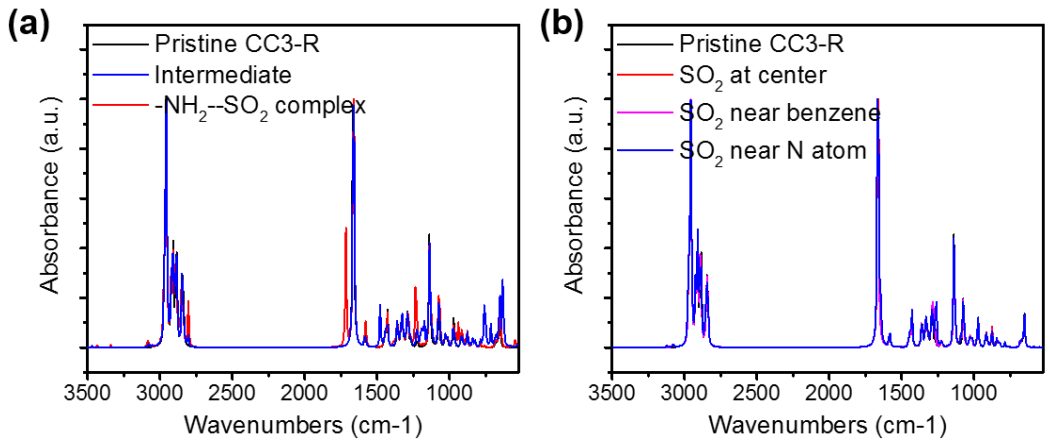

Figure 4.16 DFT calculated (a) IR spectra comparison among pristine CC3-R, decomposition immediate, and -NH_2-SO_2 complex, (b) IR spectra comparison between pristine CC3-R and SO_2 physisorption on CC3-R.

Table 4.8 Assignment summary for peaks in the differential spectra under SO_2 exposure based on DFT calculations.

Wavenumbers [cm^{-1}]	Assignment
715	S-O stretch in intermediate structure
742	C-O stretch (C-O-S) in intermediate structure
893, 922, 952	N-H bend in -NH_2-SO_2 complex
1020	C-N stretch (C-NH_2) in intermediate structure
1050	S=O symmetric stretch -NH_2-SO_2 complex
1072	O-H bend/S=O stretch in intermediate structure
1192	C-N stretch (C-N(H)) in intermediate structure
1228	S=O asymmetric stretch in -NH_2-SO_2 complex
1257	Gas phase SO_2
1353, 1387, 1408	C-H bend (H-C=O) in -NH_2-SO_2 complex
1484	N-H bend in intermediate structure
1541	N-H bend in -NH_2-SO_2 complex
1724	C=O stretch in -NH_2-SO_2 complex
2710	C-H stretch (H-C=O) in -NH_2-SO_2 complex
3010	O···H in -NH_2-SO_2 complex
3175, 3214	N-H stretch in -NH_2-SO_2 complex
3385	N-H asymmetric stretch in -NH_2-SO_2 complex N-H stretch in intermediate structure
3550	O-H stretch in intermediate structure

4.5.2 Summary

As a summary for this section, we addressed for the first time how CC3-R crystal responds to acid gases. We have combined in-situ IR experiments of acid gas degradation with computational insight to propose a detailed acid catalyzed CC3 degradation

pathway. Firstly, the imine bond in CC3-R is attacked by HSO_3^-, forming a decomposition intermediate. Then, the attacked imine bond in decomposition intermediate structure breaks into a dangling amine group and an aldehyde group in the presence of water. Finally, SO_2 can interact with the newly generated amine group in the broken cage, forming a $-NH_2-SO_2$ complex. A comprehensive understanding of the chemical stability and degradation mechanism of CC3-R crystal is helpful for further designing and developing more chemically stable porous organic cage materials.

4.6 References

1. Tozawa, T.; Jones, J. T. A.; Swamy, S. I.; Jiang, S.; Adams, D. J.; Shakespeare, S.; Clowes, R.; Bradshaw, D.; Hasell, T.; Chong, S. Y.; Tang, C.; Thompson, S.; Parker, J.; Trewin, A.; Bacsa, J.; Slawin, A. M. Z.; Steiner, A.; Cooper, A. I., Porous organic cages. *Nature materials* **2009,** *8* (12), 973-978.

2. Mastalerz, M., Shape-Persistent Organic Cage Compounds by Dynamic Covalent Bond Formation. *Angewandte Chemie-International Edition* **2010,** *49* (30), 5042-5053.

3. Jin, Y.; Voss, B. A.; Noble, R. D.; Zhang, W., A Shape-Persistent Organic Molecular Cage with High Selectivity for the Adsorption of CO2 over N-2. *Angewandte Chemie-International Edition* **2010,** *49* (36), 6348-6351.

4. Cooper, A. I., Nanoporous Organics Enter the Cage Age. *Angewandte Chemie-International Edition* **2011,** *50* (5), 996-998.

5. Holst, J. R.; Trewin, A.; Cooper, A. I., Porous organic molecules. *Nature Chemistry* **2010,** *2* (11), 915-920.

6. Sun, J. K.; Zhan, W. W.; Akita, T.; Xu, Q., Toward Homogenization of Heterogeneous Metal Nanoparticle Catalysts with Enhanced Catalytic Performance: Soluble Porous Organic Cage as a Stabilizer and Homogenizer. *J. Am. Chem. Soc.* **2015,** *137* (22), 7063-7066.

7. Song, Q. L.; Jiang, S.; Hasell, T.; Liu, M.; Sun, S. J.; Cheetham, A. K.; Sivaniah, E.; Cooper, A. I., Porous Organic Cage Thin Films and Molecular-Sieving Membranes. *Advanced materials* **2016,** *28* (13), 2629-+.

8. Uemura, T.; Nakanishi, R.; Mochizuki, S.; Kitagawa, S.; Mizuno, M., Radical Polymerization of Vinyl Monomers in Porous Organic Cages. *Angew. Chem. Int. Ed.* **2016,** *55* (22), 6443-6447.

9. Xie, S. M.; Zhang, J. H.; Fu, N.; Wang, B. J.; Chen, L.; Yuan, L. M., A chiral porous organic cage for molecular recognition using gas chromatography. *Anal. Chim. Acta* **2016,** *903*, 156-163.

10. Zwijnenburg, M. A.; Berardo, E.; Peveler, W. J.; Jelfs, K. E., Amine Molecular Cages as Supramolecular Fluorescent Explosive Sensors: A Computational Perspective. *J. Phys. Chem. B* **2016,** *120* (22), 5063-5072.

11. Ortiz, M.; Cho, S.; Niklas, J.; Kim, S.; Poluektov, O. G.; Zhang, W.; Rumbles, G.; Park, J., Through-Space Ultrafast Photoinduced Electron Transfer Dynamics of a C70-Encapsulated Bisporphyrin Covalent Organic Polyhedron in a Low-Dielectric Medium. *J. Am. Chem. Soc.* **2017,** *139* (12), 4286-4289.

12. Slater, A. G.; Little, M. A.; Pulido, A.; Chong, S. Y.; Holden, D.; Chen, L.; Morgan, C.; Wu, X.; Cheng, G.; Clowes, R.; Briggs, M. E.; Hasell, T.; Jelfs, K. E.; Day, G. M.; Cooper, A. I., Reticular synthesis of porous molecular 1D nanotubes and 3D networks. *Nature chemistry* **2017,** *9* (1), 17-25.

13. Pulido, A.; Chen, L. J.; Kaczorowski, T.; Holden, D.; Little, M. A.; Chong, S. Y.; Slater, B. J.; McMahon, D. P.; Bonillo, B.; Stackhouse, C. J.; Stephenson, A.; Kane, C. M.; Clowes, R.; Hasell, T.; Cooper, A. I.; Day, G. M., Functional materials discovery using energy-structure-function maps. *Nature* **2017,** *543* (7647), 657-+.

14. Jelfs, K. E.; Eden, E. G. B.; Culshaw, J. L.; Shakespeare, S.; Pyzer-Knapp, E. O.; Thompson, H. P. G.; Bacsa, J.; Day, G. M.; Adams, D. J.; Cooper, A. I., In silico Design of Supramolecules from Their Precursors: Odd-Even Effects in Cage-Forming Reactions. *Journal of the American Chemical Society* **2013,** *135* (25), 9307-9310.

15. Bennett, T. D.; Cheetham, A. K.; Fuchs, A. H.; Coudert, F.-X., Interplay between defects, disorder and flexibility in metal-organic frameworks. *Nat. Chem.* **2017,** *9* (1), 11-16.

16. Sholl, D. S.; Lively, R. P., Defects in Metal–Organic Frameworks: Challenge or Opportunity? *J. Phys. Chem. Lett.* **2015,** *6* (17), 3437-3444.

17. Sholl, D. S.; Lively, R. P., Defects in Metal-Organic Frameworks: Challenge or Opportunity? *J Phys Chem Lett* **2015**, 3437-3444.

18. Hasell, T.; Schmidtmann, M.; Stone, C. A.; Smith, M. W.; Cooper, A. I., Reversible water uptake by a stable imine-based porous organic cage. *Chemical communications* **2012,** *48* (39), 4689-4691.

19. Becke, A. D., Density-functional thermochemistry. III. The role of exact exchange. *J. Chem. Phys.* **1993,** *98* (7), 5648-5652.

20. Lee, C.; Yang, W.; Parr, R. G., Development of the Colle-Salvetti correlation-energy formula into a functional of the electron density. *Phys. Rev. B* **1988,** *37* (2), 785.

21. Godbout, N.; Salahub, D. R.; Andzelm, J.; Wimmer, E., Optimization of Gaussian-type basis sets for local spin density functional calculations. Part I. Boron through neon, optimization technique and validation. *Can. J. Chem.* **1992,** *70* (2), 560-571.

22. Haoyu, S. Y.; He, X.; Li, S. L.; Truhlar, D. G., MN15: A Kohn–Sham global-hybrid exchange–correlation density functional with broad accuracy for multi-reference and single-reference systems and noncovalent interactions. *Chem. Sci.* **2016,** *7* (8), 5032-5051.

23. Chai, J.-D.; Head-Gordon, M., Long-range corrected hybrid density functionals with damped atom-atom dispersion corrections. *Phys. Chem. Chem. Phys.* **2008,** *10* (44), 6615-6620.

24. Austin, A.; Petersson, G. A.; Frisch, M. J.; Dobek, F. J.; Scalmani, G.; Throssell, K., A density functional with spherical atom dispersion terms. *J. Chem. Theory Comput.* **2012,** *8* (12), 4989-5007.

25. Tomasi, J.; Mennucci, B.; Cammi, R., Quantum Mechanical Continuum Solvation Models. *Chem. Rev.* **2005,** *105* (8), 2999-3094.

26. Miertuš, S.; Scrocco, E.; Tomasi, J., Electrostatic interaction of a solute with a continuum. A direct utilizaion of AB initio molecular potentials for the prevision of solvent effects. *Chem. Phys.* **1981,** *55* (1), 117-129.

27. Klamt, A.; Schuurmann, G., COSMO: a new approach to dielectric screening in solvents with explicit expressions for the screening energy and its gradient. *J. Chem. Soc., Perkin Trans. 2* **1993,** (5), 799-805.

28. Frisch, M. J. T., G. W.; Schlegel, H. B.; Scuseria, G. E.; Robb, M. A.; Cheeseman, J. R.; Scalmani, G.; Barone, V.; Mennucci, B.; Petersson, G. A.; Nakatsuji, H.; Caricato, M.; Li, X.; Hratchian, H. P.; Izmaylov, A. F.; Bloino, J.; Zheng, G.; Sonnenberg, J. L.; Hada, M.; Ehara, M.; Toyota, K.; Fukuda, R.; Hasegawa, J.; Ishida, M.; Nakajima, T.; Honda, Y.; Kitao, O.; Nakai, H.; Vreven, T.; Montgomery, Jr., J. A.; Peralta, J. E.; Ogliaro, F.; Bearpark, M.; Heyd, J. J.; Brothers, E.; Kudin, K. N.; Staroverov, V. N.; Kobayashi, R.; Normand, J.; Raghavachari, K.; Rendell, A.; Burant, J. C.; Iyengar, S. S.; Tomasi, J.; Cossi, M.; Rega, N.; Millam, N. J.; Klene, M.; Knox, J. E.; Cross, J. B.; Bakken, V.; Adamo, C.; Jaramillo, J.; Gomperts, R.; Stratmann, R. E.; Yazyev, O.; Austin, A. J.; Cammi, R.; Pomelli, C.; Ochterski, J. W.; Martin, R. L.; Morokuma, K.; Zakrzewski, V. G.; Voth, G. A.; Salvador, P.; Dannenberg, J. J.; Dapprich, S.; Daniels, A. D.; Farkas, Ö.; Foresman, J. B.; Ortiz, J. V.; Cioslowski, J.; Fox, D. J., Gaussian 09, revision D. 01. Gaussian, Inc., Wallingford CT: 2009.

29. Frisch, M. J. T., G. W.; Schlegel, H. B.; Scuseria, G. E.; Robb, M. A.; Cheeseman, J. R.; Scalmani, G.; Barone, V.; Petersson, G. A.; Nakatsuji, H.; Li, X.; Caricato, M.; Marenich, A. V.; Bloino, J.; Janesko, B. G.; Gomperts, R.; Mennucci, B.; Hratchian, H. P.; Ortiz, J. V.; Izmaylov, A. F.; Sonnenberg, J. L.; Williams-Young, D.; Ding, F.; Lipparini, F.; Egidi, F.; Goings, J.; Peng, B.; Petrone, A.; Henderson, T.;

Ranasinghe, D.; Zakrzewski, V. G.; Gao, J.; Rega, N.; Zheng, G.; Liang, W.; Hada, M.; Ehara, M.; Toyota, K.; Fukuda, R.; Hasegawa, J.; Ishida, M.; Nakajima, T.; Honda, Y.; Kitao, O.; Nakai, H.; Vreven, T.; Throssell, K.; Montgomery, J. A., Jr.; Peralta, J. E.; Ogliaro, F.; Bearpark, M. J.; Heyd, J. J.; Brothers, E. N.; Kudin, K. N.; Staroverov, V. N.; Keith, T. A.; Kobayashi, R.; Normand, J.; Raghavachari, K.; Rendell, A. P.; Burant, J. C.; Iyengar, S. S.; Tomasi, J.; Cossi, M.; Millam, J. M.; Klene, M.; Adamo, C.; Cammi, R.; Ochterski, J. W.; Martin, R. L.; Morokuma, K.; Farkas, O.; Foresman, J. B.; Fox, D. J. , Gaussian 16, Revision A.03. Gaussian, Inc., Wallingford CT: 2016.

30. Dubbeldam, D.; Calero, S.; Ellis, D. E.; Snurr, R. Q., RASPA: molecular simulation software for adsorption and diffusion in flexible nanoporous materials. *Mol. Simul.* **2016,** *42* (2), 81-101.

31. Chen, L.; Reiss, P. S.; Chong, S. Y.; Holden, D.; Jelfs, K. E.; Hasell, T.; Little, M. A.; Kewley, A.; Briggs, M. E.; Stephenson, A.; Thomas, K. M.; Armstrong, J. A.; Bell, J.; Busto, J.; Noel, R.; Liu, J.; Strachan, D. M.; Thallapally, P. K.; Cooper, A. I., Separation of rare gases and chiral molecules by selective binding in porous organic cages. *Nat. Mater.* **2014,** *13* (10), 954-60.

32. J. B. Foresman, *Æ.* F., Exploring Chemistry with Electronic Structure Methods, Gaussian Inc., Pittsburgh, PA, 2nd, ed. **1996**.

33. Head-Gordon, M.; Pople, J. A.; Frisch, M. J., MP2 energy evaluation by direct methods. *Chem. Phys. Lett.* **1988,** *153* (6), 503-506.

34. Pople, J. A.; Binkley, J. S.; Seeger, R., Theoretical models incorporating electron correlation. *Int. J. Quantum Chem.* **1976,** *10* (S10), 1-19.

35. Kendall, R. A.; Dunning Jr, T. H.; Harrison, R. J., Electron affinities of the first-row atoms revisited. Systematic basis sets and wave functions. *J. Chem. Phys.* **1992,** *96* (9), 6796-6806.

36. Møller, C.; Plesset, M. S., Note on an Approximation Treatment for Many-Electron Systems. *Phys. Rev.* **1934,** *46* (7), 618-622.

37. Santolini, V.; Miklitz, M.; Berardo, E.; Jelfs, K. E., Topological landscapes of porous organic cages. *Nanoscale* **2017,** *9* (16), 5280-5298.

38. Liu, X.; Warmuth, R., Solvent Effects in Thermodynamically Controlled Multicomponent Nanocage Syntheses. *J. Am. Chem. Soc.* **2006,** *128* (43), 14120-14127.

CHAPTER 5. *IN SILICO* PREDICTION OF STRUCTURAL PROPERTIES OF RACEMIC POROUS ORGANIC CAGE CRYSTALS

5.1 Introduction

Porous organic cage (POC) solids have shown promising properties and attracted significant attention in applications including gas separation, adsorption, catalysis, and molecular sensing.[1-17] Unlike extended framework materials such as zeolites, covalent organic frameworks and metal-organic frameworks that are connected by covalent or coordination bonds, POC solids are comprised of individual porous molecules held together by relatively weak dispersion packing forces. POC solids can have both extrinsic packing voids and intrinsic cage cavities that form either one, two, or three dimensional pore networks.[18-21] The inclusion of solvent molecules can in some cases change the crystal packing motifs in POC crystals from 2-D pore networks to 3-D interconnected pore networks.[21] Structural mobility of the cages can also bring cooperative interactions between the hosts (POCs) and guest adsorbate molecules.[13] Since POCs are discrete organic molecules, they can be dissolved in common organic solvents without altering the porosity and structure of individual cages.[12, 22-25]

POCs have been synthesized through different dynamic covalent chemistries, including imine condensation reactions.[4, 8, 26] The formation mechanisms of imine-based POCs were investigated in our previous work with a combination of time-resolved electrospray mass spectrometry and electronic structure calculations.[27] Recently, Lucero

et al. observed and analyzed the crystal structure evolution of an imine-based POC as a function of crystallization time.[28] Fundamental studies of this kind are critical to achieving structural and morphological control of POC crystals.

One interesting attribute of POCs is the chirality that can result from imine condensation reactions involving chiral diamines.[2, 15, 29-31] Chiral materials are of intrinsic interest for a variety of fundamental and applied reasons.[32-33] Chirality within POC materials plays an important role in controlling the crystalline assembly of these porous organic molecules.[31, 34] Cooper and co-workers reported that discrete Cage Crystal 3 (CC3) cages with opposite chirality are able to pack more strongly by chiral recognition than CC3 cages with same chirality.[31, 35-36] In addition, intrinsically chiral POCs are interesting candidates for separation of chiral molecules. Chen et al. showed that homochiral CC3 exhibited an enantioselective separation for a chiral alcohol, 1-phenylethanol.[15]

We recently demonstrated that mixed-chirality POC crystals can be synthesized from racemic mixtures of diamines.[37] These materials can be produced by a low-cost synthesis and showed better acid resistance than homochiral POCs. Since imine condensation reactions between trialdehydes and diamines can take place via [2 + 3], [4 + 6], or [8 + 12] cycloiminations, cages with several stoichiometries in addition to the [4 + 6] cycloimine CC3 cage can also be formed. Our earlier work demonstrated that when mixing 1,3,5- triformylbenzene (TFB) and (R,R)-diaminocyclohexane (DACH), CC3 cages with [4+6] topology dominate the final product.[27] It is therefore plausible to assume that these mixed-chirality POC crystals consist of only CC3 cages. This system was further investigated by Cooper and coworkers, where products in the solution were

isolated from the solid product.[38] The liquid phase product was successfully grown as single crystals and it was found that CC3-SR cage and CC3-RS cage (both containing three R,R-DACH vertices and three S,S-DACH vertices) are packed in 1-D alternating chains in the crystal. Nevertheless, the precipitated solid, which accounts for a large proportion of the products, could only be examined using powder X-ray diffraction (PXRD) analysis. These PXRD results were interpreted as this product being a CC3-R/CC3-S cocrystal but could not unambiguously establish this observation. It is challenging to completely describe this new racemic crystal structure because only subtle differences exist between new racemic structure and PXRD patterns for the previously reported CC3 structure. Similar difficulties existed in fully identifying chirality in ordered structures of amino acid adlayers on metal surfaces, even with access to high quality scanning tunneling microscope images.[39-40] The potentially useful properties of the CC3-racemic crystal motivated us to tackle the challenge of further understanding its structure using *in silico* methods.

De novo prediction of POC crystal structures remains challenging. Recently, there have been some efforts to predict the packing of known homochiral organic cages into solid crystals considering some commonly observed space groups.[41-42] This work predicted the crystal energy landscapes of a series of POC crystals with encouraging accuracy. These methods, however, are only currently applicable to predicting the structure of racemic POCs that are mixtures of known enantiopure cages with highly symmetric long-range order. As we will show below, these conditions are not satisfied in CC3-racemic crystals.

In this work, we combine electronic structure calculations and molecular-level calculations to predict the atomic structure of racemic POC crystals. We first calculate the formation energies of all possible isolated CC3-based cages, including homochiral and heterochiral cages. These energies are used to predict the compositions of CC3-racemic crystals. Because the presence of solvents during the cage synthesis can have a significant effect,[43-45] we include solvent effects using an implicit solvent model. Next, all possible window-to-window cage pair packing energies are calculated with density functional theory (DFT). These energies are then used in lattice model-based Metropolis Monte Carlo (MC) simulations to assess cage ordering in CC3-racemic crystals. By expanding the structures from these lattice models, atomically detailed CC3-racemic crystal models are created and then energy-minimized by force field calculations. This allows use to compare the PXRD patterns of crystal models with experimental data.

5.2 Methods and Computational Details

5.2.1 Cage Formation Energy Calculations

All isolated cage structures were optimized at the APFD level using the DZVP2 basis set in the Gaussian 09 package.[46-47] In our earlier work we tested a range of DFT functionals and found that the APFD functional was able to capture the long range non-covalent interactions present in CC3 cages.[27] The initial structures of homochiral CC3 cages (CC3-R and CC3-S) were taken from previous literature.[31] A sequence of mixed chirality CC3 cages, designated as nSmR, where n and m represent the number of S,S-DACH vertices and R,R-DACH vertices, were prepared by substituting the original R,R-DACH linker for S,S-DACH linker in a CC3-R cage. Initial structures were manually

constructed with several different starting geometries and energy minimized in an effort to find the global minimum. Vibrational frequencies were calculated for every structure after energy minimization to ensure that no imaginary frequencies were present. The cage formation energy was defined as the energy difference between the products and reactants, where the products were CC3-based cages and H_2O molecules and the reactants were DACH and TFB molecules. A negative formation energy corresponds to an energetically favorable formation process. Figure S1 lists all the possible chirality-mixed CC3 cages. The observation that 10 distinct cages are possible is one of the roots of the additional complexity in the crystal structure of CC3-racemic compared to the homochiral materials (CC3-R and CC3-S). We used an implicit solvent approach, specifically the solvent model based on density (SMD) method,[48] to estimate the impact of solvent on cage formation energies. Single point calculations with the SMD model were performed on structures optimized in the gas phase.

5.2.2 Cage Pair Packing Energies

Cage pair packing energies were calculated using DFT with a plane wave basis set and projector-augmented-wave pseudopotentials in the Vienna Ab initio Simulation Package (VASP). Cage pair packing energies were defined as the energy difference between a dimer of cages and the sum of two isolated cages:

$$E_{packing} = E_{cage\ dimer} - E_{cage\ I} - E_{cage\ II} \quad (1)$$

Initial structures for energy minimization of dimers of cages were constructed manually based on cage pair packing motifs in the bulk CC3-R crystal. Multiple starting configurations were tested to find the lowest energy dimer cage cluster. In these periodic

DFT calculations in VASP, the vdW-DF2 functional was used for capturing the long-range dispersion interactions because the APFD functional is not available in VASP.

5.2.3 Lattice-based Metropolis Monte Carlo (MC) Simulations

Once the overall composition of CC3-based cages was established, lattice-based MC simulations were performed to explore the distribution and orientation of cages within extended crystals. Simulations were performed on diamond-type coordinates with each lattice point representing a position for CC3-based cage corresponding to the faced centered packing, consistent with experimentally observed PXRD data.[37] Our MC simulations did not use periodic boundary conditions, so they represent crystals of finite size. In our Metropolis MC simulations we used an NVT ensemble where the number of each type of CC3-based cages and crystal's volume are fixed at room temperature.[49] Since the number of cages was fixed, the Hamiltonian describing the system's energy was defined as

$$\mathcal{H} = \sum_{\substack{ij \\ i \neq j}} E_{cage\ i,j\ packing} \tag{2}$$

Here, cage i and cage j are two adjacent cages, $E_{cage\ i,j\ packing}$ is the packing energy of these two cages. Longer range interactions between cages and multi-body terms were neglected. 10,000 initial cycles were applied for the system to reach equilibrium, and another 10,000 cycles were performed to provide data for averaging. Initial tests indicated these parameters gave well converged results. Two types of moves were included during each cycle: orientation moves for each heterochiral cage and swap moves exchanging the position of a pair of cages for each cage.

The local ordering of crystals obtained from these MC simulations was characterized by two-site correlation functions. $N_{nn}(X,Y)$ represents the average number of nearest-neighbor lattice pairs that are formed by CC3-X and CC3-Y cages (X, Y can be either R, S, RS, or SR). Similarly, $N_{nnn}(X,Y)$ represents the average number of next nearest neighbor sites that are formed by CC3-X and CC3-Y cages. The probability of finding a CC3-X cage sitting in a nearest-neighbor or next-nearest-neighbor sites of a CC3-Y cage is therefore

$$P_{nn}(X,Y) = \frac{N_{nn}(X,Y)}{N_{nn}(X,R) + N_{nn}(X,S) + N_{nn}(X,RS) + N_{nn}(X,SR)} \quad (3)$$

$$P_{nnn}(X,Y) = \frac{N_{nnn}(X,Y)}{N_{nnn}(X,R) + N_{nnn}(X,S) + N_{nnn}(X,RS) + N_{nnn}(X,SR)} \quad (4)$$

5.2.4 Crystal Energy Minimization through Molecular Dynamics (MD)

Atomically-detailed models of the CC3-R/CC3-S co-crystal and CC3-racemic crystal were initially developed by placing appropriately oriented CC3-based cages into each lattice site in a structure from the lattice model described above. The lattice parameters for both the CC3-R/CC3-S co-crystal model and CC3-racemic crystal model containing 54 CC3 cages was set to 53.24 Å based on a previously simulated CC3-R/CC3-S co-crystal structure.[41] To further refine the structures, energy minimization was performed for each model via molecular mechanics calculations using the LAMMPS package.[50] These calculations used the fully flexible force field Cage-Specific Force Field (CSFF) developed previously for CC3.[51] All CSFF intermolecular Lennard-Jones interactions were truncated at 10 Å. Coulombic interactions were computed pairwise to 10 Å, with long range contributions computed using Ewald summation with a relative

accuracy of 10^{-6}. During energy minimization, lattice constants and atom positions were relaxed using a series of algorithms, including the Polak-Ribiere version of the conjugate gradient algorithm, a Hessian-free truncated Newton algorithm, and a steepest descent algorithm.

5.2.5 X-ray Diffraction Simulations

Powder X-ray diffraction patterns for crystal models were simulated in Mercury.[52] In these simulations, the X-ray source was chosen as $CuK_{\alpha 1}$ radiation (wavelength 1.54056 Å). Non-hydrogen atoms were assumed to have isotropic atom displacement of 0.05 Å and H atoms were assigned with the isotropic atom displacement of 0.06 Å. All refection peaks were assumed to have a symmetric pseudo-Voight peak shape with a full width half maximum of 0.1 degree.

5.3 Composition of CC3-based Cages in CC3-racemic Solid Crystals

CC3 cages are synthesized from TFB ($C_9H_6O_3$) and DACH ($C_6H_{14}N_2$) by an imination condensation reaction.[1] In each CC3 cage, four planar $C_6(CN)_3H_6$ units are linked by six cyclohexane vertices, resulting in four triangular-shaped windows in a tetrahedral arrangement around the cage center. DACH has two stereocenters and thus has two trans enantiomers (R,R- and S,S- DACH) as shown in Figure 5.1(a). CC3-racemic crystals are synthesized using a racemic mixture of these enantiomers.[37] Since TFB is achiral, the two DACH enantiomers have the same probability of reacting with TFB. This implies that a range of products with the same stoichiometry as CC3-R or CC3-S can potentially be formed. We considered the complete set of molecules of this type in our calculations, as shown in Figure 5.2. Among those, CC3-R, CC3-1S5R, CC3-

5S1R and CC3-S only have one unique configuration. CC3-2S4R and CC3-4S2R, however, have *cis* or *trans* isomers, and CC3-3S3R has meridional (*mer*) or facial (*fac*) isomers as a result of positional isomerism.[53]

To investigate the population of each cage type, the formation energies for each species were calculated. We assume that the distribution of reaction products is controlled by thermodynamics, not kinetics. Our previous comparison between calculated formation energies and CC3 reaction products supports this assumption.[27] This implies that the fraction of cages of a specific type after reaction between TFB and DACH is

$$C_n = \frac{g_n \exp(\frac{-\Delta G_n}{k_B T})}{\sum_n g_n \exp(\frac{-\Delta G_n}{k_B T})} \quad (5)$$

where ΔG_n is the formation energy of cage type *n*, and g_n is the degeneracy of cage type *n*.

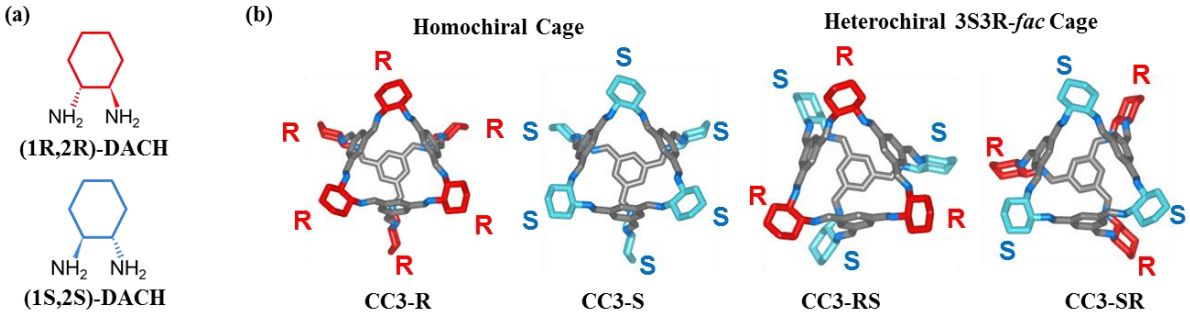

Figure 5.1(a) The two trans enantiomers (1R,2R)-, and (1S,2S)- of DACH. (b) Two types of homochiral cages, CC3-R and CC3-S, and two types of heterochiral 3S3R-*fac* cages, CC3-RS and CC3-SR in which the red vertices are formed from (1R,2R)-DACH and the blue vertices are formed from (1S,2S)-DACH. For clarity, hydrogen atoms are not shown.

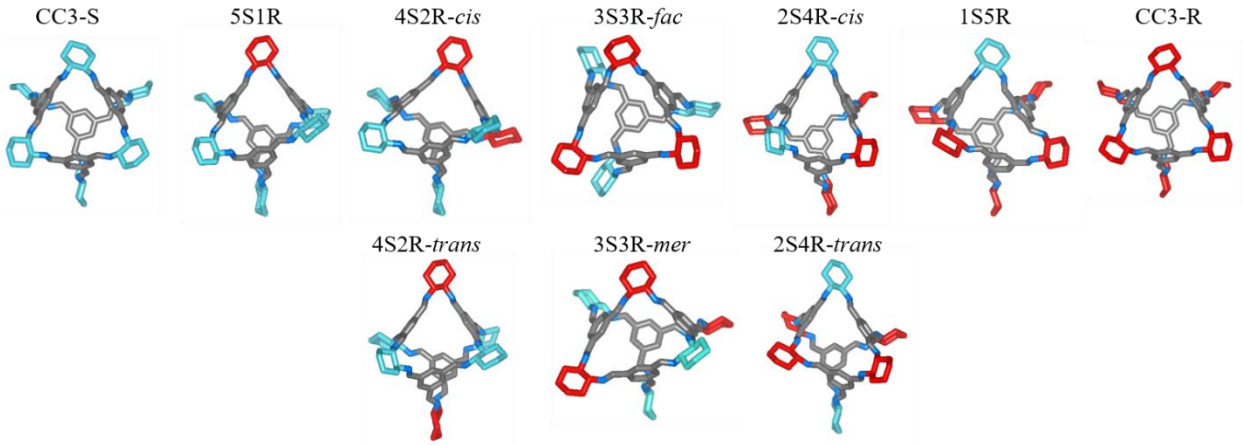

Figure 5.2 All the possible mixed-chirality CC3 cages, starting from CC3-R (all six vertices are R enantiomers), CC3-5S1R (one of six vertices is R enantiomer), CC3-4S2R (two of six vertices are R enantiomers), CC3-3S3R (three of six vertices are R enantiomers), CC3-2S4R (four of six vertices are R enantiomers), CC3-1S5R (five of six vertices are R enantiomers), to CC3-S (all six vertices are S enantiomers). (For clarity, hydrogen atoms are not shown.)

Table 5.1 Mixed-chirality CC3 cage formation energy, degeneracy, and resulting room temperature fractional concentration from gas phase DFT calculations (DFT calculations with implicit solvent corrections).

Cage Type	Formation energy[eV]	Degeneracy	Concentration (%)
CC3-R or CC3-S	-2.58 (-3.23)	1	45.8 (34.3)
1S5R or 5S1R	-2.35 (-3.06)	6	0.03 (0.28)
2S4R or 4S2R-*cis*	-2.36 (-3.09)	12	0.10 (1.61)
2S4R or 4S2R-*trans*	-1.91 (-2.76)	3	0.00 (0.00)
3S3R-*fac*	-2.48 (-3.18)	8	8.05 (27.55)
3S3R-*mer*	-1.96 (-2.67)	12	0.00 (0.00)

CC3 syntheses are carried out in solution, where the presence of solvent may influence the cage formation. As might be expected, solvents are known to have a considerable effect on cage formation.[36, 54] Because performing calculations with explicit solvent molecules is extremely demanding, we estimated the effects of solvent molecules

using the implicit solvent model based on density (SMD) method as described above.[48] The results of these calculations are listed in Table 5.1.

Table 5.1 predicts that the majority species formed among the possible CC3 cages are the homochiral cages, CC3-R and CC3-S. As dictated by symmetry, the population of each of these types of cages is equal. These cages are predicted to form 91.6% of all cages with energies from gas phase calculations, a number that is reduced to 68.6% when using solvent corrections. The remainder of the cage population is dominated by the 3S3R cages shown in Figure 5.1; gas phase (solvent corrected) calculations predict that 8.1 % (27.6%) of cages are of this kind. Since the cage structure involves both three R,R-DACH vertices and three S,S-DACH vertices, 3S3R-*fac* cages have two conformers denoted CC3-RS and CC3-SR.[38] These two kinds of conformers have the same energy (by symmetry). All of the other possible cages are predicted to have far smaller concentrations. The only other species predicted to make up more than 1% of the overall population are 2S4R-*cis* and 4S2R-*cis* cages.

5.4 Cage-Pair Interactions

After isolated cages are formed from the reaction of TFB and DACH, porous crystals made from many cages can nucleate and grow. Experimentally observed PXRD patterns of CC3-R and CC3-racemic crystals share very similar peak positions and intensities, strongly suggesting that the CC3-racemic crystal involves the same window-to-window cage packing motif as homochiral CC3-R crystals.[37] We therefore hypothesize that CC3-racemic crystals are made up of mixed chirality cages packed in a window-to-window configuration with four adjacent cages in an interconnected diamondoid pore

network as shown in Figure 5.3(a). The results above indicate that several distinct cage types are available for incorporation into these crystals. To predict what kinds of cage orderings might be favored in CC3-racemic crystals, we therefore must establish the energies associated with packing various kinds of cages next to each other. Because a detailed study of all possible packings in fully periodic materials is impractical, we assumed that the overall packing energy of a crystal can be approximated by pairwise contributions associated with neighboring cages and used DFT calculations to compute the cage's pairwise interaction energies.

We used the results in Table 5.1 to simplify the composition of CC3-racemic to only four types of cages: two homochiral CC3 cages (CC3-R and CC3-S), and two heterochiral cages (CC3-RS and CC3-SR). Each homochiral cage has four identical windows, which can be denoted (RRR) or (SSS), depending on the overall chirality of the cage. Here, R and S represents the chirality of the cyclohexane groups' vertices around the cage's triangular window. For the CC3-RS cage, three of the four windows are (SSR) and the remaining one is (RRR). Similarly, for the CC3-SR cage, three of the four windows are (RRS) and the remaining one is (SSS). In total, there are 10 potential window-to-window interactions: (RRR) to (RRR), (RRR) to (RRS), (RRR) to (RSS), (RRR) to (SSS), (RRS) to (RRS), (RRS) to (RSS), (RRS) to (SSS), (RSS) to (RSS), (RSS) to (SSS), and (SSS) to (SSS). Some of these interactions must be identical by symmetry. Taking advantage of this observation, there are six distinct window-to-window interactions that need to be considered. These pairs are shown in Figure 2(b). In addition, for (RRS) to (RSS) and (RSS) to (RSS) cage pairs, two unequal packing energies exist corresponding to two rotational conformations of the window packing, as

shown in Figure 5.3(b). The cage pair packing energies for all of these cases were calculated using DFT calculations with the vdW-DF2 functional as described above. The resulting pairwise interaction energies are shown in Table 5.2.

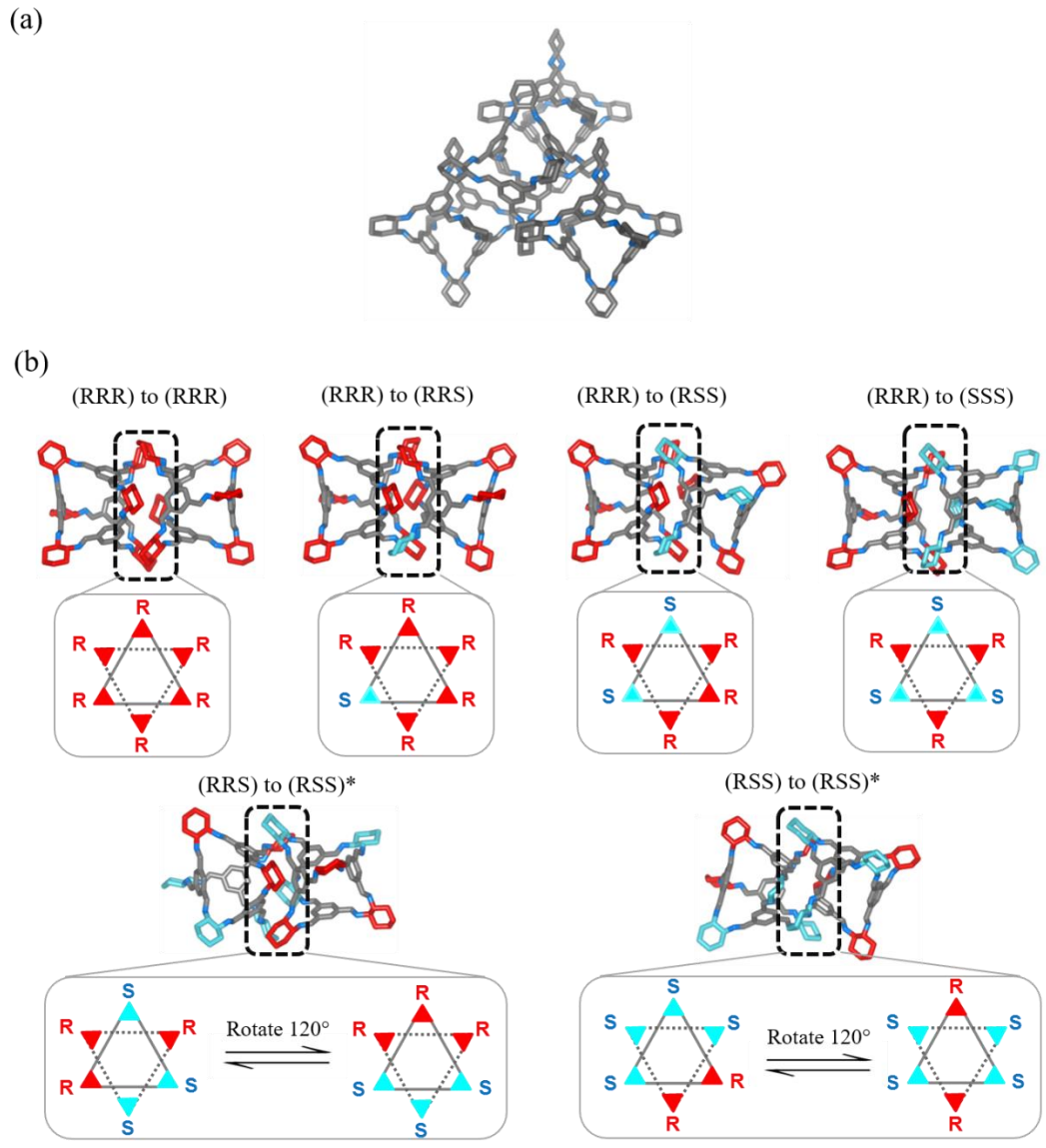

Figure 5.3 (a) CC3 cages packed in a window-to-window configuration with four adjacent cages in an interconnected diamondoid pore network. (b) Six distinct window-to-window cage pair interactions present in a CC3-racemic crystal. Solid and dashed triangles represent windows in two adjacent cages. Cage pairs with an asterisk (*) denote systems ((RRS) to (RSS) and (RSS) to (RSS)) that have two rotational conformations.

It is useful to consider the implications of the results in Table 5.2 for an idealized mixture that contains only homochiral cages, that is, a racemic mixture of CC3-R and CC3-S cages. Because <RRR,SSS> interactions are considerably more energetically favorable than <RRR,RRR> or <SSS,SSS> interactions, our calculations strongly suggest that a racemic mixture of this kind will crystallize in an ordered structure with alternating CC3-R and CC3-S cages. This is entirely consistent with the suggestion from Cooper and co-workers that CC3-R and CC3-S cages are packed in an alternating window-to-window packing motif in the CC3-R/CC3-S co-crystal.[25] This outcome is also consistent with the broader context of chiral crystallization, where is it known that the formation of racemic conglomerates is far more common than enantioselective formation of homochiral crystals.[39, 55-56]

Table 5.2 DFT calculated different window-to-window cage pair packing energies from vdW-DF2 DFT calculations with cage dimers. The two letter lists inside the angle brackets define the window types that form each window-to-window packing interaction.

Packing Interaction	<RRR,RRR>	<RRR,RRS>	<RRR,RSS>	<RRR,SSS>	<RRS,RSS>*		<SSR,SSR>*	
$E_{packing}$ *(eV)*	-2.11	-2.13	-2.15	-2.28	-2.19	-2.08	-2.15	-1.97

5.5 Predicting and Analyzing Lattice Model-based CC3-racemic Crystal Structural Properties

After identifying the type of CC3-based cages that can form, their concentration and the packing energies for these cages, lattice model-based Metropolis Monte Carlo (MC) simulations were performed to predict the spatial arrangement of CC3-based cages

in the CC3-racemic crystal. Each lattice point in the simulation model represents either a homochiral or a heterochiral CC3 cage.

Before modeling the CC3-racemic crystal, a simple co-crystal model containing only CC3-R and CC3-S was constructed and compared to experimental results. Previous work from Cooper and co-workers group suggested CC3-R and CC3-S cages are packed in an alternating window-to-window packing motif in the CC3-R/CC3-S co-crystal produced from co-precipitation.[34] In our simulation, temperatures spanning a broad range were tested, as shown in Figure 5.4. At room temperature, an alternating cage packing between CC3-R cages (red octahedra) and CC3-S cages (blue octahedra) was observed, in agreement with experimental observations. This alternating arrangement is driven by the strong cage pair packing energy between CC3-R and CC3-S. In contrast, at extremely high temperatures entropy plays a more important role than cage pair packing energy, resulting in a random arrangement of CC3-R and CC3-S cages. This latter situation is not intended to mimic any realistic experiment, but rather to verify that our calculations can probe a range of cage orderings.

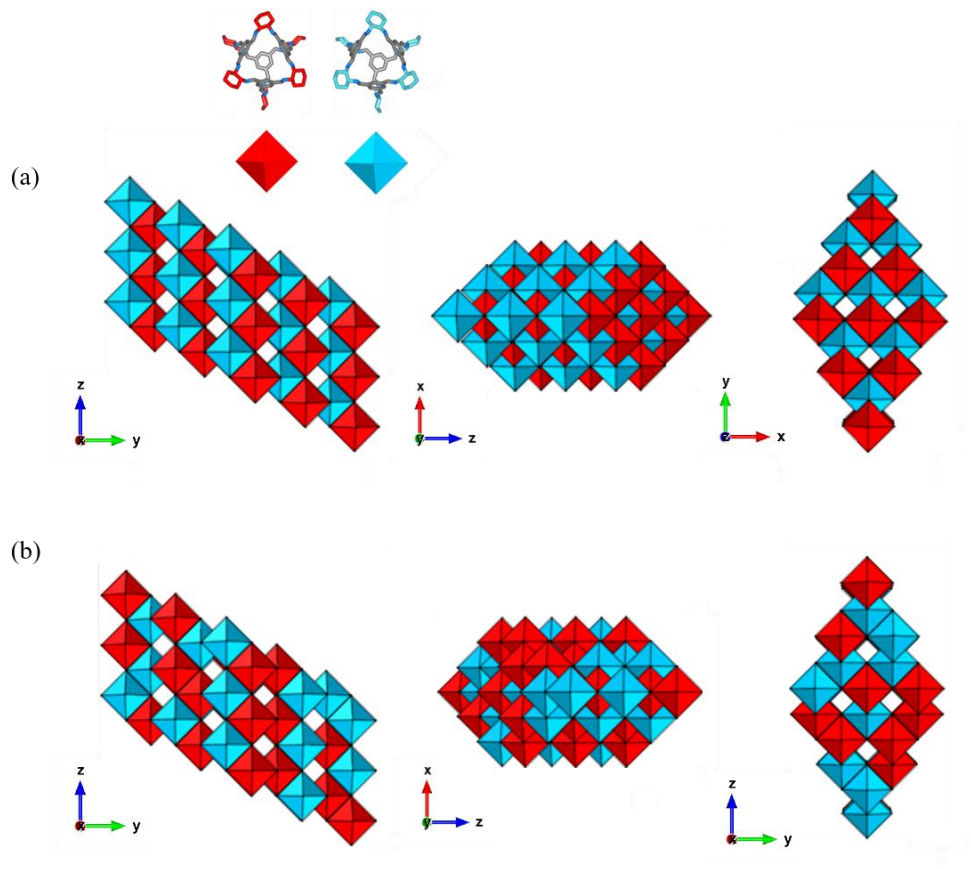

Figure 5.4 Three different viewpoints of the simulated CC3-R/CC3-S co-crystal lattice model (54 cages) at (a) room temperature; (b) artificially high temperature (10000K). (Red blocks are CC3-R cages and blue blocks are CC3-S cages.)

For modeling CC3-racemic crystals that include both homochiral (CC3-R and CC3-S) cages and heterochiral (CC3-RS and CC3-SR) cages, there is additional complexity must be considered in the simulation due to the orientation of heterochiral cages. Because heterochiral cages have two different types of window, the orientation of the cages influences the cage pair packing energies with their adjacent windows. In MC simulation, heterochiral cage orientation was updated in every simulation step with random sampling of all heterochiral cages' orientations. Figure 5.5(b) and (c) show three different MC simulation results for CC3-racemic crystal models with cage concentrations

obtained with and without implicit solvent corrections. Each simulation contained 250 distinct cages without periodic boundary conditions. Compared to the alternate packing of CC3-R and CC3-S cages in the CC3-R/CC3-S co-crystal, CC3-RS and CC3-SR show both clustering and mixing with alternating CC3-R and CC3-S cages in CC3-racemic crystals.

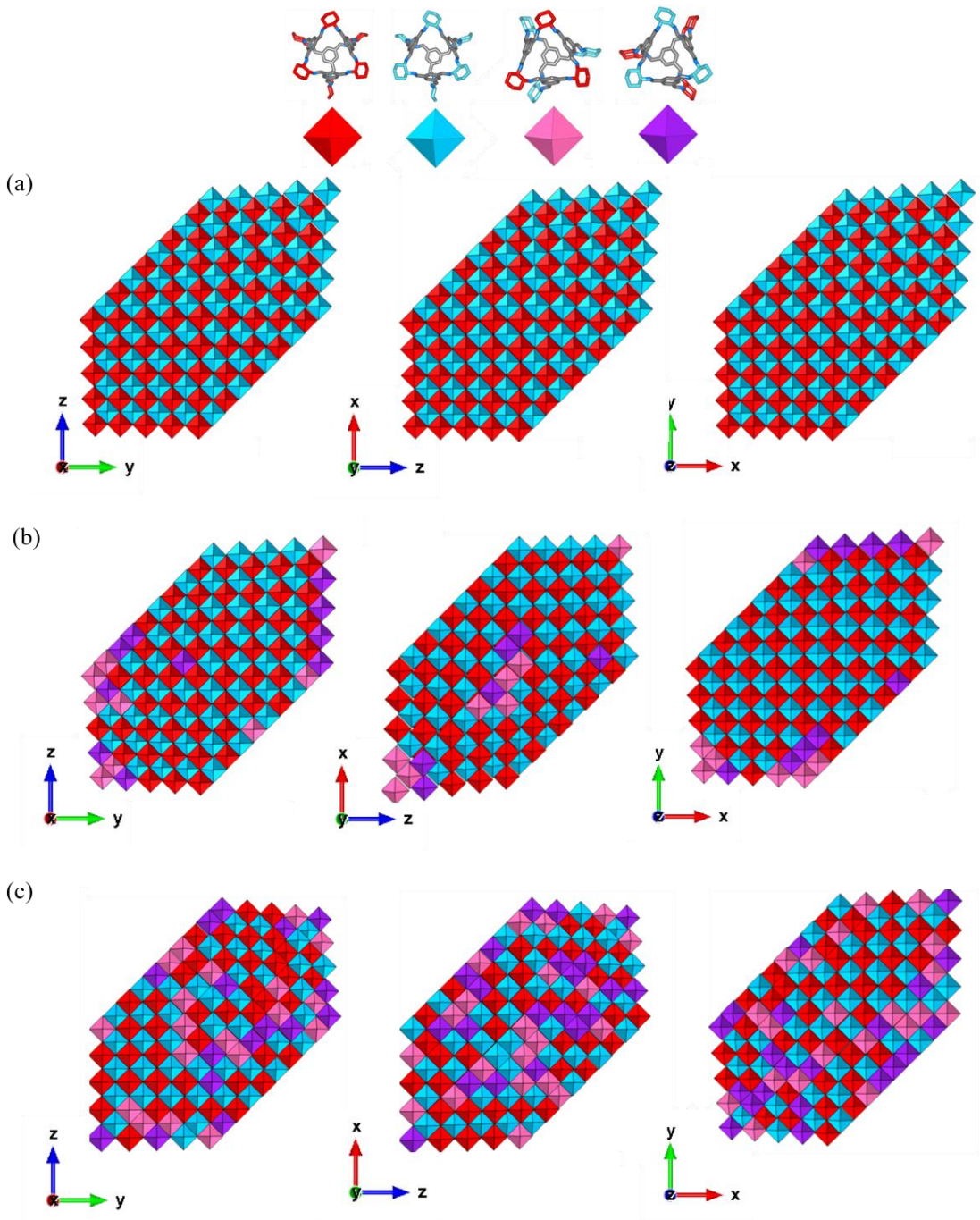

Figure 5.5 Snapshots from MC simulations viewed from three orientations of (a) a CC3-R/CC3-S co-crystal lattice model; (b) a CC3-racemic lattice model with cage concentrations from gas phase formation energies, and (c) a CC3-racemic lattice model, with cage concentrations from formation energies with implicit solvent corrections. (Red blocks are CC3-R cages, blue blocks are CC3-S cages, pink blocks are CC3-RS cages, and purple blocks are CC3-SR cages.)

We further characterized the short-range order of the homochiral and heterochiral cage distributions in the CC3-R/CC3-S co-crystal and CC3-racemic crystals using the correlation functions defined above. Simulation volumes comprised of 2000 cages without periodic boundary conditions were used for averaging. All of the analysis below comes from MC simulations performed at room temperature. Table 5.3 shows the detailed cage distribution probability of nearest neighbors and next-nearest neighbors centered on CC3-S cages, CC3-R cages, CC3-SR cages, and CC3-RS cages in two CC3-racemic crystal models. Taking the cage symmetry into consideration, the probability of finding a CC3-R cage sitting in a nearest-neighbor or next-nearest-neighbor sites of CC3-R (CC3-S) is the statistically equal to the probability of finding a CC3-S cage sitting in a nearest-neighbor or next-nearest-neighbor sites of CC3-S (CC3-R). CC3-RS and CC3-SR have the same symmetric. Therefore, in addition to demonstrating the cage distribution probabilities centered on CC3-S cages, CC3-R cages, CC3-SR cages, and CC3-RS cages individually, the averaged cage distribution probabilities centered on either CC3-S or CC3-R, and CC3-SR or CC3-RS, with symmetry consideration is calculated and shown in Figure 5.6 (a) (iii) and (vi), (b) (iii) and (vi). Figure 5.7 shows the cage distribution probability centered on a CC3-S cage (blue octahedron) in a CC3-R/CC3-S co-crystal, and the cage distribution probability centered on a CC3-S cage (blue octahedron) and a CC3-SR cage (purple octahedron) in CC3-racemics. Because the cage formation energies from gas phase calculations and using implicit solvent corrections predict different concentrations of cages in CC3-racemic crystals, results for each situation are shown. In each probability distribution illustrated in the figure, the inner ring represents the cage distribution probability of the center cage's nearest neighbor and the outer ring represents

the cage distribution probability of the center cage's next-nearest neighbor. The results in Figure 5.7(a) indicate a perfect alternating packing between CC3-R and CC3-S cages in the CC3-R/CC3-S co-crystal. This alternating packing is also the dominant motif in the CC3-racemic crystals shown in Figure 5.7(b) and (c), although not with the same degree of perfection. In these models, ~40-50% of the nearest neighbors of CC3-S were CC3-R, and ~30-40% of the next-nearest neighbors of CC3-S were CC3-S.

Table 5.3 Cage distribution probability of nearest neighbors and next-nearest neighbors centered on CC3-S cages, CC3-R cages, CC3-SR cages, and CC3-RS cages in two CC3-racemic.

Center Cage	CC3-racemic crystal (gas phase)				CC3-racemic crystal (implicit solvent model)			
CC3S	CC3S	CC3R	CC3SR	CC3RS	CC3S	CC3R	CC3SR	CC3RS
nn	6.71%	46.62%	21.47%	25.19%	15.33%	36.68%	21.63%	26.36%
nnn	38.09%	13.59%	23.55%	24.77%	27.08%	23.05%	25.88%	23.99%
CC3R	CC3S	CC3R	CC3SR	CC3RS	CC3S	CC3R	CC3SR	CC3RS
nn	45.33%	6.84%	23.97%	23.86%	35.56%	14.86%	26.71%	22.87%
nnn	14.03%	39.61%	21.57%	24.79%	22.84%	27.35%	25.08%	24.74%
CC3-SR	CC3S	CC3R	CC3SR	CC3RS	CC3S	CC3R	CC3SR	CC3RS
nn	17.64%	20.26%	22.90%	39.20%	20.00%	25.47%	25.19%	29.34%
nnn	20.19%	17.92%	34.79%	27.09%	25.56%	25.00%	25.79%	23.65%
CC3-RS	CC3S	CC3R	CC3SR	CC3RS	CC3S	CC3R	CC3SR	CC3RS
nn	21.72%	21.17%	41.06%	16.05%	25.59%	22.89%	30.80%	20.72%
nnn	23.38%	22.68%	29.84%	24.09%	24.16%	25.15%	24.12%	26.57%

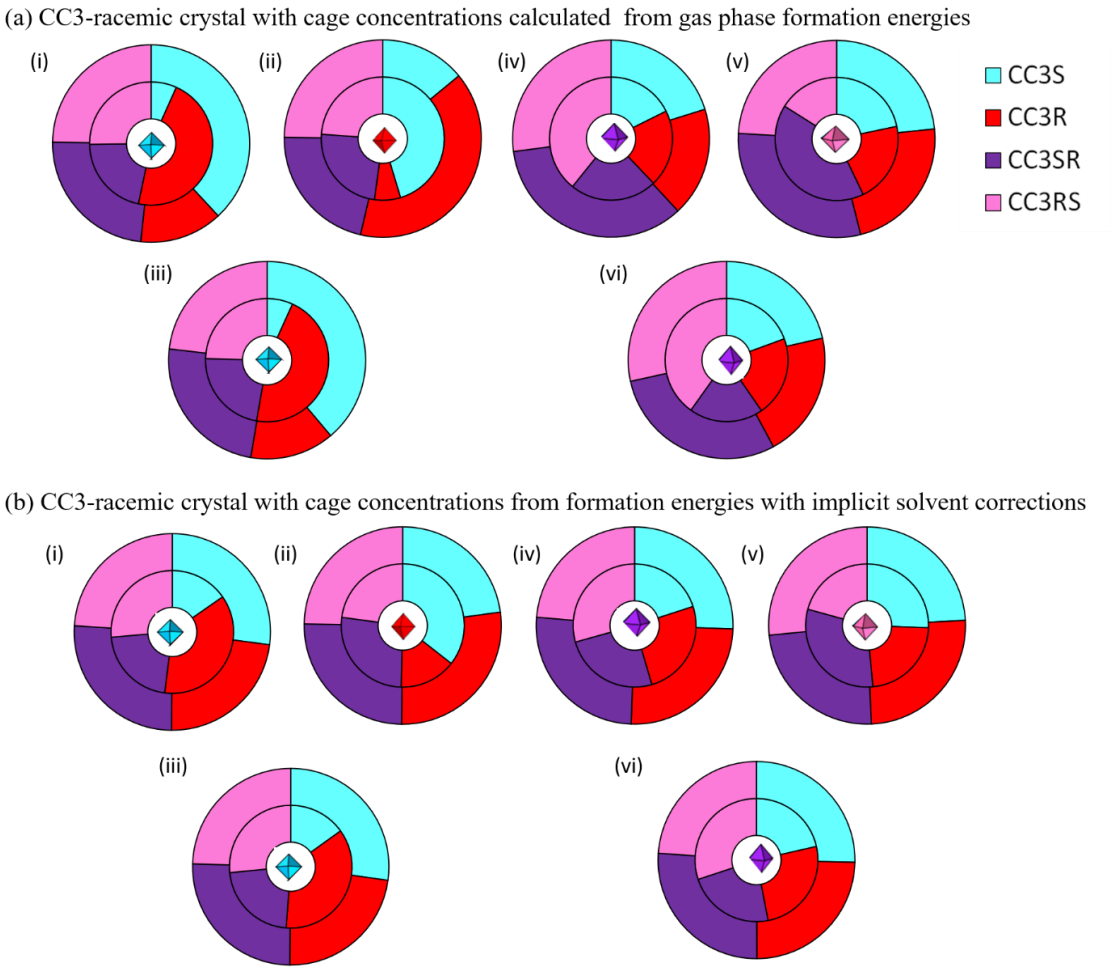

Figure 5.6 Pair correlation results from MC simulations. In each diagram, the reference cage is shown in the center and the nearest neighbor (next-nearest neighbor) probabilities are represented by the first and second concentric circle, respectively. (a) (i), (ii), (iv), and (v), and (b) (i), (ii), (iv), and (v) The cage distribution probabilities centered on CC3-S cages, CC3-R cages, CC3-SR cages, and CC3-RS cages in two CC3-racemic crystal models. (a) (iii) and (vi), (b) (iii) and (vi) averaged cage distribution probabilities centered on CC3-S cages and CC3-SR cages in two CC3-racemic crystal models.

It is useful to compare the results of our MC simulations with the cage distribution probabilities that would arise if the CC3-RS and CC3-SR molecules were randomly distributed through the CC3-racemic crystal. To this end, Figure 5.7(d) and (e) shows the outcome from a "mean field" model in which ordering of CC3-R and CC3-S

was assumed to be perfectly alternating but the remaining cages were distributed randomly. Comparing the maps centered at CC3-SR cage obtained from MC simulations to the mean-field theory results shows that the heterochiral cages tend to aggregate into small clusters within the CC3-racemic crystals. In our MC simulations, the majority (50-60%) of both nearest and second-nearest neighbor cages of heterochiral cages are also heterochiral cages. It is notable that this clustering is incomplete in the sense that our MC simulations do not predict phase separation between the heterochiral and homochiral cages.

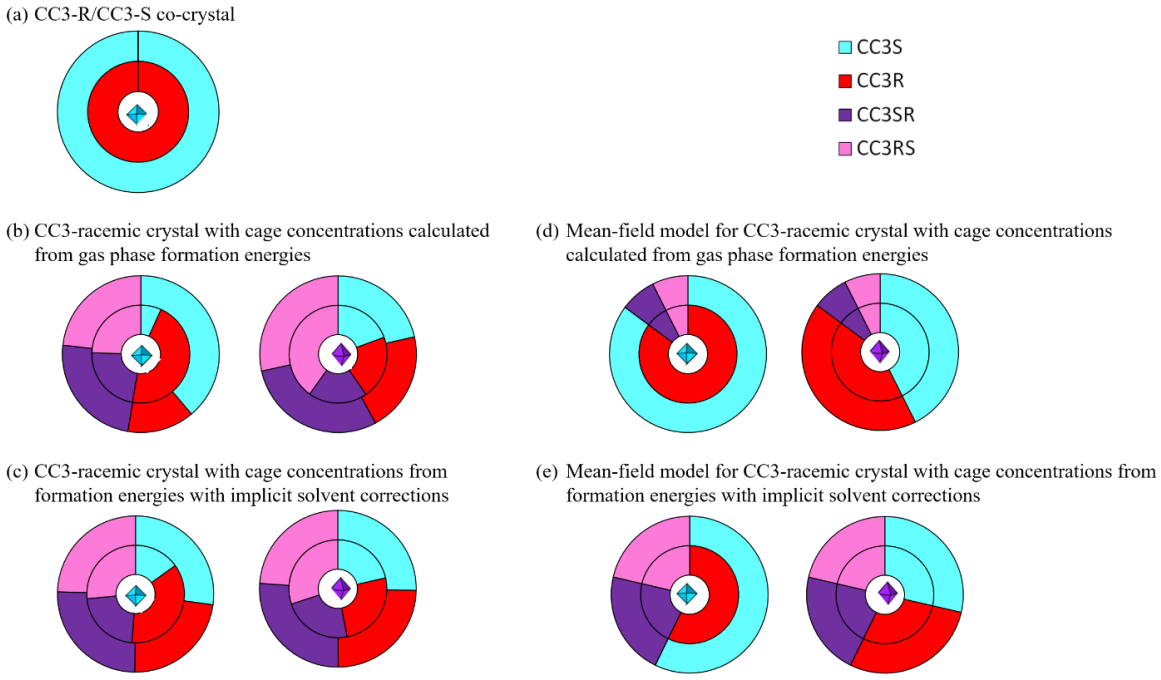

Figure 5.7 Pair correlation results from MC simulations. In each diagram, the reference cage is shown in the center and the nearest neighbor (next-nearest neighbor) probabilities are represented by the first and second concentric circle, respectively. (a) The cage distribution probabilities centered on CC3-S cage in the CC3-R/CC3-S co-crystal, (b) and (c) cage distribution probabilities centered on a CC3-S cage and CC3-SR cage in two CC3-racemic crystal models, (d) and (e) cage distribution probabilities based on mean-field theory centered on a CC3-S cage and CC3-SR cage in two CC3-racemic crystal models.

5.6 Atomically detailed CC3-racemic Crystal Structures

Although the lattice model described above gives insight into the ordering of molecular in CC3-racemic crystals, it is not possible to directly compare these properties to experiments. To allow us to predict the PXRD patterns of CC3-racemic crystals, equilibrated data from our MC simulations was used to generate atomically-detailed models. Each model of this type that we considered contained 54 cage molecules in a simulation volume with periodic boundary conditions. These structures were refined using the force field described in the Methods section.

PXRD patterns of three energy-minimized crystal models, including atomic models for a CC3-R/CC3-S co-crystal and two CC3-racemic crystals, and for experimentally synthesized CC3-racemic crystals are shown in Figure 5.8. A careful comparison between patterns for the co-crystal model and the CC3-racemic crystal model was performed to characterize possible experimental signatures that would arise when mixing heterochiral cages into homochiral cages. Figure 5.8(a) shows the patterns plotted on a linear intensity scale. In this representation, the patterns for the two CC3-racemic crystal models closely resemble that of the CC3-R/CC3-S co-crystal model. There is a very small systematic shift of peaks to lower angles with respect to CC3-R/CC3-S co-crystal because the unit cell parameters of the co-crystal model, 52.70 Å, are slightly smaller than for the CC3-racemic models, 52.98 Å and 52.93 Å. To further highlight possible differences between the patterns, we replotted the PXRD patterns using a log scale for intensity in Figure 5.8(b). Several minor peaks can be observed in the CC3-racemic crystal models at 10.8°, 11.2°, 12.9°, 13.5°, 14.7°, 16.6°, 19.1°, and 21.8° that are not observed in the CC3-R/CC3-S co-crystal. The intensities of those peaks, however,

are too small to be observable in the experimentally measured patterns seen in Figure 5.8(b)viii. This confirms the idea that PXRD is unable to distinguish between these materials, even though potentially important differences in the detailed structure of the materials exist. The modeling data we have presented regarding the composition and structure of CC3-racemic therefore provides the most thorough description available to date of this POC solid.

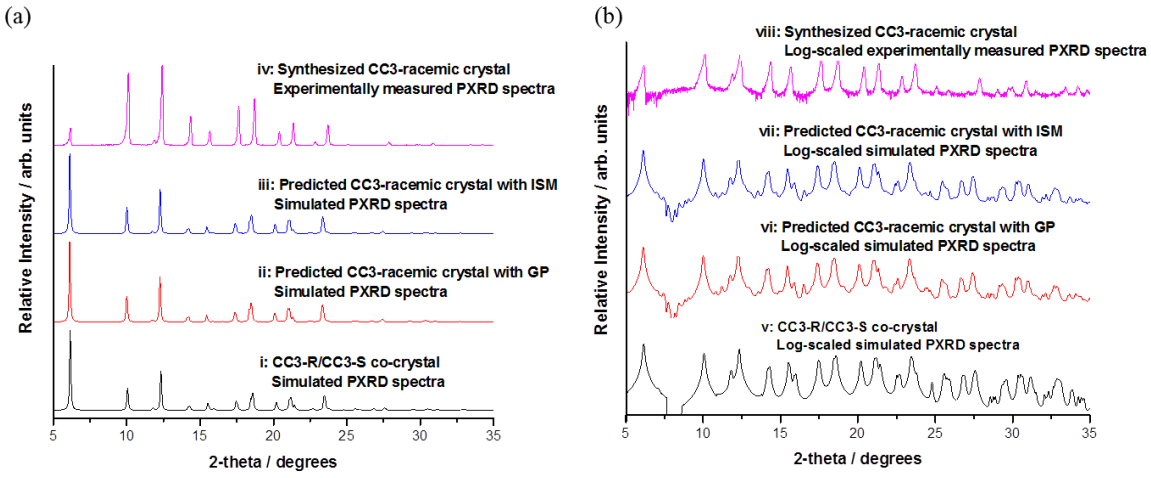

Figure 5.8 (a) PXRD patterns on a linear intensity scale of (i) an atomic model of a CC3-R/CC3-S co-crystal, (ii) an atomic model of a CC3-racemic crystal with composition from gas phase formation energies, (iii) an atomic model of a CC3-racemic crystal with composition generated using implicit solvent corrections, and (iv) experimental data for CC3-racemic crystals. (b) The same data as in (a) but using log scaling for the PXRD intensities.

5.7 Summary

This work has introduced an *in silico* prediction method that combines electronic structure calculations, atomistic calculations, and lattice based models to predict the atomic structure of racemic POC crystals. Our procedure began by enumerating the types of cage molecules that can be present and calculating the concentrations of these species.

The packing energies of pairs of POC molecules within the crystal structure of the racemic crystal were calculated. These packing energies were then used to define a lattice model representations of the racemic crystal that could be used to examine molecular ordering in extended crystals with MC simulations. Finally, by expanding configurations obtained from the lattice model into atomic-level detail, fully detailed CC3-racemic crystal models were obtained.

A key observation from our calculations is that CC3-racemic is made up of four distinct molecular species, two types of homochiral cages (CC3-R and CC3-S) and two types of heterochiral cages (CC3-RS and CC3-SR cages). In this sense, the racemic material is not a trivial extension of homochiral CC3 crystals, which contain only a single enantiomer of homochiral CC3 cages. Our calculations predict that the heterochiral cages are a minority species, with concentrations varying from 8 – 28% depending on whether implicit solvent corrections are used.

To characterize the cage distributions and structural properties within the racemic crystal, short-range order as well as long-range order were studied by cage pair correlation functions and PXRD patterns. In terms of short-range order, the inclusion of heterochiral cages has little influence on the strong preference for homochiral cages to form an alternative packing arrangement. Our calculations indicate that there is weak tendency for heterochiral cages to aggregate in CC3-racemic, but this tendency is not strong enough to suggest the possibility of phase separation from the homochiral cages. The PXRD patterns associated with our predicted structures are completely consistent with experimental observations, but this experimental technique is not able to readily detect the differences between the CC3-racemic structures that include heterochiral cages

and a simpler model of a CC3-R/CC3-S co-crystal. Our computational approach to describing the composition and structure of CC3-racemic is therefore a useful example of using methods of this kind to uncover structural information that is not accessible using routine experimental characterization.

5.8 References

1. Tozawa, T.; Jones, J. T. A.; Swamy, S. I.; Jiang, S.; Adams, D. J.; Shakespeare, S.; Clowes, R.; Bradshaw, D.; Hasell, T.; Chong, S. Y.; Tang, C.; Thompson, S.; Parker, J.; Trewin, A.; Bacsa, J.; Slawin, A. M. Z.; Steiner, A.; Cooper, A. I., Porous organic cages. *Nature materials* **2009,** *8* (12), 973-978.

2. Holst, J. R.; Trewin, A.; Cooper, A. I., Porous organic molecules. *Nature chemistry* **2010,** *2* (11), 915-920.

3. Briggs, M. E.; Cooper, A. I., A Perspective on the Synthesis, Purification, and Characterization of Porous Organic Cages. *Chemistry of Materials* **2017,** *29* (1), 149-157.

4. Hasell, T.; Cooper, A. I., Porous organic cages: soluble, modular and molecular pores. *Nature Reviews Materials* **2016,** *1* (9).

5. Jelfs, K. E.; Cooper, A. I., Molecular simulations to understand and to design porous organic molecules. *Current Opinion in Solid State and Materials Science* **2013,** *17* (1), 19-30.

6. Cooper, A. I., Nanoporous Organics Enter the Cage Age. *Angewandte Chemie-International Edition* **2011,** *50* (5), 996-998.

7. Evans, J. D.; Jelfs, K. E.; Day, G. M.; Doonan, C. J., Application of computational methods to the design and characterisation of porous molecular materials. *Chemical Society reviews* **2017**.

8. Jin, Y. H.; Zhu, Y. L.; Zhang, W., Development of organic porous materials through Schiff-base chemistry. *Crystengcomm* **2013,** *15* (8), 1484-1499.

9. Cooper, A. I., Porous Molecular Solids and Liquids. *ACS Central Science* **2017,** *3* (6), 544-553.

10. Pulido, A.; Chen, L. J.; Kaczorowski, T.; Holden, D.; Little, M. A.; Chong, S. Y.; Slater, B. J.; McMahon, D. P.; Bonillo, B.; Stackhouse, C. J.; Stephenson, A.; Kane, C. M.; Clowes, R.; Hasell, T.; Cooper, A. I.; Day, G. M., Functional materials discovery using energy-structure-function maps. *Nature* **2017,** *543* (7647), 657-+.

11. Kong, X.; Jiang, J. W., Porous organic cage membranes for water desalination: a simulation exploration. *Physical Chemistry Chemical Physics* **2017,** *19* (28), 18178-18185.

12. Song, Q.; Jiang, S.; Hasell, T.; Liu, M.; Sun, S.; Cheetham, A. K.; Sivaniah, E.; Cooper, A. I., Porous Organic Cage Thin Films and Molecular-Sieving Membranes. *Advanced materials* **2016**.

13. Hasell, T.; Miklitz, M.; Stephenson, A.; Little, M. A.; Chong, S. Y.; Clowes, R.; Chen, L.; Holden, D.; Tribello, G. A.; Jelfs, K. E.; Cooper, A. I., Porous Organic Cages for Sulfur Hexafluoride Separation. *J Am Chem Soc* **2016,** *138* (5), 1653-9.

14. Kewley, A.; Stephenson, A.; Chen, L.; Briggs, M. E.; Hasell, T.; Cooper, A. I., Porous Organic Cages for Gas Chromatography Separations. *Chemistry of Materials* **2015,** *27* (9), 3207-3210.

15. Chen, L.; Reiss, P. S.; Chong, S. Y.; Holden, D.; Jelfs, K. E.; Hasell, T.; Little, M. A.; Kewley, A.; Briggs, M. E.; Stephenson, A.; Thomas, K. M.; Armstrong, J. A.; Bell, J.; Busto, J.; Noel, R.; Liu, J.; Strachan, D. M.; Thallapally, P. K.; Cooper, A. I., Separation of rare gases and chiral molecules by selective binding in porous organic cages. *Nature materials* **2014,** *13* (10), 954-60.

16. Mitra, T.; Jelfs, K. E.; Schmidtmann, M.; Ahmed, A.; Chong, S. Y.; Adams, D. J.; Cooper, A. I., Molecular shape sorting using molecular organic cages. *Nature chemistry* **2013,** *5* (4), 276-81.

17. Camp, J. S.; Sholl, D. S., Transition State Theory Methods To Measure Diffusion in Flexible Nanoporous Materials: Application to a Porous Organic Cage Crystal. *The Journal of Physical Chemistry C* **2016,** *120* (2), 1110-1120.

18. Evans, J. D.; Sumby, C. J.; Doonan, C. J., Synthesis and Applications of Porous Organic Cages. *Chemistry Letters* **2015,** *44* (5), 582-588.

19. Slater, A. G.; Little, M. A.; Pulido, A.; Chong, S. Y.; Holden, D.; Chen, L.; Morgan, C.; Wu, X.; Cheng, G.; Clowes, R.; Briggs, M. E.; Hasell, T.; Jelfs, K. E.; Day, G. M.; Cooper, A. I., Reticular synthesis of porous molecular 1D nanotubes and 3D networks. *Nature chemistry* **2017,** *9* (1), 17-25.

20. Liu, M.; Chen, L. J.; Lewis, S.; Chong, S. Y.; Little, M. A.; Hasell, T.; Aldous, I. M.; Brown, C. M.; Smith, M. W.; Morrison, C. A.; Hardwick, L. J.; Cooper, A. I., Three-dimensional protonic conductivity in porous organic cage solids. *Nature communications* **2016,** *7*.

21. Hasell, T.; Culshaw, J. L.; Chong, S. Y.; Schmidtmann, M.; Little, M. A.; Jelfs, K. E.; Pyzer-Knapp, E. O.; Shepherd, H.; Adams, D. J.; Day, G. M.; Cooper, A. I., Controlling the Crystallization of Porous Organic Cages: Molecular Analogs of Isoreticular Frameworks Using Shape-Specific Directing Solvents. *Journal of the American Chemical Society* **2014,** *136* (4), 1438-1448.

22. Evans, J. D.; Huang, D. M.; Hill, M. R.; Sumby, C. J.; Thornton, A. W.; Doonan, C. J., Feasibility of Mixed Matrix Membrane Gas Separations Employing Porous Organic Cages. *The Journal of Physical Chemistry C* **2014,** *118* (3), 1523-1529.

23. Jiang, S.; Chen, L.; Briggs, M. E.; Hasell, T.; Cooper, A., Functional Porous Composites by Blending with Solution-Processable Molecular Pores. *Chem. Commun.* **2016**.

24. Jiang, S.; Jones, J. T.; Hasell, T.; Blythe, C. E.; Adams, D. J.; Trewin, A.; Cooper, A. I., Porous organic molecular solids by dynamic covalent scrambling. *Nature communications* **2011,** *2*, 207.

25. Jones, J. T.; Hasell, T.; Wu, X.; Bacsa, J.; Jelfs, K. E.; Schmidtmann, M.; Chong, S. Y.; Adams, D. J.; Trewin, A.; Schiffman, F.; Cora, F.; Slater, B.; Steiner, A.; Day, G. M.; Cooper, A. I., Modular and predictable assembly of porous organic molecular crystals. *Nature* **2011,** *474* (7351), 367-71.

26. Belowich, M. E.; Stoddart, J. F., Dynamic imine chemistry. *Chemical Society reviews* **2012,** *41* (6), 2003-2024.

27. Zhu, G.; Liu, Y.; Flores, L.; Lee, Z. R.; Jones, C. W.; Dixon, D. A.; Sholl, D. S.; Lively, R. P., Formation Mechanisms and Defect Engineering of Imine-Based Porous Organic Cages. *Chemistry of Materials* **2018,** *30* (1), 262-272.

28. Lucero, J.; Elsaidi, S. K.; Anderson, R.; Wu, T.; Gómez-Gualdrón, D. A.; Thallapally, P. K.; Carreon, M. A., Time Dependent Structural Evolution of Porous Organic Cage CC3. *Crystal Growth & Design* **2018,** *18* (2), 921-927.

29. Jelfs, K. E.; Schiffmann, F.; Jones, J. T. A.; Slater, B.; Cora, F.; Cooper, A. I., Conformer interconversion in a switchable porous organic cage. *Physical Chemistry Chemical Physics* **2011,** *13* (45), 20081-20085.

30. Jelfs, K. E.; Wu, X. F.; Schmidtmann, M.; Jones, J. T. A.; Warren, J. E.; Adams, D. J.; Cooper, A. I., Large Self-Assembled Chiral Organic Cages: Synthesis, Structure, and Shape Persistence. *Angewandte Chemie-International Edition* **2011,** *50* (45), 10653-10656.

31. Hasell, T.; Chong, S. Y.; Jelfs, K. E.; Adams, D. J.; Cooper, A. I., Porous Organic Cage Nanocrystals by Solution Mixing. *Journal of the American Chemical Society* **2012,** *134* (1), 588-598.

32. Hazen, R. M.; Sholl, D. S., Chiral selection on inorganic crystalline surfaces. *Nature materials* **2003,** *2* (6), 367-374.

33. Lee, H. E.; Ahn, H. Y.; Mun, J.; Lee, Y. Y.; Kim, M.; Cho, N. H.; Chang, K.; Kim, W. S.; Rho, J.; Nam, K. T., Amino-acid- and peptide-directed synthesis of chiral plasmonic gold nanoparticles. *Nature* **2018,** *556* (7701), 360-+.

34. Cooper, A. I.; Day, G. M.; Jones, J. T. A.; Wu, X. F.; Hasell, T.; Bacsa, J.; Jelfs, K. E.; Scmidtmann, M.; Chong, S. Y.; Trewin, A.; Schiffman, F.; Cora, F.; Slater, B.; Steiner, A., Modular and predictable assembly of porous organic molecular crystals. *Nature* **2011,** *474* (7351), 367-371.

35. Hasell, T.; Chong, S. Y.; Schmidtmann, M.; Adams, D. J.; Cooper, A. I., Porous Organic Alloys. *Angewandte Chemie-International Edition* **2012,** *51* (29), 7154-7157.

36. Hasell, T.; Little, M. A.; Chong, S. Y.; Schmidtmann, M.; Briggs, M. E.; Santolini, V.; Jelfs, K. E.; Cooper, A. I., Chirality as a tool for function in porous organic cages. *Nanoscale* **2017,** *9* (20), 6783-6790.

37. Zhu, G.; Hoffman, C. D.; Liu, Y.; Bhattacharyya, S.; Tumuluri, U.; Jue, M. L.; Wu, Z.; Sholl, D. S.; Nair, S.; Jones, C. W.; Lively, R. P., Engineering Porous Organic Cage Crystals with Increased Acid Gas Resistance. *Chemistry-a European Journal* **2016,** *22* (31), 10743-10747.

38. Slater, A. G.; Little, M. A.; Briggs, M. E.; Jelfs, K. E.; Cooper, A. I., A solution-processable dissymmetric porous organic cage. *Molecular Systems Design & Engineering* **2018,** *3* (1), 223-227.

39. Rankin, R. B.; Sholl, D. S., Structures of glycine, enantiopure alanine, and racemic alanine adlayers on Cu(110) and Cu(100) surfaces. *Journal of Physical Chemistry B* **2005,** *109* (35), 16764-16773.

40. Rankin, R. B.; Sholl, D. S., First-principles studies of chiral step reconstructions of Cu(100) by adsorbed glycine and alanine. *The Journal of chemical physics* **2006,** *124* (7), 74703.

41. Pyzer-Knapp, E. O.; Thompson, H. P. G.; Schiffmann, F.; Jelfs, K. E.; Chong, S. Y.; Little, M. A.; Cooper, A. I.; Day, G. M., Predicted crystal energy landscapes of porous organic cages. *Chemical Science* **2014,** *5* (6), 2235-2245.

42. Jones, J. T. A.; Hasell, T.; Wu, X. F.; Bacsa, J.; Jelfs, K. E.; Schmidtmann, M.; Chong, S. Y.; Adams, D. J.; Trewin, A.; Schiffman, F.; Cora, F.; Slater, B.; Steiner, A.; Day, G. M.; Cooper, A. I., Modular and predictable assembly of porous organic molecular crystals. *Nature* **2011,** *474* (7351), 367-371.

43. Santolini, V.; Miklitz, M.; Berardo, E.; Jelfs, K. E., Topological landscapes of porous organic cages. *Nanoscale* **2017,** *9* (16), 5280-5298.

44. Lee, S.; Yang, A.; Moneypenny, T. P.; Moore, J. S., Kinetically Trapped Tetrahedral Cages via Alkyne Metathesis. *Journal of the American Chemical Society* **2016,** *138* (7), 2182-2185.

45. Liu, X.; Warmuth, R., Solvent Effects in Thermodynamically Controlled Multicomponent Nanocage Syntheses. *Journal of the American Chemical Society* **2006,** *128* (43), 14120-14127.

46. Austin, A.; Petersson, G. A.; Frisch, M. J.; Dobek, F. J.; Scalmani, G.; Throssell, K., A Density Functional with Spherical Atom Dispersion Terms. *Journal of Chemical Theory and Computation* **2012,** *8* (12), 4989-5007.

47. Godbout, N.; Salahub, D. R.; Andzelm, J.; Wimmer, E., Optimization of Gaussian-type basis sets for local spin density functional calculations. Part I. Boron through neon, optimization technique and validation. *Canadian Journal of Chemistry* **1992,** *70* (2), 560-571.

48. Marenich, A. V.; Cramer, C. J.; Truhlar, D. G., Universal Solvation Model Based on Solute Electron Density and on a Continuum Model of the Solvent Defined by the Bulk Dielectric Constant and Atomic Surface Tensions. *Journal of Physical Chemistry B* **2009,** *113* (18), 6378-6396.

49. Metropolis, N.; Rosenbluth, A. W.; Rosenbluth, M. N.; Teller, A. H.; Teller, E., Equation of State Calculations by Fast Computing Machines. *Journal of Chemical Physics* **1953,** *21* (6), 1087-1092.

50. Plimpton, S., Fast Parallel Algorithms for Short-Range Molecular Dynamics. *J. Comput. Phys.* **1995,** *117* (1), 1-19.

51. Holden, D.; Jelfs, K. E.; Cooper, A. I.; Trewin, A.; Willock, D. J., Bespoke Force Field for Simulating the Molecular Dynamics of Porous Organic Cages. *The Journal of Physical Chemistry C* **2012,** *116* (31), 16639-16651.

52. Macrae, C. F.; Bruno, I. J.; Chisholm, J. A.; Edgington, P. R.; McCabe, P.; Pidcock, E.; Rodriguez-Monge, L.; Taylor, R.; van de Streek, J.; Wood, P. A., Mercury CSD 2.0 - new features for the visualization and investigation of crystal structures. *Journal of Applied Crystallography* **2008,** *41*, 466-470.

53. Jiang, S.; Jones, J. T. A.; Hasell, T.; Blythe, C. E.; Adams, D. J.; Trewin, A.; Cooper, A. I., Porous organic molecular solids by dynamic covalent scrambling. *Nature communications* **2011,** *2*.

54. Liu, X. J.; Warmuth, R., Solvent effects in thermodynamically controlled multicomponent nanocage syntheses. *Journal of the American Chemical Society* **2006,** *128* (43), 14120-14127.

55. Eliel, E. L.; Wilen, S. H.; Mander, L. N., *Stereochemistry of organic compounds*, John Wiley & Sons, New York, 1994.

56. Jacques, J.; Collet, A.; Wilen, S. H., *Enantiomers, Racemates, and Resolutions*, John Wiley & Sons, New York, 1981.

CHAPTER 6. SUMMARY AND SUGGESTIONS FOR FUTURE WORK

6.1 Summary

A significant challenge in the chemical industry is to remove environmentally harmful gases before their emission to the atmosphere. Adsorption-based separation technology using porous materials has been shown to be a promising method to solve this issue. A large variety of porous materials have been synthesized and evaluated for these applications, such as zeolites, MOFs, and recently newly synthesized materials, POCs. In current state of the art, zeolites are the only materials among above three that have been widely commercialized in industry, while MOFs and POCs are still mostly investigated on the lab-scale. One issue that we need to address before implementing new materials in industrial separation processes is the stability of these materials in the face of aggressive contaminants, such as the humid acid gas's present in flue gas. Therefore, the overall objective of this thesis has been to propose computational modeling for understanding the chemical stability and degradation mechanisms of porous materials under acidic environments.

Chapter 2 and Chapter 3 focused on the study of MOFs. In Chapter 2, we developed sheet models for all external surface MOFs, M-BDC nanosheets (M = Zn, Cu, and Co), and studied acid gas adsorption on surface-specific adsorption sites. In addition to considering pure component adsorption behavior, we explored how gas mixtures, taking flue gas mixture as an example, interact with Cu-BDC nanosheet. Among the

components in the flue gas mixture, sulfur hydrates (H_2SO_3, and H_2SO_4) were predicted to dominate the equilibrium adsorption and bind to a large number of surface sites. Finally, we explored the chemical stability and potential degradation pathway of Cu-BDC nanosheet under exposure to sulfur hydrates. The second type of MOFs we investigated was UiO-66, in Chapter 3. We developed a series of UiO-66 based crystal models with different concentrations of defects and different types of compensating groups, including parent UiO-66, TFA group capped missing-linker defective UiO-66 (TFA-UiO-66), TFA group capped missing-cluster defective UiO-66 (**reo**-defective UiO-66), and hydrolyzed missing-linker defective UiO-66 (ML-UiO-66). Using these models, we explored the influence of defects on the crystal porosity and the chemical stability of these materials. We found that the structural incorporation of TFA modulators in defective TFA-UiO-66 helps to increase crystal porosity without sacrificing its chemical stability in harsh conditions.

Chapter 4 and Chapter 5 focused on the understanding a type of imine-based porous materials, CC3-R, including formation mechanism, defect engineering, chemical stability, and mixed chirality. Since POCs are a class of relatively new porous materials, before studying their chemical stability, in Chapter 4 we explored the formation mechanism of CC3-R, finding that several other intermediate cages could co-exist with the complete CC3-R cage in the final product. Then, "missing-linker" type of defects were introduced in CC3-R materials, and these defective CC3-R materials exhibit enhanced CO_2 adsorption capacity and adsorption strength due to the additional functional groups that present within the crystal. Finally, we explored the chemical stability of CC3-R under exposure to the acidic environment and investigate the

degradation mechanism behind the instability. In Chapter 5, we developed and synthesized a type of chemical-stable POCs, CC3-racemic crystal. Since it is exceptionally challenging to fully solve the crystal structure experimentally, we developed a comprehensive theoretical prediction method with the combination of electronic structure calculations and molecule modeling calculations to predict the atomic structure of this chemical-stable CC3-racemic crystal.

Overall, this thesis explores a general computational methodology to understand the chemical stability of porous materials under attack from water or acidic molecules. This theoretical study will enable efforts to develop chemically stable porous materials that are suitable for use in the separation application even with the presence of aggressive contaminants such as H_2S, SO_X, and NO_X.

6.2 Suggestions for Future Work

Compared to water attack, degradation of MOFs under attack by acidic molecules involves more complicated reactions. Therefore, a thorough and clear understanding of the chemical stability of MOFs under moist conditions and the corresponding water-induced degradation mechanism is needed before expanding the chemical stability study to acidic environments. Potential future work is to develop an evaluation metric that consists of several valuables that can be calculated by electronic structure or other calculations and validate the feasibility of using the developed evaluation metric to predict the chemical stability of MOFs under water attack qualitatively.

To achieve this goal, we start by investigating the general degradation reactions MOFs may experience during water attack, which has been completed up to now.

Through extended literature review on the study of degradation mechanism of MOFs and our effort in exploring the degradation mechanism of M-BDC nanosheets (M = Zn, Cu, and Co) and a series of UiO-66 based materials using computational method in this thesis, we can propose a systematically degradation pathway of MOFs under exposure to water that are applicable more generally to MOFs. This generalized degradation pathway starts with the protonation of the water molecule, the cleavage of the metal-ligand bond, and the coordination of the hydroxyl group into OMS. This step involved in the degradation reactions is denoted as water insertion reaction, shown in Figure 6.1. Formation energy associated with such reaction can be used as an indicator to analyze the feasibility of reaction from a thermodynamic perspective.

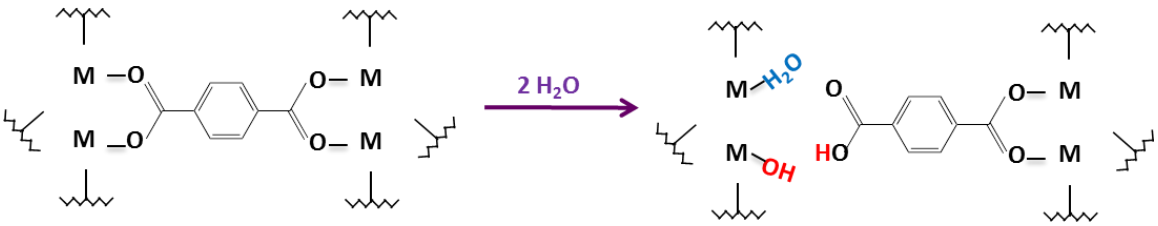

Figure 6.1 Illustration of water insertion reaction, including the protonation of the water molecule, the cleavage of the metal-ligand bond, and the coordination of the hydroxyl group into OMS. (M as metal center and BDC as linker)

In the existing studies, there have been some efforts to predict the relative chemical stability of MOFs.[1-2] In Low et al.'s work, they observed good agreement between theoretical calculations and experiments regarding relative hydrothermal stability of MOFs, which implied their calculated activation energies for ligand replacement by water in different MOFs can provide a useful estimate for MOFs' hydrothermal stability. However, some statements and methods used in their work made their conclusion not strongly persuasive. First, all the electronic structure calculations

were based upon MOFs' cluster models, obtained by truncating from periodic models, which lost the real periodicity of materials. Our previous study has highlighted the importance of periodicity in capturing the water interaction with MOFs.[3] Thus their cluster calculations potentially were not able to give accurate enough description of water attack results. Another issue is that the calculated predictor for hydrothermal stability was activation energy for ligand replacement by water reaction, where dangling ligand was kept charged without being protonated. As described in the previous paragraph, comparing to ligand replacement by water molecule, the cleavage of the metal-ligand bond by the protonation of the water molecule has been investigated and shown to be a dominant step for MOFs degradation pathway. Therefore, a more thorough and comprehensive calculated predictor for hydrothermal stability is activation energy for water insertion reaction. However, it is too much time-consuming to calculate activation energy relative to formation energy, thus using formation energy for water insertion reaction is more appealing for large-scale screening of MOFs' water stability. In addition to above two suspect statements regarding modeling method, too many important variables that could potentially influence chemical stability are different among the 10 MOFs being considered in their study. The chemical stability of MOFs depends on many various factors, ranging from structural properties to chemical properties. The most important structural properties are the coordination number of metal cluster, and chemical properties can be the identity of metal, the identity of the organic linker, the linker pKa, etc. With many variables being different, it is difficult to evaluate the validity of using calculated activation energy as a predictor to forecast the hydrothermal stability of MOFs.

To address these potential issues, our objective is to use water insertion reaction energy as a thermodynamic predictor to evaluate the relative chemical stability of MOFs under exposure to water. First, water insertion reaction energies are calculated with periodic models, representing the real periodicity of materials and imposing the natural constraints on the end of ligands during hydrolysis reactions. Furthermore, to shrink the combined influence of different variables in MOFs, we narrow the selection of MOF candidates down to a sub-class of MOFs, where the metal centers are connected by BDC-based linkers, such as MOF-2[4], IRMOF-1[1], IRMOF-3[5], UiO-66, MIF-47[6], etc. A database of water insertion reaction energy in such sub-class of MOFs could then be created. With the pre-knowledge of chemical stability of some MOFs inside this sub-class measured experimentally, performing further data analysis on water insertion reaction energy database is helpful to evaluate the validity of using water insertion reaction energy calculated by electronic structure calculations to predict MOF's chemical stability.

6.3 References

1. Low, J. J.; Benin, A. I.; Jakubczak, P.; Abrahamian, J. F.; Faheem, S. A.; Willis, R. R., Virtual High Throughput Screening Confirmed Experimentally: Porous Coordination Polymer Hydration. *Journal of the American Chemical Society* **2009,** *131* (43), 15834-15842.

2. Yuan, S.; Feng, L.; Wang, K. C.; Pang, J. D.; Bosch, M.; Lollar, C.; Sun, Y. J.; Qin, J. S.; Yang, X. Y.; Zhang, P.; Wang, Q.; Zou, L. F.; Zhang, Y. M.; Zhang, L. L.; Fang, Y.; Li, J. L.; Zhou, H. C., Stable Metal-Organic Frameworks: Design, Synthesis, and Applications. *Advanced materials* **2018,** *30* (37).

3. Howe, J. D.; Liu, Y.; Flores, L.; Dixon, D. A.; Sholl, D. S., Acid Gas Adsorption on Metal-Organic Framework Nanosheets as a Model of an "All-Surface" Material. *Journal of Chemical Theory and Computation* **2017,** *13* (3), 1341-1350.

4. Li, H.; Eddaoudi, M.; Groy, T. L.; Yaghi, O. M., Establishing microporosity in open metal-organic frameworks: Gas sorption isotherms for Zn(BDC) (BDC = 1,4-

benzenedicarboxylate). *Journal of the American Chemical Society* **1998,** *120* (33), 8571-8572.

5. Nguyen, J. G.; Cohen, S. M., Moisture-Resistant and Superhydrophobic Metal-Organic Frameworks Obtained via Postsynthetic Modification. *Journal of the American Chemical Society* **2010,** *132* (13), 4560-+.

6. Kang, I. J.; Khan, N. A.; Haque, E.; Jhung, S. H., Chemical and Thermal Stability of Isotypic Metal-Organic Frameworks: Effect of Metal Ions. *Chemistry-a European Journal* **2011,** *17* (23), 6437-6442.